Imperial College London

Mechanisms of High Temperature Degradation of Thermal Barrier Coatings

Rudder T.C. Wu
Department of Materials,
Imperial College, London

A thesis presented for the Degree of Doctor
of Philosophy of the Imperial College, London

January 2009

Abstract

Thermal barrier coatings (TBCs) are crucial for increasing the turbine inlet temperature (and hence efficiency) of gas turbine engines. The thesis describes PhD research aimed at improving understanding of the thermal cycling failure mechanisms of electron beam physical vapour deposited (EB-PVD) yttria stabilised zirconia (YSZ) TBCs on single crystal superalloys.

The research consisted of three different stages. The first stage involved designing a coupled one-dimensional thermodynamic-kinetic oxidation and diffusion model capable of predicting the concentration profiles of alloying elements in a single-phase γ nickel-rich Ni-Al-Cr ternary alloy by the finite difference method. The aim of this investigation was to improve the understanding of interactions between alloying species and developing oxide. The model demonstrated that in the early stages of oxidation, Al consumption by oxide scale growth is faster than Al replenishment by diffusion towards the scale, resulting in an initial Al depletion in the alloy near the scale.

The second stage involved a systematic study of the life-time of TBC systems on different single crystal superalloys. The study aimed at demonstrating that the compatibility of modern nickel-based single crystal superalloys with TBC systems is influenced strongly by the content of alloying element additions in the superalloy substrate. The results can be explained by postulating that the fracture toughness parameters controlling decohesion are influenced strongly by small changes in composition arising from interdiffusion with the bond coat, which itself inherits elemental changes from the substrate.

The final stage of study involved a detailed study of different bond coats (two β-structured Pt-Al types and a γ/γ' Pt-diffusion type) in TBC systems based on an EB-PVD YSZ top coat and a substrate material of CMSX-4 superalloy. Generation of stress in the thermally grown oxide (TGO) on thermal cycling, and its relief by plastic deformation and fracture, were investigated experimentally in detail.

Acknowledgements

I would like to gratefully acknowledge the enthusiasm, support and guidance of my supervisors, Professor Alan Atkinson, and Professor Roger Reed. I would like to thank Dr. Hiroshi Harada, Dr. Kyoko Kawagishi of National Institute for Materials Science Japan and Mr. Rodney Wing of Chromalloy - UK for the provision of research facilities and specimens and Dr. Xin Wang for his help on TGO stress measurement. Financial support for my PhD project has been provided for by the Engineering and Physical Sciences Research Council (EPSRC), the Overseas Research Studentship (ORS) and the Natural Sciences and Engineering Research Council of Canada (NSERC).

I would also like to express special appreciation to all the technical and administrative staff in the Department of Materials at Imperial College, London for all their assistance and technical support. Special thanks to Dr. Mahmoud Ardakani and Mr. Steve Fay for their help in the specimen preparation process.

Finally, I am indebted to my parents (Kai Hsuan Wu and Chuan Chi Chou) for their support and encouragement. Without their decisions to give up their jobs and immigrated to Canada for the consideration of my brother's and my future education, I could not be able to achieve what I have completed thus far.

List of publications

This thesis describes research carried out by the author in the Department of Materials from October 2005 – September 2008 at Imperial College London under the supervision of Professor Alan Atkinson and Professor Roger Reed. No part of this thesis has been accepted or is being currently submitted for any other or qualification in this college or elsewhere.

The publications that have been prepared during the pursuit of this PhD degree are listed as follows:

1. **R.T. Wu**, X. Wang, A. Atkinson, On The Evolution of Bond Coat Compatibility for Thermal Barrier Coating Systems. *Surface and Coatings Technology (December 2008) Submitted*

2. **R.T. Wu**, K. Kawagishi, H. Harada, R.C. Reed, The retention of thermal barrier coating systems on single-crystal superalloys: Effects of substrate composition, *Acta Materialia Volume 56, Issue 14, August 2008, Pages 3622-3629.*

3. A. Mottura, **R.T. Wu**, M.W. Finnis, R.C. Reed, A critique of rhenium clustering in Ni-Re alloys using extended X-ray absorption spectroscopy, *Acta Materialia Volume 56, Issue 11, June 2008, Pages 2669-2675.*

4. **R.T. Wu**, R.C. Reed, On the compatibility of single crystal superalloys with a thermal barrier coating system, *Acta Materialia Volume 56, Issue 3, February 2008, Pages 313-323.*

5. **R.T. Wu**, R.C. Reed, K. Kawagishi, H. Harada, R. Wing, On the Compatibility of Nickel-Based Single Crystal Superalloys with Coating Systems. *7th International Charles Parsons Turbine Conference – Proceedings 2007.*

Table of Contents

List of Figures

List of Tables

Chapter 1 Introduction

1.1 Scope and Aims of Research

The objective of the present research is to investigate phenomena specifically related to the high temperature degradation of superalloys and coatings. One of the challenges in the field of high temperature structural materials will be addressed: that of assuring compatibility of the superalloys with the coatings required to protect them. These combinations of materials are required for hot section components in the latest generation of gas turbine engines, e.g. to power new aeroplanes and for ultra-efficient land-based turbines for electricity generation. Traditionally, superalloys and coatings have been designed in isolation with very little if any attention being paid to the factors which govern whether any given alloy can be coated or not.

The proposed work has the following aims.

First, oxidation behaviours of NiCrAl ternary alloys will be evaluated and assessed using a computer model to improve understanding of the oxidation mechanisms of high-temperature alloys in the first year of PhD project. In addition, the model will try to identify the redistribution of each alloying constituent and characterise the composition-dependent oxidation behaviour. Results of the modelling work will then be applied to explain aspects of high temperature exposure and oxidation phenomena pertinent to single crystal Ni-base superalloys and oxidation resistant bond coats, to provide further insight into the future alloy designs.

Second, thermal cycling experiments are carried out to evaluate how the substrate influences the spallation lifetime of coated commercial superalloys. Five commercial single crystal superalloys (SRR99, TMS-82+, PWA1484, CMSX-4 and TMS-138A) and three industry-standard bond coat systems (Pt-diffusion, High Temperature Low

Activity Pt-Al, and Low Temperature High Activity Pt-Al) have been selected to evaluate the dependence of TBC spallation lifetime on the type of substrate and coating applied.

Third, thermal cycling experiments are carried out to provide a detailed comparative study of the degradation process and failure mechanisms between these three industry-standard bond coats. The progressive evolution of stress in the alumina thermally grown oxide (TGO) upon thermal cycling and its relief by plastic deformation and fracture will be studied using luminescence spectroscopy and interfacial characterisation approach.

Chapter 2

Literature Review

2.1 Background information

The success of the turbine technology can be largely attributed to the development and utilization of nickel-base superalloys as the material for hot-section turbine components. Following the Kyoto Protocol aiming at mitigating CO_2 emission to prevent global warming, there is a considerable international effort aimed at improving the efficiency of the gas turbines used for jet propulsion and electricity generation, due to the price of fossil fuels and widespread environmental concerns about the effects of CO_2 emissions. As is widely known, high temperature materials are important in this, since fuel economy and rate of emissions scale directly with the temperature of the hot gas stream exiting the combustor regions; this effect explains the incentive to raise the operating temperatures experienced by the turbomachinery in these engines. In fact, a substantial enhancement of the engine is based on the increase of the maximum turbine entry temperature over the years as shown in Figure 2.1. It is not surprising therefore that all the major original equipment manufacturers (OEMs) possess research programmes which seek to develop new grades of alloy for use in their engines.

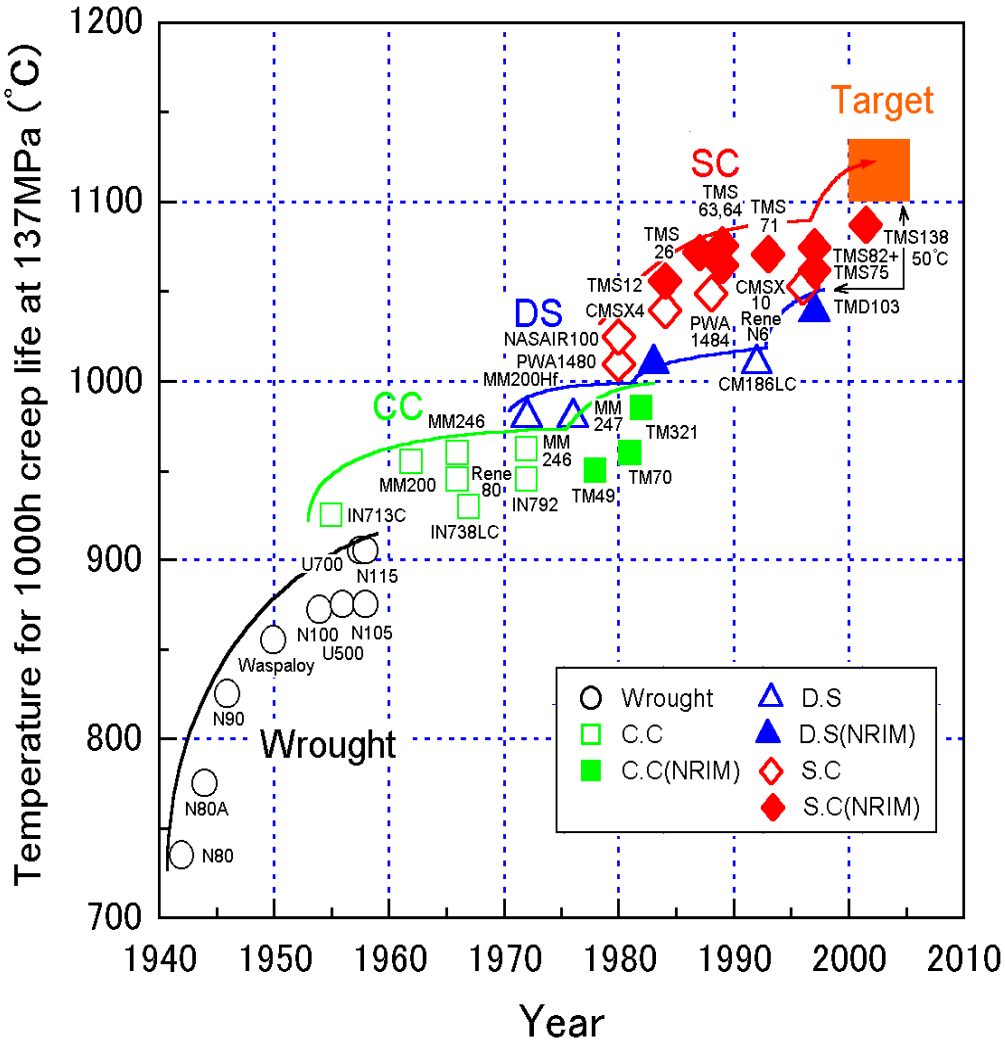

Figure 2.1 Evolution of the high-temperature capability of the superalloys over a period of 60 years since their emergence in the 1940s [1].

Nickel-based superalloys [2-5] play a vital role in this, since they have emerged as the materials of choice for the turbine blades, nozzle guide vanes and hot-section seals in the very hottest parts of these engines. These are amongst the most complex of the alloys produced by man, owing to the addition of many different alloying elements such as Co, Cr, Mo, W, Al, Ta, Re, Ru, which are added to provide a balance of properties,

e.g. creep resistance, tensile strength, fatigue capability, oxidation resistance, corrosion resistance and castability. While the alloy designer must consider all of these properties to meet simultaneously the turbine design specifications, advanced 4th and 5th generation Ni-base single crystal superalloys tend to exhibit improved creep resistance at a cost of sacrificing the high temperature oxidation resistance. Thus, advanced thermal barrier coatings (TBCs) – most usually based upon yttria-stabilised zirconia (YSZ) – must now be applied to the surface of alloy components as a functional material to further enhance the temperature capability of the turbine blade aerofoils.

2.2 Single Crystal Nickel-Base Superalloys

The terminology "superalloy" was first introduced after World War II to cover alloys designed specifically for aircraft turbine engines. Since then, the superalloys have been developed to expand their application to many different areas including aircraft and land-based gas turbine engines, rocket engines and petroleum plants. In this research, attention is given to nickel-base superalloys as this is the most popular class of superalloy being used nowadays.

Nickel, as the base element of Nickel-base superalloy, is the fifth most abundant element on earth. Its crystal structure is face-centered cubic (FCC), see Figure 2.2, from ambient conditions to its melting point of 1455ºC. Its density at ambient conditions is 8907 kg/m^3 which compared with other metals used for aerospace applications, e.g. Ti (4508 kg/m^3) and Al (2698 kg/m^3), is rather dense. This is due to the small inter-atomic distance, arising from the strong cohesion provided by the outer d-electrons, a typical characteristic of the transition metals.

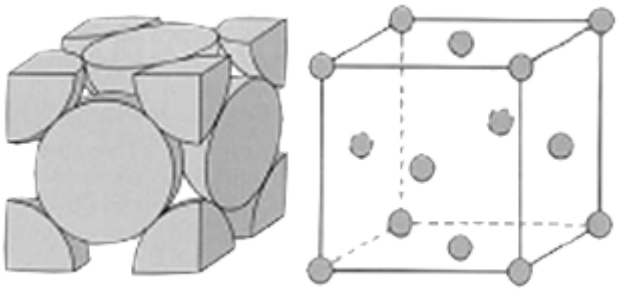

Figure 2.2 The Unit Cell of the Face-Centred Cubic (FCC) Crystal Structure

The compositions of the superalloys and the phases promoted by the presence of the alloying elements have been established over many years, and considerable use of them is required when designing new grades of superalloy. In the next section, the composition-microstructural relationships in nickel alloys and the method of controlling and promoting high temperature strength will be discussed.

2.2.1 Composition-Microstructure Relationships in Nickel Alloys

Most nickel-base superalloys contain ten or more deliberately added elements and can be considered one of the most complicated class of alloys ever engineered. The alloys generally contain significant amounts of chromium, aluminum, and titanium. Small amounts of boron, zirconium and carbon are often included. Other common additions are molybdenum, tungsten, tantalum, hafnium and niobium. Recently in the 4^{th} and 5^{th} generation of nickel-base superalloys, rhenium and ruthenium have also been introduced to improve high temperature phase stability in order to enhance the creep capability further [6, 7].

Broadly speaking, the elemental additions in Ni-base superalloys can be categorized as being i) γ formers (elements that preferentially partition to the austenitic γ matrix and thus stabilize it, or ii) γ' formers (elements partition to the γ' precipitate and promote the formation of ordered phases such as the compound Ni_3(Al, Ta, Ti). Figure 2.3 illustrates the computed Ni-Al binary diagrams determined using thermodynamic software such as the Thermo-Calc^{TM} package. Thermo-Calc^{TM} performs standard equilibrium

calculations and calculation of thermodynamic quantities based on thermodynamic databases.

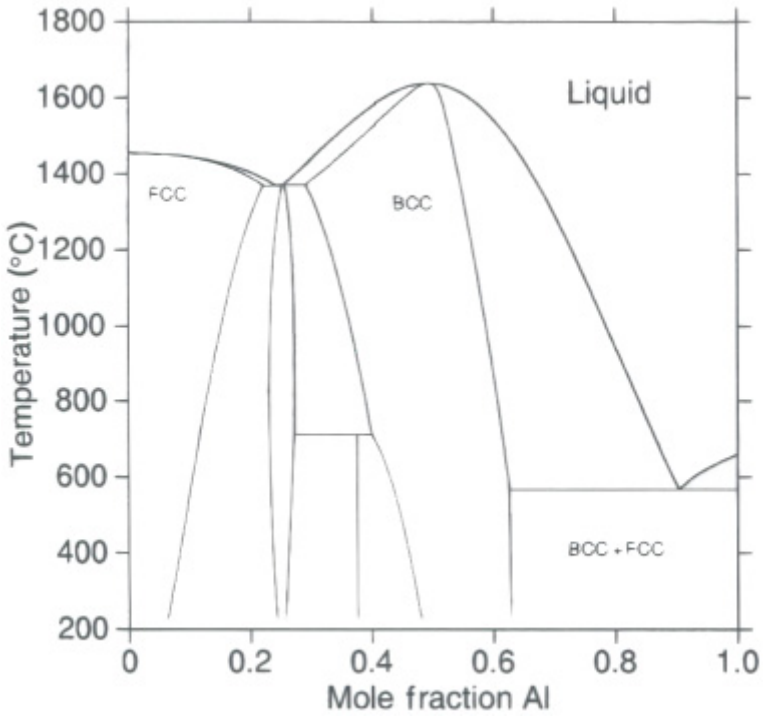

Figure 2.3 Ni-Al phase diagram the Thermo-calc^{TM} (thermodynamic) software.

The major phases present in typical superalloys are as follows [8]:

(i) The Gamma Phase (γ): This is usually the continuous matrix and exhibits the FCC structure. It contains significant concentrations of elements such as cobalt, chromium, molybdenum, tungsten, ruthenium and rhenium.

(ii) The Gamma Prime Phase (γ'): This forms as a precipitate intermetallic phase, e.g. Ni_3Al, in nickel-base superalloys which is often coherent with the γ-matrix with an ordered $L1_2$ crystal structure, as illustrated in Figure 2.4. The precipitate is enriched in elements such as titanium and tantalum.

(iii) Carbides. Carbon, present at levels of 0.05-0.2 wt% combines with reactive and refractory elements such as titanium, tantalum, and hafnium to form MC carbides. During

heat treatment and service, these decompose and form other carbides such as $M_{23}C_6$ and M_6C which tend to reside on the grain boundaries. These carbides are usually rich in chromium and molybdenum.

(iv) Topologically Close-Packed Phases (TCPs - μ, σ, Laves etc): These phases can be found in certain superalloys particularly in the service-aged condition. TCPs usually form as needle-like structures and are detrimental to the mechanical strength of the alloy. Thus, compositions of the superalloys are usually chosen to avoid formation of these compounds.

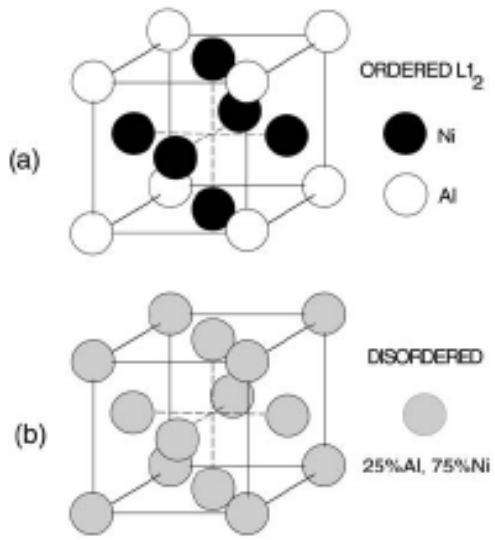

Figure 2.4 Arrangement of Ni and Al atoms in (a) the order Ni_3Al phase and (b) after disordering [5].

2.3 Oxidation Resistant Coatings and Thermal Barrier Coating Systems

Superalloys, although designed for high temperature applications, suffer chemical and mechanical degradation upon extended thermal exposure. With the modern jet engine operating (turbine entry gas temperature, TET ~ 1750K [9]) beyond the liquidus temperature (1600K) of the superalloy to achieve the designed thrust output and

maximise the fuel efficiency, hot section components exposed to this environment such as turbine blades and nozzle guide vanes are susceptible to creep and oxidation. To withstand this environment and to prevent the onset of melting, a reduction of metal temperatures is essential and can be achieved by the use of thermal barrier coatings (TBCs) in addition to surface thin-film air cooling [10-12]. The drop in the metal surface temperature significantly reduces metal oxidation rates and reduces susceptibility to creep. As shown in Figure 2.5, the turbine operating temperature is well above the melting temperature of the substrate, making it impossible for superalloys to survive in this environment without being protected by a thermal barrier coating.

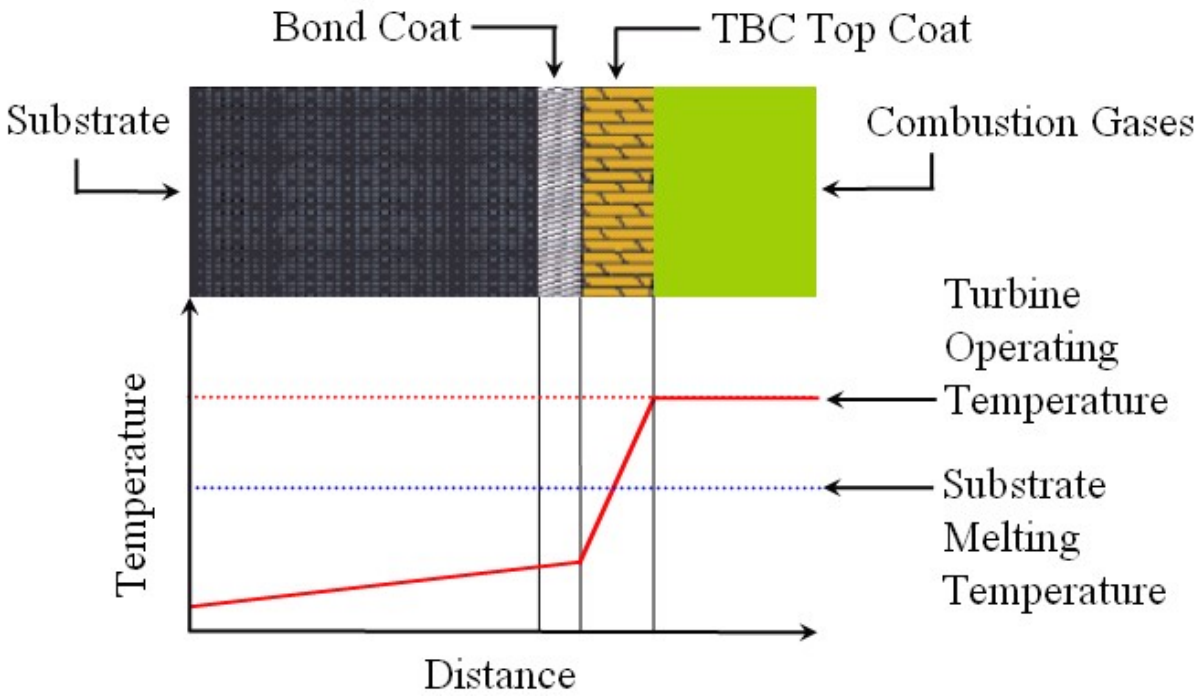

Figure 2.5 Temperature reduction by thermal barrier coatings [11]

Thermal barrier coatings (TBCs) are extensively used on advanced turbine components for propulsion and power generation applications [6-8]. State-of-the-art TBCs consist of a thermally insulating ceramic layer, usually made of zirconia containing about 7 wt% of yttria, also known as the yttria stabilized zirconia (YSZ). The second layer is the so-called intermetallic bond coat typically of a MCrAlY overlayed or a PtAl/Pt-diffused type, with the purpose of offering enhanced oxidation resistance due to its ability to form a slow-growing protective oxide scale. These layers are sequentially coated onto

the structural materials of Ni based alloys. Such an implementation enables an increase in the gas temperature of the jet engine and effectively results in an improvement of thermodynamic efficiency. YSZ is almost exclusively used as the top coat material for current TBC systems due to its low thermal-conductivity, high temperature phase stability and relatively good thermal-mechanical compatibility with the alloy substrate. Nonetheless, the oxygen transparent property and porosity of zirconia at elevated temperatures leads to the formation of a thermally grown oxide (TGO) layer between the YSZ top coat and the bond coat.

Deposition of the top coat layer is usually done by either an air plasma spray method (APS) or an electron beam physical vapour deposition process (EB-PVD). Coatings deposited by the APS method results in splats with inter-lamella gaps parallel to the substrate while EB-PVD produces a columnar structure with inter-column interfaces across the entire thickness of the coating. Figure 2.6 shows a comparison between the two distinct microstructures. It is this porous columnar structure that provides EB-PVD coatings with exceptional strain resistance because it gives a low elastic modulus.

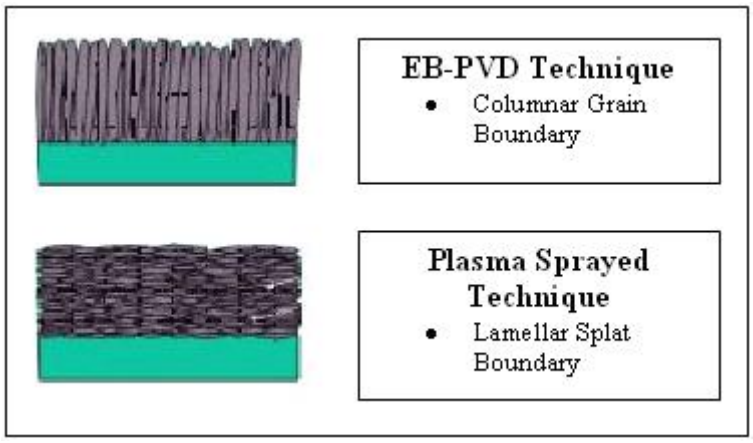

Figure 2.6 A comparison of TBC deposition techniques [12]

2.3.1 Overlay Bond Coats

Commonly used overlay coatings for the superalloys are metallic alloys of general composition MCrAlX, where M is usually Ni or a combination of both Ni and Co, and X is usually a reactive element added in minor proportions, such as silicon, zirconium, hafnium or yttrium. Yttrium is commonly used in modern TBCs as it enhances the adherence of the protective TGO alumina scale [13].

Due to the nature of the overlaid structure, the composition of the coating is largely independent of that of the alloy substrate, even though some inter-diffusion inevitably takes place during operation. Thus, this type of coating enables the desired surface properties to be attained for a given application. In the case of coated superalloys, a combination of oxidation and corrosion resistance and creep strength can be attained. Table 2.1 lists the composition of some overlay coatings [14].

Table 2.1 Compositions of some commonly used and prototype MCrAlY overlay bond coats [14], in weight %

	Ni	Co	Cr	Al	Y	Ti	Si	Hf	Others
NiCrAlY	Bal		25	6	0.4				
NiCrAlY	Bal		22	10	1.0				
NiCrAlY	Bal		31	11	0.6				
NiCrAlY	Bal		35	6	0.5				
CoNiCrAlY	32	Bal	21	8	0.5				
CoCrAlY		Bal	25	14	0.5				
NiCoCrAlTaY	Bal	23	20	8.5	0.6				4 Ta
NiCoCrAlYSi	Bal	0-40	12.5-20	2-8	0-0.25	0-10	2-10		0-4 Nb 0-4 Nb 0-20 Fe 0-5 Mn
NiCrAlTi	Bal		30-40	1-10		1-5			
NiCoCrAlHf	Bal	0-40	10-45	6-25				0-10	

2.3.2 Diffusion Bond Coats

In this study, the most important diffusion coatings are those which increase the surface concentration or activity of aluminium and reduce that of nickel. In contrast with the overlay coating, bond coat materials are diffused directly into the superalloy surface rather than being deposited as a discrete layer. Upon thermal exposure, a protective layer of alumina scale then forms readily on such a surface. Diffusion coatings as bond coats in the case of TBCs are often formed by electrodeposition of platinum before aluminisation. These elements become incorporated into the diffusion layer through the formation of a modified β-phase (Ni, Pt)Al.

It should be noted that the thicknesses of bond coats in the case of diffusion coatings is usually much thinner than those of overlay bond coats, 30-50 μm compared with 250 μm for instance [15]. Thus, the diffusion coatings may be more susceptible to depletion of aluminium in service.

A variation of this approach, patented by Rolls-Royce and Chromalloy UK [16] is to rely on the inward diffusion of platinum alone to improve oxidation resistance without undergoing any aluminising process. The theory behind the improved behaviour of this particular system is currently not fully understood and further research is necessary. However, a possible explanation could be that the aluminium diffuses from within the substrate to preferentially associate with the slow-diffusing platinum near the surface. Due to this process, the presence of platinum near the surface enhances the aluminium concentration so that it is maintained at a level in which preferential formation of a protective alumina scale could form. Again, full understanding of the details of this mechanism relies on further research.

2.4 Failure mechanisms

It is known that under the high-temperature service environment and cyclic operating profile typical of modern jet engines, creep and thermal fatigue play key, life-limiting, roles for the hot-section engine components in addition to the degradation by hot corrosion and oxidation. With the introduction of TBCs onto the surface of the alloy substrate being exposed to the hot gas, the composite structure results in a complex interplay between the inter-diffusion as well as internal stresses due to the mismatches in coefficients of thermal expansion (CTE). Thus, TBC coated components are subjected to several and potentially inter-related failure mechanisms due to their structural complexity [17-22].

2.5 Oxidation of Pure Metals

Oxidation means the loss of electrons. Oxidation of pure metals is a chemical reaction in which the metal loses one or more electrons, such that the atom of the metal change from the neutral state to a positively charge ion and react with oxygen to form an oxide of the metal. In the simplest process, the reaction can be described by the following reaction.

$$aM + bO_2 = M_aO_{2b}$$

The oxide can form as a protective and adherent scale that slows down further oxidation, or may spall off repeatedly, exposing fresh metal surface to react with oxygen. For the non-porous and adherent scales, oxidation progresses from direct exposure of the metal to oxygen to a solid-state diffusion limited mechanism. The latter involves either the diffusion of cations through the oxide scale towards the gas or the diffusion of gas through the oxide. In addition to the oxide scale protectiveness, the rate of subsequent oxidation also depends on other parameters such as the oxide thickness, the surface area, the environmental temperature and the gas composition.

In many situations, especially in the case of alloys, more than one oxidation mechanism

may take place at once and thus, complicates the study of oxidation. However, by breaking down the overall oxidation process into individual investigations of thermodynamics, kinetics and evolving microstructure, it is possible to predict the types of oxidation reaction that occur and obtain a quantitative evaluation of how quickly a reaction is likely to proceed.

2.6 Thermodynamic Fundamentals

For the oxidation reaction

$$aM + \frac{b}{2}O_2 = M_aO_b$$

the equilibrium constant can be written as a function of the reactant activity;

$$K_T = \frac{aM_aO_{2b}}{aM\,P_{O_2}^b}$$

For pure metal and pure oxide, the activities of both metal and oxide are unity; thus, the equation can be simplified accordingly, with the oxygen activity expressed as its partial pressure in units of atmospheres (P_{O2})

$$K_T = \frac{1}{P_{O_2}^b}$$

In addition, the change of the Gibbs free energy per mole of reaction can be expressed as

$$\Delta G_f = \Delta G_f^o - RT \ln\left(\frac{1}{P_{O_2}^b}\right)$$

When the above reaction is at equilibrium, the change of the Gibbs free energy, ΔG_f, is equal to zero.

$$\Delta G_f^o = RT \ln\left(\frac{1}{P_{O_2}^b}\right)$$

It can thus be seen that the thermodynamic analyses of the oxidation reaction of a

simple system can be reduced to a dependence on the temperature and oxygen partial pressure. The equilibrium oxygen partial pressure of an oxide is known as the dissociation pressure which is a measure of oxide stability. The lower the dissociation pressure, the greater the thermodynamic stability of the oxide is and vice versa.

2.7 Wagner Theory of Parabolic Oxidation

The high temperature oxidation kinetics of a metal depends largely on the properties of the oxide scale. In the case of an adherent oxide and assuming the reactions taking place at the metal/oxide and oxide/gas interfaces are effectively instantaneous, the rate controlling process of the overall oxidation reaction depends on transport of reacting species through the oxide scale.

Thus, as the oxide scale grows thicker and correspondingly, the diffusion distance becomes longer, the oxidation kinetics (i.e. the rate of oxide thickness growth, dx/dt) change inversely proportionally to the overall oxide scale thickness. Experimentally, it is often observed that the rate of oxidation follows such a parabolic rate law, which can be quantitatively defined by a parabolic rate equation,

$$x^2 = k_p t$$

Where x is the thickness of the oxide scale and k_p is the parabolic rate constant.

Wagner [23] provided a theoretical treatment for this rate constant and derived a steady-state oxidation rate-expression as a function of the concentration of metal and oxygen species in the oxide lattice, diffusion coefficients of oxygen and metal ions in the oxide and thermodynamic equilibria at both the metal/oxide and oxide/gas interfaces.

Based on this local equilibrium assumption, thermodynamic activity gradients of either the nonmetal or metal can be established across the oxide layer. Since the transport of metal cations and oxygen anions are in different directions, an electric field is produced

across the oxide scale. Due to the presence of this electric field, electrons move across the oxide from the metal to the atmosphere. The transport of electrons is balanced by the charge equivalent migration of ions; thus, overall electric neutrality is maintained.

Wagner's derivation [23] of the parabolic rate constant, k', for cationic and anionic diffusion controlled oxidation are described in equations below respectively. Note that $k_p = 2k'$.

$$k' = \frac{1}{RT}\int_{\mu''_M}^{\mu'_M} D_M d\mu_M$$

$$k' = \frac{1}{RT}\int_{\mu'_X}^{\mu''_X} D_X d\mu_X$$

where D_M and D_X are the diffusion coefficient of metal M and non-metal X in the oxide scale respectively and μ_M and μ_X are the chemical potential of metal M and non-metal X.

Oxidation morphology and the oxidation rate constants of many metals have been published in previous studies [24-35] forming large database related to the oxidation of metallic materials. However, it should be indicated here that there are also many systems deviate greatly from the Wagner's model, especially for systems incapable to form coherent oxides; thus, the diffusion controlled assumption of the Wagner's theory is not satisfied.

2.8 Oxidation of Alloy Systems

High temperature oxidation of engineering alloys is an important field of study. The oxidation resistance of an alloy depends on its ability to form a stable, adherent, slow-growing oxide layer upon thermal exposure. Oxidation of binary alloys has been studied extensively and theoretical understanding is well established. In addition, numerical models capable of predicting composition changes in single binary [23, 36-39] and dual-phase binary [40, 41] systems have been developed. For instance, a criterion has been devised to predict the minimum concentration of the less noble solute constituent required in a binary alloy to form a single external layer of the most stable oxides [42]. However, despite the fact that current engineering structural alloys consist almost exclusively of three or more elements to provide adequate mechanical properties and corrosion/oxidation resistance, very few theoretical foundations have been established to explain the oxidation of ternary alloys due to the difficulty in understanding interactions between alloying species and the competition between developing oxides. In particular, the competition between formation of oxides of different compositions in the early stage of oxidation has not been fully understood and thus the bulk chemical composition dependence of oxidation behaviour cannot be formulated analytically. Moreover, the oxidation kinetics of a ternary alloy, in contrast to a binary system, depend strongly on the interaction between competing oxides and are a function of the growth rate of each of the developing oxides.

2.9 Oxidation of Ni-Cr-Al Alloy Systems

Giggins and Pettit, in a series of papers [43-47], classified Ni-Cr-Al alloys based on the oxide morphology and oxidation mechanisms at 1000ºC. With the study of binary Ni-Al and Ni-Cr alloys and further experimental examination of the oxidation behaviour of ternary Ni-Cr-Al alloys, they provided a general description that classified the oxidation behaviour into three groups (i.e. Group I, II, and III) based on the type of oxides formed (Figure 2.7).

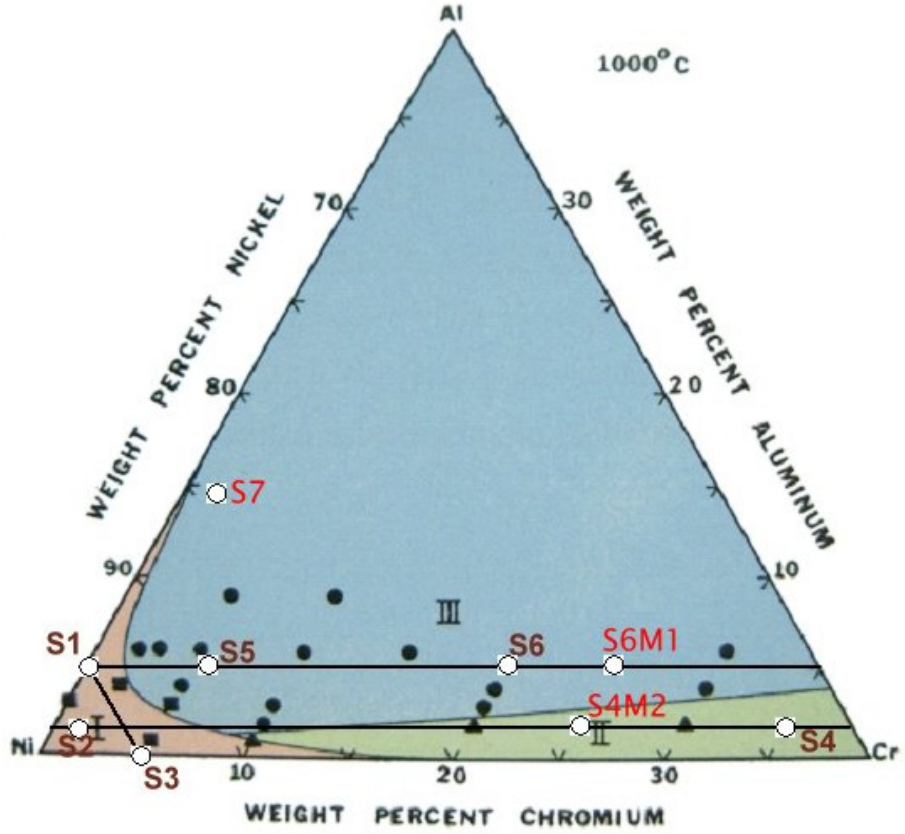

Figure 2.7 Ternary phase diagram showing the group I, II and III oxidation behaviour [44]. (Note: Points shown are experimental observations used to construct this diagram)

A schematic diagram of the proposed oxidation process of Group I, II and III alloys is shown in Figure 2.8 [44]

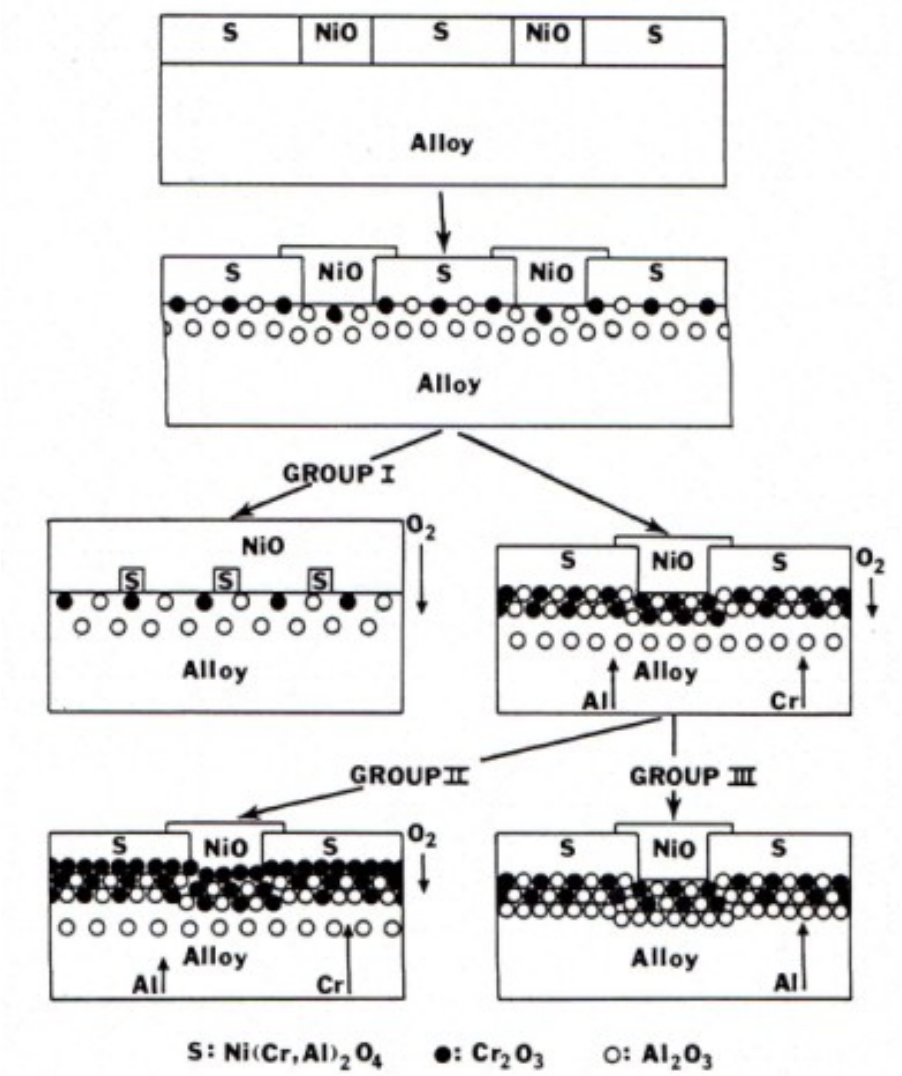

Figure 2.8 Proposed mechanisms of the oxidation process [44]

Group I is composed of alloys which formed a continuous and compact layer of NiO accompanied by a complex subscale consisting of Cr_2O_3, Al_2O_3 or $Ni(Al,Cr)_2O_4$ spinels. This group of alloys has relatively low concentration of chromium and aluminium which quickly deplete to zero near the oxide-metal interface upon rapid initial oxidation. Since the concentrations are not sufficient to form a compact and continuous layer of Al_2O_3 or Cr_2O_3, the diffusion of nickel to form NiO in these alloys is favoured.

As shown in Figure 2.9 (left), the binary Ni-5wt% Al alloy preferentially formed a compact and continuous NiO layer with a thin Ni-enriched layer underneath it and internally precipitated Al_2O_3. The binary Ni-5wt% Cr alloy, similarly, failed to

preferentially form a Cr_2O_3 layer, but instead a spinel of Cr enriched NiO layer, with internal precipitation of Cr_2O_3 subscale.

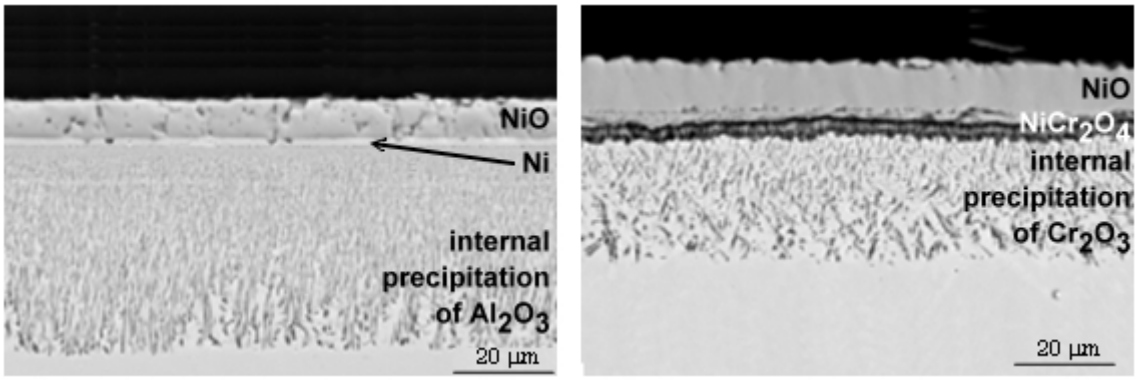

Figure 2.9 From left to right: the oxidation morphology of Ni-5wt% Al and Ni-5wt% Cr alloys upon isothermal oxidation at 1100°C for 1 hr [48].

Group II alloys cover a wide range of chromium concentration, but generally have relatively low concentration of aluminium. The chromium concentration is higher than that of aluminium in this group of alloys. In terms of the oxide morphology, an external layer of Cr_2O_3 and internal precipitation of Al_2O_3 are observed upon thermal exposure as shown in Figure 2.10. Although the oxide morphology during the initial rapid oxidation may be similar to that of Group I, the increased concentration of chromium in this group of alloys ensures that there is more chromium present at the oxide-metal interface for oxidation of Cr_2O_3 to take place, and thus, favours the formation of a continuous Cr_2O_3 oxide layer. With the formation of the Cr_2O_3 layer, diffusion of nickel through the layer from the bulk alloy to the oxide-metal interface slows down dramatically. As a result, only a very thin outer layer of NiO is usually observed.

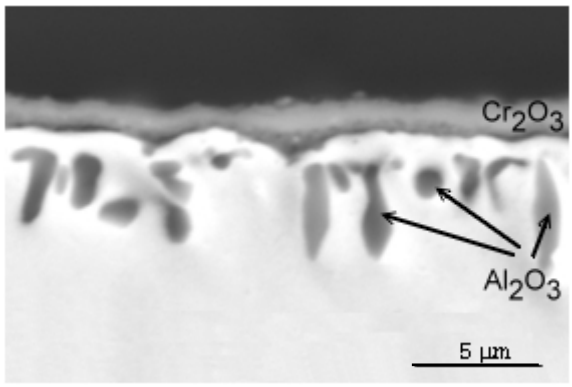

Figure 2.10 The oxidation morphology of a Ni-35wt% Cr-2.5wt% Al alloy upon isothermal oxidation at 1100°C for 1 hr [48].

The oxidation of group III alloys results in the preferential formation of a compact external Al_2O_3 scale, and differs from Group I & II since no internal subscale is observed. Figure 2.11 shows a compact external Al_2O_3 scale grew on the surface of a Ni-2.5wt% Cr-15wt% Al alloy without any internal precipitation of oxides after isothermal oxidation at 1100°C for 1 hour. However, external Cr_2O_3, $NiCr_2O_4$ and even NiO may be observed depending on the relative concentration of aluminium and chromium. The reason is the formation of external Cr_2O_3, $NiCr_2O_4$ and even NiO layers above the alumina scale associated with the diffusion of chromium and nickel through the initially formed Al_2O_3 layer, consistent with the thermodynamic description (i.e. equilibrium partial pressure of oxygen) of the Ni-Al-Cr-O system.

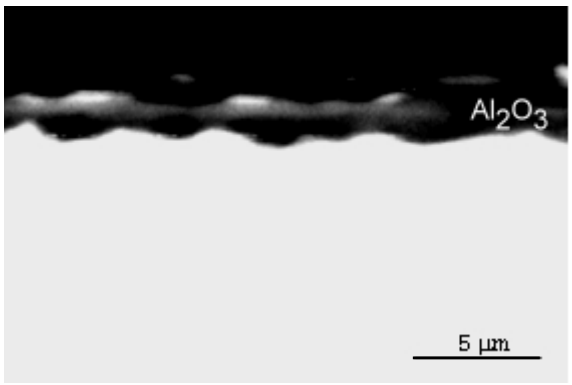

Figure 2.11 The oxidation morphology of a Ni-2.5wt% Cr-15wt% Al alloy upon isothermal oxidation at 1100°C for 1 hr [48].

2.10 The Gettering Effect

One of the important conclusions from the work of Giggins and Pettit was the ability for chromium to encourage the premature external oxidation of aluminium, known as the 'gettering effect'. Due to the presence of chromium, the minimum concentration of aluminum to preferentially form external alumina scale decreases from 15 wt% of the binary Ni-Al alloy. Upon further alloying addition of chromium, the minimum Al concentration necessary to stay in the group III region decreases, until the group II behaviour takes over eventually.

Thus, the presence of a third element, in this case chromium promotes the establishment of a protective alumina scale in alloys of lower aluminum concentration. The classic theory is when Al and Cr compete to form external oxide of either Al_2O_3 or Cr_2O_3, the unsuccessful Cr then precipitates to form internal oxide and act as a secondary getter for oxygen, thereby decreases the inward flux of oxygen diffusion into the alloy. In the case of a group III alloy, this allows aluminium ions to diffuse outward to form external alumina layer without getting precipitated internally [49-51].

2.11 High temperature cyclic oxidation of coating systems

Long term durability of coating systems depends on the stability of the interface between the protective coating and the substrate materials. In the case of TBC systems, one particular degradation mechanism is associated with progressive interfacial roughening, or rumpling of the bond coat because such interfacial distortion due to biaxial compression can induce tensile stresses perpendicular to the interface [52-56]. This nucleates cracks and eventually leads to the spallation failure of TBCs [57-60]. Such rumpling instability has been previously reported in aluminide [57, 61-63], MCrAlY [62] and Pt-modified [64] coating systems. In the literature, this type of degradation has been attributed to the thermal expansion mismatch between the bond coat and substrate [61, 62], repeated oxide cracking [57, 63], martensitic transformation in aluminides [65] and decomposition of the β-(Ni, Pt)Al phase [66].

The effect of oxidation on the rumpling mechanism of Pt-modified bond coat systems has been studied by Tolpygo et al. [64] in which the role of oxidation was evaluated by conducting cyclic testing in an inert atmosphere. By comparing specimens thermal cycled in vacuum with control specimens thermal cycled in standard atmosphere condition, they found that thermal cycling in vacuum is sufficient to cause rumpling. Based on this observation, it was suggested that the rumpling mechanism is driven by an interaction between the bond coat and the substrate.

In Ni-rich β phase nickel aluminides, cooling from temperatures above 1100°C results in a reversible phase transformation, known as the martensitic transformation when the Al content is less than about 37 at% [67]. Such kind of phase transformation does not involve diffusion of atoms, but occurs by local displacement of coordinated atoms. This means the B2 (body-centered cubic) phase changes to an $L1_0$ (face-centered tetragonal) as illustrated in Figure 2.12. The martensitic transformation is accompanied by a characteristic volume change because the molar volume of β is about 2% larger than that of the martensitic phase [65].

Similarly, Pt-modified nickel aluminide bond coat systems also experience martensitic transformation upon cooling from temperatures above 1000-1050°C [65, 68, 69]. To study whether the martensitic transformation induced strain causes rumpling in the bond coat, it is possible to compare the surface roughness of bond coats thermal cycled entirely above the martensitic transformation temperature with that of the bond coats thermal cycled in the transformation range. Such an experiment was carried out using Pt-Al bond coats as reported in [64], which showed that with and without the transformation, similar bond coat surface roughness was obtained after the same number of cycles.

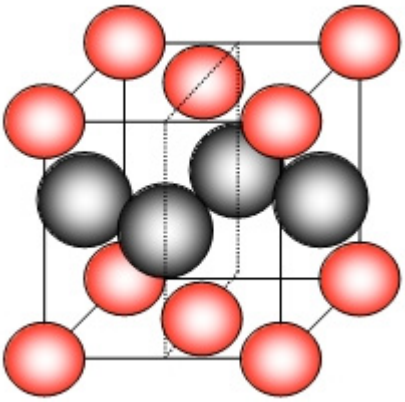

Figure 2.12 The Unit Cell of the $L1_0$ Face-Centred Tetragonal (FCT) Crystal Structure.

More recently, it has been reported [70] that the rumpling is sensitive to the hafnium and carbon content of the substrate alloy. It was found that alloys containing low hafnium and high carbon concentrations showed largest rumpling while high hafnium and low carbon alloys showed the opposite. It was argued in the literature that hafnium diffuses into the bond coat and the growing alumina oxide layer; thus, increasing their creep resistance. Carbon, on the other hand, was thought to form tantalum-rich carbides, which tie up hafnium, therefore, decrease the amount of hafnium available to diffuse into the bond coat and oxide layer.

2.12 Project Objectives

In this project, high temperature oxidation and failure mechanism of Ni-Cr-Al alloy systems and EBPVD YSZ TBCs deposited on Pt-diffusion and Pt-Al bond coats on different single crystal superalloys are studied. The importance of superalloy composition on the TBC life has received considerably less attention in the field of high temperature materials while the failure characteristics and mechanism have yet to be compared and analysed in details.

The overall objective of this research can be divided into 5 sub objectives which are listed below:

1. To develop a computer model to characterise the composition-dependent oxidation behaviour and to identify the redistribution of each alloying constituent.
2. To evaluate the compatibility of nickel-based single crystal superalloys with TBC system.
3. To investigate the role of the compositions of these alloys in determining the TBC's spallation resistance.
4. To compare the degradation process and failure mechanisms of three industry-standard bond coats (Pt-diffusion, High Temperature Low Activity Pt-Al, and Low Temperature High Activity Pt-Al).
5. To characterise the progressive evolution of stress in the alumina thermally grown oxide (TGO) upon thermal cycling and its relief by plastic deformation and fracture using luminescence spectroscopy and other interfacial characterisation approaches.

References for Chapter 2

[1] High Temperature Materials Center. National Insitute for Materials Science. 26 April 2006 <http://sakimori.nims.go.jp/htm21-e.html >.

[2] W. Betteridge and S. W. S. Shaw, "Development of superalloys," Materials Science and Technology, Volume 3, 1987, Pages 682-694.

[3] C.T. Sims, N.S. Stoloff and W. C. Hagel, eds, Superalloys II: High-Temperature Materials for Aerospace and Industrial Power (New York: John Wiley and Sons 1987).

[4] K.A. Green, T.M. Pollock, H. Harada et al., eds., Superalloys 2004, Proceedings of the Tenth International Symposium on the Superalloys (Warrendale, PA: The Minerals, Metals and Materials Society (TMS), 2004).

[5] R.C. Reed, Superalloys: fundamentals and applications, Cambridge University Press, Cambridge (2006).

[6] M.S.A. Karunaratne, C.M.F. Rae and R.C. Reed, "On the microstructural instability of an experimental nickel-based single-crystal superalloy," Metallurgical Materials Transactions A, Volume 32, 2001, Pages 2409-2421

[7] S. Walston, A. Cetel, R. MacKay, K. O'Hara, D. Duhl and R. Dreshfield: Superalloys 2004 (TMS, Warrendale, Pittsburg, 2004) Pages 15-24

[8] M. Durand-Charre, "The Microstructure of Superalloys." Gordon and Breach (1997)

[9] N.A. Cumpsty, Jet Propulsion: A Simple Guide to the Aerodynamic and Thermodynamic Design and Performance of Jet Engines (Cambridge: Cambridge University Press, 1997)

[10] W. Beele, G. Marijinissen, A. van Lieshout, "The evolution of thermal barrier coatings," Surface & Coating Technology, Volume 120-121, 1999, Pages 61-67

[11] P. Kennard Wright, "Influence of cyclic strain on life of a PVD TBC," Materials Science and Engineering A, Volume 245, 1998, Pages 191-200

[12] A.G. Evans, D.R. Mumm, J.W. Hutchinson, G. H. Meier, F. S. Pettit, "Mechanisms controlling the durability of thermal barrier coatings," Progress in Materials Science, Volume 46, 2001, Pages 505-553

[13] A. Strawbridge, and P.Y. Hou, "The role of reactive elements in oxide scale adhesion," Materials at High Temperatures, Volume 12, 1994, Pages 177-181

[14] A.R. Nicholl, H. Gruner, G. Wuest and S. Keller, "Future developments in plasma

spray coating," Materials Science and Technology, Volume 2, 1986, Pages 214-219
[15] H. Evans, and M. Taylor, "Oxidation of high-temperature coatings," Proceedings of the I MECH E Part G, Journal of Aerospace Engineering, Volume 220, 2006, Pages 1-10
[16] D.S., Rickerby, and R.G. Wing, "Article including thermal barrier coating substrate." US Patent. 5 981 091, 9 November 1999
[17] A.M. Karlsson and A.G. Evans, "A numerical model for the cyclic instability of thermally grown oxides in thermal barrier systems," Acta Materialia, Volume 49, 2001, Pages 1793-1804
[18] N. Czech, H. Fietzek, M. Juez-Lorenzo, V. Kolarik and W. Stamm, "Studies of the bond-coat oxidation and phase structure of TBCs," Surface and Coatings Technology, Volume 113, 1999, Pages 157-164
[19] V. Lughi, V.K. Tolpgo, D.R. Clarke, "Microstructural aspects of the sintering of thermal barrier coatings," Materials Science & Engineering A, Volume 368, 2004, Pages 212-221
[20] K.T. Voisev, T.W. Clyne, "Laser drilling of cooling holes through plasma sprayed thermal barrier coatings," Surface and Coatings Technology, Volume 176, 2004, Pages 296-306
[21] A. Nusair Khan, J. Lu and H. Liao, "Heat treatment of thermal barrier coatings," Materials Science & Engineering A, Volume 359, 2004, Pages 129-136
[22] M. Andritschky, P. Alpuim, D. Stover, C. Funke, "Study of the mechanics of the delamination of ceramic functional coatings," Materials Science and Engineering A, Volume 271, 1999, Pages 62-69
[23] C. Wagner, "Theoretical analysis of the diffusion processes determining the oxidation rate of alloys," Journal of The Electrochemical Society, Volume 99, 1952, Pages 369-380
[24] C.M.J. Graham and M. Cohen, "The effect of oxygen pressure on the oxidation of iron at 350ºC and 400 ºC," Journal of The Electrochemical Society, Volume 116, 1960, Pages 1430-1435
[25] S. Chang, W.H. Wade, "Kinetics of interaction of oxygen with evaporated iron films," Journal of Physical Chemistry, Volume 74, 1970, Pages 2484 - 2488
[26] B. Deal, "The oxidation of silicon in dry oxygen, wet oxygen, and steam," Journal of The Electrochemical Society, Volume 110, 1963, Pages 527-533

[27] B.E. Deal and A.S. Grove, “General relationship for the thermal oxidation of silicon,” Journal of Applied Physics, Volume 36, 1965, Pages 3770-3778

[28] W.J. Moore, “Oxidation of metals at high temperatures,” Journal of The Electrochemical Society, Volume 100, 1953, Pages 302-313

[29] E.A. Gulbransen and K.F. Andrew, “The kinetics of oxidation of high purity nickel,” Journal of The Electrochemical Society, Volume 101, 1954, Pages 128-140

[30] P. Kofstad, “Oxidation of Metals: Determination of activation energies,” Nature, Volume 179, 1957, Pages 1362 - 1363

[31] A. Dravnieks, “Correlations between parabolic oxidation of metals and properties of oxides,” Journal of The Electrochemical Society, Volume 100, 1953, Pages 95-102

[32] A.Z. Hed, “On the deviations from parabolic oxidation of Co-25 w/o Cr at high temperature,” Journal of The Electrochemical Society, Volume 118, 1971, Pages 737-739

[33] W. Boggs, “The Oxidation of iron-aluminum alloys from 450ºC to 900ºC,” Journal of The Electrochemical Society, Volume 118, 1971, Pages 906-913

[34] J. E. Lopes Gomes, A. M. Huntz, "Correlation between the oxidation mechanism of titanium under a pure oxygen atmosphere, morphology of the oxide scale, and diffusional phenomena," Oxidation of Metals, Volume 14, 1980, Pages 249-261

[35] R.C. Svedberg: Proc. Symp. On properties of high temperature alloys with emphasis on environmental effects, Vol. 77-1, 331-385, Eds. Z. A. Foroulis and F. S. Pettit (1977)

[36] B.D. Bastow, D.P. Whittle, G.C. Wood, “Alloy depletion profiles resulting from the preferential removal of the less noble metal during alloy oxidation,” Oxidation of Metals, Volume 12, 1978, Pages 413-438

[37] G. Wang, B. Gleeson, and D.L. Douglass, “An extension of Wagner’s analysis of competing scale formation,” Oxidation of Metals, Volume 35, 1991, Pages 317-332

[38] D.P. Whittle, D.J. Evans, D.B. Scully and G. C. Wood, “Compositional changes in the underlying alloy during the protective oxidation of alloys.” Acta Materialia, Volume 15, 1967, Pages 1421-1430

[39] G.L. Wulf, M.B. McGirr, and G.R. Wallwork, “Theoretical analysis of alloy oxidation with reference to Fe-Cr alloys.” Corrosion Science, Volume 9, 1969, Pages 739-754

[40] G. Wahl, “Coating composition and the formation of protective oxide layers at high temperatures,” Thin Solid Films, Volume 107, 1983, Pages 417-426
[41] P. Carter, B. Gleeson, and D.J. Young, “Calculation of precipitate dissolution zone kinetics in oxidising binary two-phase alloys.” Acta Materialia, Volume 44, 1996, Pages 4033-4038
[42] N. Matan, H.M.A. Win and, P. Carter, M. Karunaratne, P.D. Bogdanoff and R.C. Reed, “A coupled thermodynamic/kinetic model for diffusional processes in superalloys,” Acta Materialia, Volume 46, 1998, Pages 4587-4600
[43] F.S. Pettit, “Oxidation mechanisms of nickel-aluminium alloys at temperatures between 900ºC and 1300ºC,” Transactions AIME, Volume 239, 1967, Pages 1297-1305
[44] C.S. Giggins and F.S. Pettit, “Oxidation of Ni-Cr-Al alloys between 1000ºC and 1200ºC,” Journal of The Electrochemical Society, Volume 118, 1971, Pages 1782-1790
[45] C.S. Giggins and F.S. Pettit, Trans. AIME 245, 2695 (1969); Pratt and Whitney Aircraft, Advanced Materials Research and Development Laboratory, Report No. 68-024 (October, 1968).
[46] C.S. Giggins, B.H. Kear, F.S. Pettit and J.K. Tien, “Factors affecting adhesion of oxide scales on alloys,” Metallurgical and Materials Transactions B, Volume 5, 1974, Pages 1685-1688
[47] F.S. Pettit and C.S. Giggins, “Hot corrosion,” C. T. Sims, N.S. Stoloff and W.C. Hagel, eds, Superalloys II, 1987, Pages 327-358
[48] R.T. Wu, “Coatings for High Temperature Applications.” MPhil to PhD transfer report, Imperial College London, 2006 November
[49] F.H. Stott, G.C. Wood, and J.Stringer, “The influence of alloying elements on the development and maintenance of protective scales,” Oxidation of Metals, Volume 44, 1995, Pages 113-145
[50] C. Wagner, “Passivity and inhibition during the oxidation of metals at elevated temperatures,” Corrosion Science, Volume 5, 1965, Pages 751-764
[51] F.H. Stott and G.C. Wood “The mechanism of Ni-Cr-Al alloys at 1000ºC – 1200ºC,” Corrosion Science, Volume 11, 1971, Pages 799-812
[52] A.G. Evans, G.B. Crumley and R.E. Demaray, “On the mechanical behavior of brittle coatings and layers,” Oxidation of Metals, Volume 20, 1983, Pages 193-216
[53] X.-Y. Gong and D.R. Clarke. “On the measurement of strain in coatings formed on

a wrinkled elastic substrate," Oxidation of Metals, Volume 50, 1998, Pages 355-376
[54] A.G. Evans, M.Y. He, J.W. Hutchinson, "Effect of interface undulations on the thermal fatigue of thin films and scales on metal substrates," Acta Materialia, Volume 45, 1997, Pages 3543-3554.
[55] Z. Suo, "Wrinkling of the oxide scale on an aluminum-containing alloy at high temperatures," Journal of the Mechanics and Physics of Solids, Volume 43, 1995, Pages 829-846.
[56] M.Y. He, A.G. Evans, J.W. Hutchinson, "The ratcheting of compressed thermally grown thin films on ductile substrates," Acta Materialia, Volume 48, 2000, Pages 2593-2601.
[57] J.W. Holmes and F.A. McClintock, "The chemical and mechanical processes of thermal fatigue degradation of an aluminide coating," Metallurgical and Materials Transactions A, Volume 21, 1990, Pages 1209-1222
[58] D.R. Mumm, A.G. Evans, and I.T. Spitsberg, "Characterization of a cyclic displacement instability for a thermally grown oxide in a thermal barrier system," Acta Materialia, Volume 49, 2001, Pages 2329-2340
[59] V.K. Tolpygo, and D. R. Clarke, "Morphological evolution of thermal barrier coatings induced by cyclic oxidation," Surface and Coatings Technology, Volumes 163-164, 2003, Pages 81-86.
[60] J.A. Ruud, A. Bartz, M.P. Borom and C.A. Johnson, "Strength degradation and failure mechanisms of electron-beam physical-vapor-deposited thermal barrier coatings," Journal of the American Ceramic Society, Volume 84, 2001, Pages 1545-1552
[61] P. Deb, D.H. Boone, and T.F. Manley II, "Surface instability of platinum modified aluminide coatings during 1100ºC cyclic testing," Journal of Vacuum Science and Technology A, Volume 5, 1987, Pages 3366-3372
[62] R.C. Pennefather, D.H. Boone, "Mechanical degradation of coating systems in high-temperature cyclic oxidation," International Journal of Pressure Vessels and Piping, Volume 66, 1996, Pages 351-358
[63] Y.H. Zhang, P.J. Withers, M.D. Fox and D.M. Knowles, "Damage mechanisms of coated systems under thermomechanical fatigue," Materials Science and Technology, Volume 15, 1999, Pages 1031-1036

[64] V.K. Tolpygo, D.R. Clarke, “On the rumpling mechanism in nickel-aluminide coatings: Part I: an experimental assessment,” Acta Materialia, Volume 52, 2004, Pages 5115-5127.

[65] M.W. Chen, M.L. Glynn, R.T. Ott, T.C. Hufnagel, K.J. Hemker, “Characterization and modeling of a martensitic transformation in a platinum modified diffusion aluminide bond coat for thermal barrier coatings,” Acta Materialia, Volume 51, 2003, Pages 4279-4294.

[66] V.K. Tolpygo, D.R. Clarke, “Surface rumpling of a (Ni, Pt)Al bond coat induced by cyclic oxidation,” Acta Materialia, Volume 48, 2000, Pages 3283-3293.

[67] S. Bose, High Temperature Coatings, Butterworth-Heinemann, (2007).

[68] D. Pan, M.W. Chen, P.K. Wright, K.J. Hemker, “Evolution of a diffusion aluminide bond coat for thermal barrier coatings during thermal cycling,” Acta Materialia, Volume 51, 2003, Pages 2205-2217.

[69] Y. Zhang, J.A. Haynes, B.A. Pint, I.G. Wright, W.Y. Lee, “Martensitic transformation in CVD NiAl and (Ni,Pt)Al bond coatings,” Surface and Coatings Technology, Volumes 163-164, 2003, Pages 19-24.

[70] V.K. Tolpygo, K.S. Murphy, D.R. Clarke, “Effect of Hf, Y and C in the underlying superalloy on the rumpling of diffusion aluminide coatings,” Acta Materialia, Volume 56, 2008, Pages 489-499.

Chapter 3

A Coupled Thermodynamic-Kinetic Model for the Oxidation Kinetics of Ternary Nickel-Rich Alloys

3.1 Introduction

Oxidation of engineering alloys is an important subject of study in the field of high temperature materials. Numerical modelling efforts of these alloys tended to be limited to single binary [1-5] and dual-phase binary [6, 7] systems due to the difficulty in formulating the composition-dependent oxidation behaviour of ternary systems. Moreover, the competition between formation of oxides of different compositions also present a challenge in deriving numerical procedures.

However, as mentioned previously, since most structural alloys consist almost exclusively of three or more elements to achieve the required properties, analytical models capable of characterising and predicting diffusion and oxidation processes of ternary alloy systems would offer a tremendous benefit to the field of alloy design.

In year 2000, a finite-difference computer program was written by the National Aeronautics and Space Administration (NASA) to be a pioneer model dealing with the diffusion and high temperature oxidation processes of an overlay type of bond coat represented by the Ni-Cr-Al ternary system [8]. The model makes the simplification of using an exclusive Al_2O_3 formation model and assumes a parabolic growth rate. Oxides other than alumina were not considered, thus, suggesting that the only surface flux in the ternary diffusion calculation is loss of aluminium to form the alumina scale.

A successor model to the NASA program was designed by Nijdam et al. [9],

representing an improvement of the oxidation treatment by including formation of Cr_2O_3, and NiO in addition to Al_2O_3. The amount of each oxide phase developed as a function of oxidation time is then coupled with the diffusion equations to calculate the composition-depth profiles in the alloys. The model, however, does not consider formation of spinel oxides.

In this work, a finite difference computer code has been written to model the assumed one-dimensional diffusion and oxidation processes of a ternary alloy (i.e. Ni-Al-Cr) upon isothermal oxidation exposure with the aim of predicting the composition profile change in the alloy substrate. The calculation is based on coupling thermodynamics of a ternary alloy – oxygen system (i.e. Ni-Al-Cr-O) [10] with kinetics of diffusion transport [11, 12] of atomic species in the substrate and the rate of the oxidation reactions. The output of the model predicts the composition of the oxide scale and the concentration depth profile of elements after various oxidation exposure times, by assuming parabolic oxide growth kinetics. However, it does not include diffusion of oxygen in the alloy by assuming zero solubility of oxygen in this alloy system, and therefore cannot describe internal oxidation in the alloy.

The example alloy utilised for this model is a γ-Ni-27Cr-9Al (at %) alloy oxidized at 1100ºC in air atmosphere. One of the reasons for the selection of this alloy is due to the availability of ternary interdiffusion coefficient data in Ni solid solution γ (fcc) phase of the Ni-Cr-Al system at 1100 and 1200ºC. In addition, there is no anticipated phase transformation in the alloy substrate upon surface oxidation induced composition changes as confirmed by the Ni-Cr-Al ternary phase diagram.

The predicted composition depth profiles in the substrate and the growth kinetics of oxides are compared with experimental results obtained in [9] to verify the current model.

3.2 Theoretical Development

The theoretical basis to be used in the current model can be divided into three different categories – 1) oxide thermodynamics, 2) oxidation kinetics and 3) solid-state volume diffusion.

Oxide Thermodynamics

Thermodynamic descriptions of most practical engineering ternary alloy – oxygen systems have been thoroughly studied and are widely available. The free energy changes of oxidation reactions of the Ni-Cr-Al ternary system are available in [10]. Oxidation of a single-phase alloy $M^{I}M^{II}M^{III}$ can be described by both

$$xM^{J} + \frac{y}{2}O_2 \leftrightarrow M^{J}_{x}O_{y} \quad \text{for } J = I, II, III$$

$$M^{K} + M^{J}_{x}O_{y} + \frac{1}{2}O_2 \leftrightarrow M^{K}M^{J}_{x}O_{y+1} \quad \text{for } K = \text{most noble element I and } J = II, III$$

With $\Delta G^{o}_{M^{J}_{x}O_{y}}$ and $\Delta G^{o}_{M^{K}M^{J}_{x}O_{y+1}}$, representing the standard free energy of oxide formation per mole of oxide, free energy values can be calculated from the database for a given temperature, oxygen partial pressure and activities of metallic elements. Subsequently, the oxygen partial pressure, $\Pi^{eq}_{M^{J}_{x}O_{y}}$ or $\Pi^{eq}_{M^{K}M^{J}_{x}O_{y+1}}$ (unit: atmosphere) in which oxide $M^{J}_{x}O_{y}$ or $M^{K}M^{J}_{x}O_{y+1}$ is in equilibrium with the alloy at the oxide/metal interface can be determined by

$$\Pi^{eq}_{M^{J}_{x}O_{y}} = \left(\frac{1}{a^{x}_{M}} \exp \frac{\Delta G^{0}_{M^{J}_{x}O_{y}}}{RT} \right)^{2/y}$$

$$\Pi^{eq}_{M^{K}M^{J}_{x}O_{y+1}} = \left(\frac{1}{a^{x}_{M}} \exp \frac{\Delta G^{0}_{M^{K}M^{J}_{x}O_{y+1}}}{RT} \right)^{2}$$

Where a_M are the thermodynamic activities of the constituent M at the oxide/metal interface. The activity values vary as the oxidation proceeds and can be related to the concentration of alloy constituents at the oxidation front.

In the model, activities are retrieved from a thermodynamic software (Thermo-Calc^{TM}) every time-step to enable the computation of the oxidation thermodynamics.

Oxidation Kinetics

The kinetics of oxidation can be experimentally measured and expressed in terms of an empirically measured rate expression. Although this may be the simplest way to input kinetic parameters into a thermal-kinetic oxidation model, it is also possible and more general to derive a rate expression from the Wagner's parabolic growth theory.

According to Nerst-Einstein relationship, the partial ionic conductivity σ_i, of an ionic solid (such as an oxide) can be defined as:

$$\sigma_i = \frac{c_i D_i Z_i^2 e^2}{k_B T}$$

where c_i, D_i and Z_i denotes the number of ions of type i in the oxide per unit volume, self-diffusion coefficient of element i and the valence of element i respectively. The total conductivity of an inorganic compound, such as a metal oxide, can be expressed by the sum of the conductivities of the electronic and ionic charge carriers, as follows:

$$\sigma_{total} = \sigma_{ionic} + \sigma_{electronic} = \sigma_{total}\left(t_e + t_{ion}\right)$$

where t_e and t_{ion} are the transport numbers of electrons and ions respectively. Since most oxides formed by oxidation of metals at high temperature are predominately electronic semiconductors, it is reasonable to assume $t_e \approx 1$and $t_{ion} \approx 0$ [13, 14].

The approach used in the present model is based on Wagner's parabolic growth theory [1] for high temperature oxidation of electronic conducting oxides. The parabolic oxidation rate, k_t, for an n-type oxide can be expressed as

$$k_t = \frac{3Co_o^x}{2} D_0^* \left[\left(P_{O_2}^i\right)^{-1/6} - \left(P_{O_2}^o\right)^{-1/6}\right]$$

Where Co_o^x is concentration of oxygen atoms in the regular lattice, D_0^* is the diffusion coefficient of oxygen at an oxygen partial pressure of 1atm and $P_{O_2}^i$ and $P_{O_2}^o$ are the partial pressure of oxygen at the inner and outer interface respectively. As can be seen from this expression, the driving force for the oxygen diffusion is the difference in oxygen partial pressure between the outer and inner interfaces of the oxide. k_t for a p-type oxide can be written as

$$k_t = \frac{3C_{M_M^x}}{2} D_M^* \left[\left(P_{O_2}^o\right)^{1/6} - \left(P_{O_2}^i\right)^{1/6} \right]$$

where $C_{M_M^x}$ is the concentration of metal atoms in the regular lattice, D_M^* is the diffusion coefficient of metal M at an oxygen partial pressure of 1atm.

The values of $C_{O_O^*}$ and $C_{M_M^*}$ are the concentration of metal (M) and oxygen (O) in the lattice of n-type and p-type oxide respectively. The values of the oxygen partial pressure used in these equations can be approximated by the equilibrium partial pressure values at the oxide/metal interface and the external atmosphere.

Solid-state Volume Diffusion

Isothermal solid-state volume diffusion within a ternary alloy can be modelled using the ternary diffusion equations of Fick's second law. In the ternary system, with concentration of the third component, M^{III}, being a dependent variable, the diffusion of M^I and M^{II} in the alloy is given by [15]:

$$\frac{\partial C_j}{\partial t} = \frac{\partial}{\partial X}\left(\tilde{D}_{jj} \left(\frac{\partial C_j}{\partial X} \right) \right) + \frac{\partial}{\partial X}\left(\tilde{D}_{jk} \left(\frac{\partial C_k}{\partial X} \right) \right) \qquad (j,k = M^I, M^{II})$$

where $\tilde{D}_{jj}$ and $\tilde{D}_{jk}$ are the ternary main and cross-term concentration dependent diffusion coefficients. Using the empirical relationships for the concentration dependence of interdiffusion coefficients available in [12], the above equation can be

expressed as follows:

$$\frac{\partial}{\partial X}\left(\tilde{D}_{jj}\left(\frac{\partial C_j}{\partial X}\right)\right)=\tilde{D}_{jj}\frac{\partial^2 C_j}{\partial X^2}+\left(\frac{\partial \tilde{D}_{jj}}{\partial C_j}\frac{\partial C_j}{\partial X}+\frac{\partial \tilde{D}_{jj}}{\partial C_k}\frac{\partial C_k}{\partial X}\right)\frac{\partial C_j}{\partial X} \qquad (j,k=M^I,M^{II})$$

$$\frac{\partial}{\partial X}\left(\tilde{D}_{jk}\left(\frac{\partial C_k}{\partial X}\right)\right)=\tilde{D}_{jk}\frac{\partial^2 C_k}{\partial X^2}+\left(\frac{\partial \tilde{D}_{jk}}{\partial C_j}\frac{\partial C_j}{\partial X}+\frac{\partial \tilde{D}_{jk}}{\partial C_k}\frac{\partial C_k}{\partial X}\right)\frac{\partial C_k}{\partial X} \qquad (j,k=M^I,M^{II})$$

Three initial boundary conditions were applied for this modeling application.

1). An initial boundary condition of uniform concentration distribution within the alloy is stipulated, i.e. $C_j^{t=0}=C_j^0$, where C_j^0 is the original bulk concentration of the alloy constituent j.

2). A semi-infinite boundary condition of zero diffusion flux at the end of the one-dimensional length L (Figure 3.1) is also assumed, i.e. $\left(\frac{\partial C_j}{\partial X}\right)_{X=L}=0$

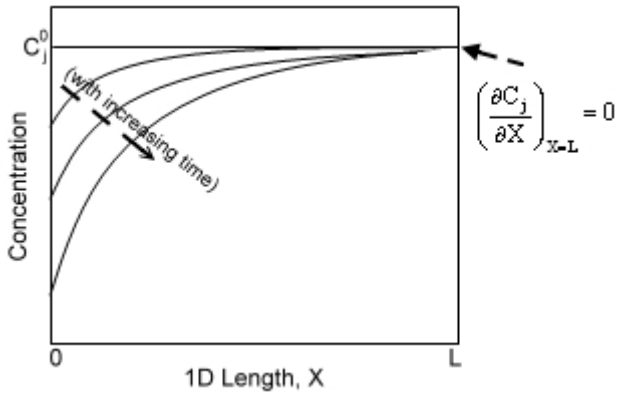

Figure 3.1 A semi-infinite boundary condition of zero diffusion flux at the end of the end of the one-dimensional length L.

3). The surface flux of diffusion at the oxidation front (oxide-metal interface), i.e. supply of reactants for oxidation, must be balanced by the oxidation kinetics set by the parabolic growth law assuming that sufficient alloy constituents are present to form the oxide of calculated thickness for a particular time step.

Thus, the mass balance can be formulated as:

$$\frac{x_j}{V_{M_x^JO_y}}\Delta\Phi_{M_x^JO_y}=\int_0^L C_j^t dx-\int_{0+\Delta\xi}^L C_j^{t+\Delta t}dx$$

where $V_{M_x^J O_y}$ is the molar volume of the oxide phase, $\Delta\Phi_{M_x^J O_y}$ is the amount (i.e. volume per unit interface area) of the oxide phases $M_x^J O_y$ formed per Δt, x_j is the stoichiometric ratio of an oxidation reaction as previously defined (i.e. the number of moles of alloy constituent M^J per mole of $M_x^J O_y$) while $\Delta\xi$ is the interfacial displacement per time step, denoted Δt.

3.3 Numerical Procedures

At beginning of the calculation, a ternary alloy with uniform concentration profiles and a given length L is represented by a grid of nodal spacing Δz to yield n number of equispaced nodes. The value of the nodal spacing Δz is taken to be the minimum grid spacing necessary to provide sufficient flux to match the oxidation kinetics. For instance, assuming that at t = 0 and based on the parabolic growth kinetics of oxides, the increment of oxide thickness can be calculated for each of the associated grown oxides (i.e. Al_2O_3, Cr_2O_3, NiO and spinels) for a given time step of Δt. In order to form oxides with the calculated thickness, the nodal spacing is calculated to be the minimum thickness capable of delivering sufficient diffusional transport of ionic alloy constituents to the oxidation front in order to provide the source of reactants for the oxidation reactions. Thus, the nodal spacing is taken to be the minimum value of the three average depths among which the three alloy constituents can diffuse from the bulk of the substrate towards the oxide/metal interface. The average root mean square diffusion distance for each alloy constituent can be obtained by the following equation:

$$z = \sqrt{2\tilde{D}_{max}\Delta t}$$

where $\tilde{D}_{max}$ is the corresponding main or cross-term interdiffusion value having the largest value.

Oxide Layer Thickness

Oxide layer thickness can be calculated based on the following equation, utilizing Wagner's parabolic growth constant, k_p, described above.

$$d_{ox} = \sqrt{k_{p'} t}$$

The thickness growth of oxides in a time step is thus, calculated by

$$\Delta d_{ox} \approx \frac{k_p}{2d} \Delta t$$

The total thickness growth of all oxides is thus,

$$\Delta d_{ox} = \sum_{J=1}^{III} \Delta d_{M_x^J O_y} + \sum_{J=1}^{III, J \neq I} \Delta d_{M^K M_x^J O_{y+1}}$$

Concentrations at all nodes

The transient 1-D solid-state volume diffusion equations described above are derived from the mass balance on an elemental control volume. Thus, the partial differential equations can be solved numerically using the Crank-Nicholson semi-implicit finite difference method [16] to yield a system of a tridiagonal matrix (i.e. a matrix has non-zero entries only on the diagonal, the super-diagonal and the sub-diagonal. Such matrices often arise in the study of numerical differential equations) which can be subsequently processed using the Gaussian elimination technique to obtain the concentrations through the entire length of an alloy. However, all formulations thus far have been for a general interior node. Surface nodes require special treatment to incorporate boundary conditions of additional flux occurring at the node 1 and L. Since the end node at L is not exposed to any other medium, there will be no external flux associated with oxidation or interdiffusion. The surface node at 1, however, is subject to oxidation as described earlier; thus, additional mass balance for node number 1 is necessary to account for the external oxidation-initiated diffusional flux.

The partial derivatives for the concentration with respect to time and position are expressed in terms of first and second order central difference approximations. The partial derivatives for concentration with respect to time are solved using forward difference to predict the concentration profile of the next time step.

Interface composition and thermodynamics of oxide formation

In order to determine the composition of the interface node at the oxide/alloy interface, it is necessary to predict the diffusion flux leaving the alloy to form oxides. As mentioned above, based on mass balance, the surface flux (i.e. supply of reactants for oxidation by diffusion) should be balanced by the oxidation kinetics; thus, it is possible to relate the parabolic growth kinetics to the diffusion flux of each of the alloy constituents. Nevertheless, a situation arises when the alloy diffusion flux of a specific constituent, calculated from its associated oxidation kinetics, is higher than the flux of the constituent available in the interface node. This essentially suggests that the amount of a reactant available is insufficient to form the oxide of calculated thickness during that particular time step; thus, the diffusional flux is, instead, limited by the amount of alloy species available near the oxidation surface for oxidation during that particular time step. Thus, the fluxes leaving and entering the interface node are determined from both the oxidation kinetics, but limited by the amount of available alloy constituents and the interdiffusion mechanism.

Oxide – Metal interface displacement

Since oxide growth contributes to metal consumption from the alloy substrate, the oxide – metal interface will be displaced an amount determined by the number of metal atoms oxidised and the change in the lattice parameter in a time step. The resulting displacement at time t with respect to the original location of interface at time 0 is illustrated in Figure 3.2 and can be determined by

$$\xi = \sum_{J=I}^{III} \frac{x_{M^J}}{V_{M_x^J O_y}} \bar{V}_{M^J} \Phi_{M_x^J O_y} + \sum_{J=II}^{III} \frac{z_{M^I}}{V_{M_z^I M_x^J O_{y+z}}} \bar{V}_{M^I} \Phi_{M_z^I M_x^J O_{y+z}}$$

$$xM^J + \frac{y}{2} O_2 = M_x^J O_y \quad \text{for } J = I, II, III$$

$$zM^K + M_x^J O_y + \frac{z}{2} O_2 = M_z^K M_x^J O_{y+z} \quad \text{for K preferentially forms a bivalent oxide, } J = II, III$$

where $V_{M_x^J O_y}$ is again, the molar volume of the oxide phase $M_x^J O_y$, Z_{M^I} is the stoichiometric ratio (i.e. number of moles of M^K per mole of $M_z^K M_x^J O_{y+z}$) of the spinel reaction and $V_{M_x^J O_y}$ is the partial molar volume of component M^J at the alloy - oxide

interface.

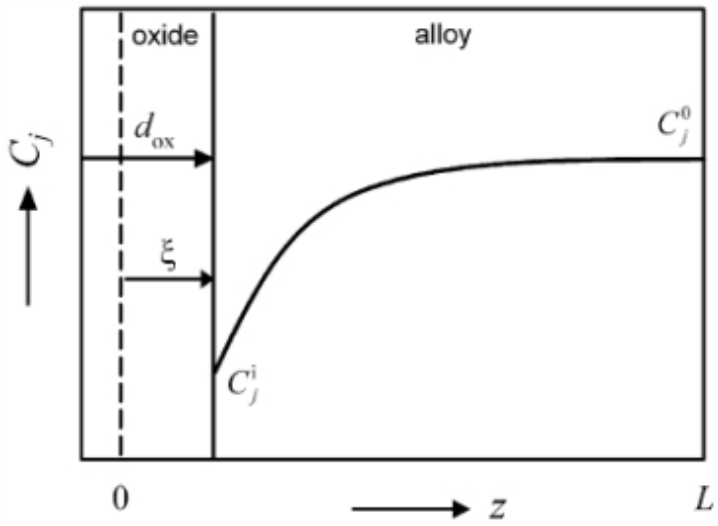

Figure 3.2 Schematic illustration of the concentration-depth profile and the oxide-metal interfacial displacement at oxidation time t. [9]

Grid adjustment

After advancing through the sequence of calculations for $t+\Delta t$, it is necessary to adjust the grid position to maintain equidistant node spacing due to the oxide – metal interface displacement. The new grid spacing Δz at time $t+\Delta t$ is thus calculated by $\Delta z^{t+\Delta t} = \left(L^t - \xi^{t+\Delta t}\right)/(n-1)$. The concentrations at the new nodes after grid adjustment are determined by linear interpolation. The interpolation errors can be minimized by reducing the time step Δt and the grid spacing Δz.

3.4 Application to a γ –NiCrAl Alloy

The finite difference model described above was applied to the oxidation of a single phase ternary alloy. The oxidation rate and the compositional change in a γ-Ni-27Cr-9Al (at %) alloy isothermally oxidised at 1373 K and ambient partial pressure of oxygen were modelled. In order to carry out the computation for the oxidation rate and the ternary main and cross-term concentration dependent diffusion coefficients, the following parameters [12, 17] and equations were used in the calculations (Table 3.1

and Table 3.2).

Table 3.1 Materials properties of oxides [17].

Oxide	Molar Volume [$cm^3\ mol^{-1}$]	Conductivity [$S\ m^{-1}$]	D^*_N [$cm^2\ s^{-1}$]	D^*_O [$cm^2\ s^{-1}$]
Al_2O_3	25.6	$1.00x10^{-4}$	$1.23x10^{-17}$	$1.29x10^{-16}$
Cr_2O_3	29.2	$1.67x10^{-4}$	$1.53x10^{-11}$	n/a
$NiAl_2O_4$	44	n/a	$1.58x10^{-13}$	
$NiCr_2O_4$	50.4	$2.50x10^{-2}$	$3.16x10^{-14}$	
NiO	11.0	1.08	$1.00x10^{-10}$	

Table 3.2 Emperically derived parameters used to obtain the concentration dependent diffusion coefficients [12]. Note: C_M is the concentration of alloy constituent M in wt%.

Parameters for Diffusion Coefficients							
$D_{AlAl}(C_{Al}, C_{Cr}) = [A110 + (A111 \times C_{Al}) + (A112 \times C_{Cr}) + (A113 \times C_{Al}^2) + (A114 \times C_{Cr}^2)] \times A115$							
$D_{AlCr}(C_{Al}, C_{Cr}) = [A120 + (A121 \times C_{Al}) + (A122 \times C_{Cr}) + (A123 \times C_{Al}^2) + (A124 \times C_{Cr}^2)] \times A125$							
$D_{CrAl}(C_{Al}, C_{Cr}) = [A210 + (A211 \times C_{Al}) + (A212 \times C_{Cr}) + (A213 \times C_{Al}^2) + (A214 \times C_{Cr}^2)] \times A215$							
$D_{CrCr}(C_{Al}, C_{Cr}) = [A220 + (A221 \times C_{Al}) + (A222 \times C_{Cr}) + (A223 \times C_{Al}^2) + (A224 \times C_{Cr}^2)] \times A225$							
A110	1.229	A120	0.0116	A210	0.0766	A220	0.783
A111	0.0731	A121	0.0923	A211	-0.0153	A221	-0.0123
A112	-0.0083	A122	-0.001	A212	0.0837	A222	0.0247
A113	0.0101	A123	0.00016	A213	0.00062	A223	0.00096
A114	0.00016	A124	0.000017	A214	-0.0015	A224	-0.00057
A115	1.00E-10	A125	1.00E-10	A215	1.00E-10	A225	1.00E-10

In order to carry out the modelling, it is necessary to calculate the equilibrium oxygen partial pressure using the thermodynamic data [10]. Figure 3.3 shows the calculated Gibbs free energies of oxidation reactions as a function of the oxygen partial pressure (in atm.) using the metal activities of the bulk alloy composition retrieved from

Thermo-Calc^{TM}. It can be seen that alumina is the most stable oxide with an equilibrium partial pressure of 2.79 x 10^{-38}, while nickel oxide is the least stable oxide with an equilibrium partial pressure of 8.99 x 10^{-11}. Nickel based spinel oxides, included in the calculation here, are thermodynamically more stable than the pure nickel oxide. Based on these equilibrium oxygen partial pressure values, the layering of different oxides can be determined, with the most stable oxide (i.e. alumina) exists directly above the metal-oxide interface and the least stable one (i.e. nickel oxide) locates on the outer most layer as illustrated in Figure 3.4. It should be indicated here that the $NiAl_2O_4$ oxide, although should be present between the $NiCr_2O_4$ and NiO layers according to the thermodynamic assessment, the formation of $NiAl_2O_4$, which relies on Ni reacting with the Al_2O_3 oxide phase, cannot take place under the current layering structure. This implies that $NiAl_2O_4$ should be absent in the current ternary alloy system or at least on the level of macroscopic consideration of the general oxide morphology and structure.

Table 3.3 Thermodynamic activity of each alloy constituent retrieved from Thermo-Calc^{TM}.

Alloy Constituent	Composition (at %)	Thermodynamic Activity
Al	9	8.24 x 10^{-8}
Cr	27	3.38 x 10^{-3}
Ni	64	7.09 x 10^{-4}

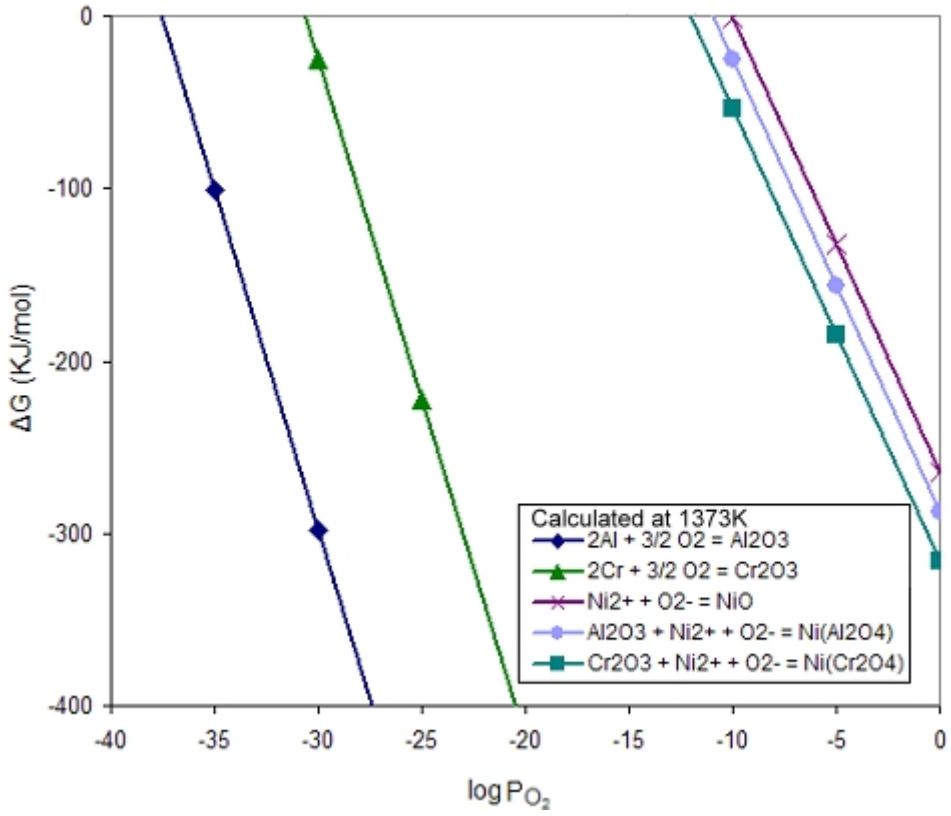

Figure 3.3 Gibbs free energies of oxidation reactions as a function of the oxygen partial pressure.

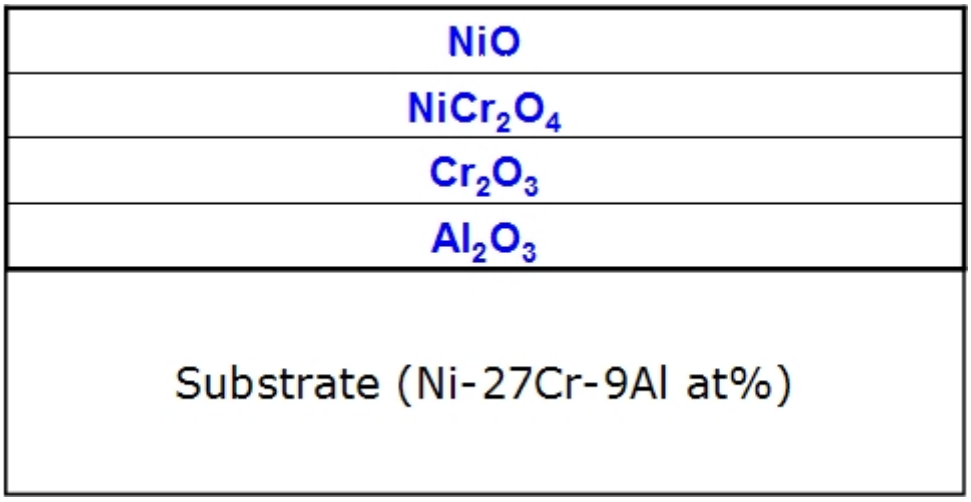

Figure 3.4 A schematic representation showing the layering of different oxides determined from the thermodynamic calculation (Figure 3.3).

Based on the thermodynamic assessment, the model uses the layering structure and assumes the presence of very thin and continuous layers of these determined stable

oxides from the beginning. The purpose of applying this assumption is to avoid modelling the initial oxide morphology and the complex competition mechanisms associated with the transition from an internal oxidation to continuous layers of oxides, since the aim of the model is to predict the composition profile changes in the alloy substrate. Oxidation kinetics are determined for each of the stable oxides using the above materials properties and the parabolic growth equations explained previously. It should be noted that due to the difficulty in determining the solubilities of cationic species in oxides (i.e. Cr^{3+} and Ni^{+} in Al_2O_3) and their transport properties, a theoretical treatment of the ionic diffusion processes in the oxide layers is not numerically established in the model. However, in order to recognise the fact that the presence of a continuous alumina layer underneath Cr_2O_3 and NiO layers inhibits the diffusion of Cr^{3+} and Ni^{+} from reaching above, the combined thickness of Al_2O_3 and Cr_2O_3 layers is used in the parabolic growth equation to calculate the growth rate of Cr_2O_3. In the case of calculating the growth rate of NiO, the total oxide thickness in the system is used. In addition, the above assumption also has its qualitative significance since in reality, the thicker the alumina layer, the less likelihood for short-circuit diffusion of Ni and Cr species in alumina to be the predominant transport mechanisms. Therefore in real systems, the growth rates of Cr_2O_3 and NiO layers are very much dependent on the thickness of the alumina scale.

By coupling this with the ternary diffusion equations, the composition profile in the alloy and the thickness of each oxide phase developed as a function of oxidation time can be modelled. Based on the calculated results, the initial rapid oxidation (i.e. transient oxidation) and the more stable quasi-equilibrium oxidation stages have been plotted along with the experimentally measured oxide thickness [9] as shown in Figure 3.5.

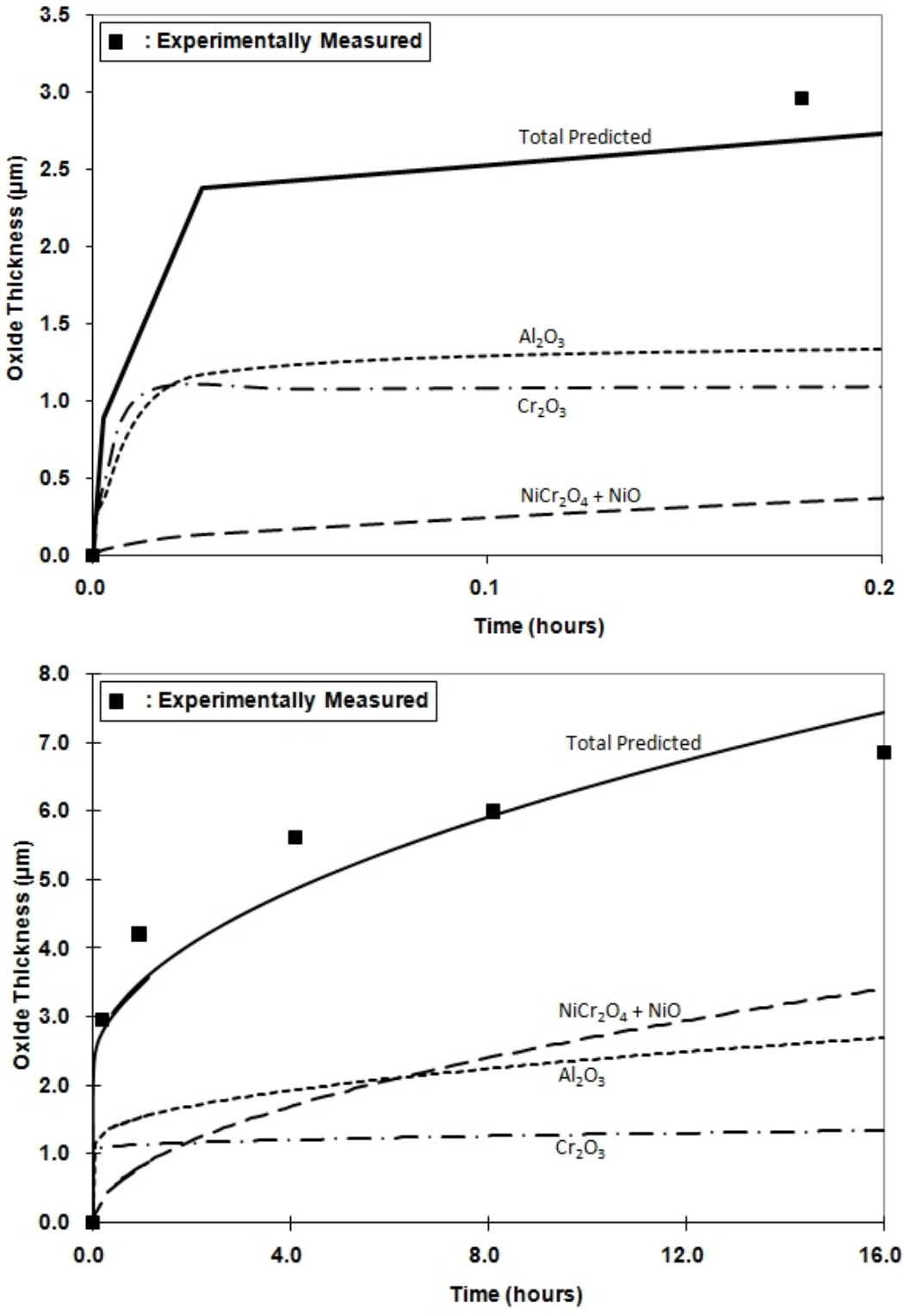

Figure 3.5 a) Top, oxidation kinetics at 1373K in the early stage b) bottom, overall oxidation kinetics at 1373K for the first 16 hours.

The cross-section microstructural morphology of the γ-Ni-27Cr-9Al (at %) ternary alloy

isothermally oxidised for 16 hours at 1373 K is also included here for comparison as shown in Figure 3.6. [18]. It can be seen here that the layering order of oxides previously proposed based on the thermodynamic assessment agrees with the actual oxide composition distribution. In particular, $NiAl_2O_4$ layer is absent in the actual oxidised specimen because $NiAl_2O_4$ is not thermodynamically stable to be formed below Cr_2O_3 in this ternary alloy system.

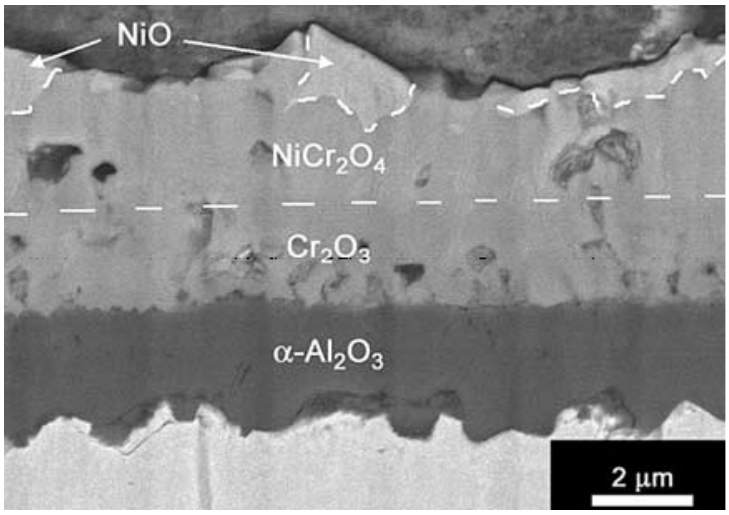

Figure 3.6 The cross-section microstructural morphology of the γ-Ni-27Cr-9Al (at %) ternary alloy isothermally oxidised for 16 hours at 1373 K [18].

The modelled results of the compositional changes in the alloy are compared against the experimental Al and Cr concentration-depth profiles of γ-Ni-27Cr-9Al measured by Auger electron spectroscopy (AES) after oxidation for 1, 4, 16, 64 hours at 1373 K and $P_{O_2} = 2x10^4$ Pa as shown in Figure 3.7 [9]. It can be seen in Figure 3.5 that the oxidation kinetics of alumina- and chromia- formation reactions are significantly higher than that of nickel oxide or spinels in the early stage of oxidation due to the enhanced thermodynamic stability of alumina over other oxides (Figure 3.3). Thus, preferential oxidation of aluminium to form alumina takes place in the initial stage of the oxidation.

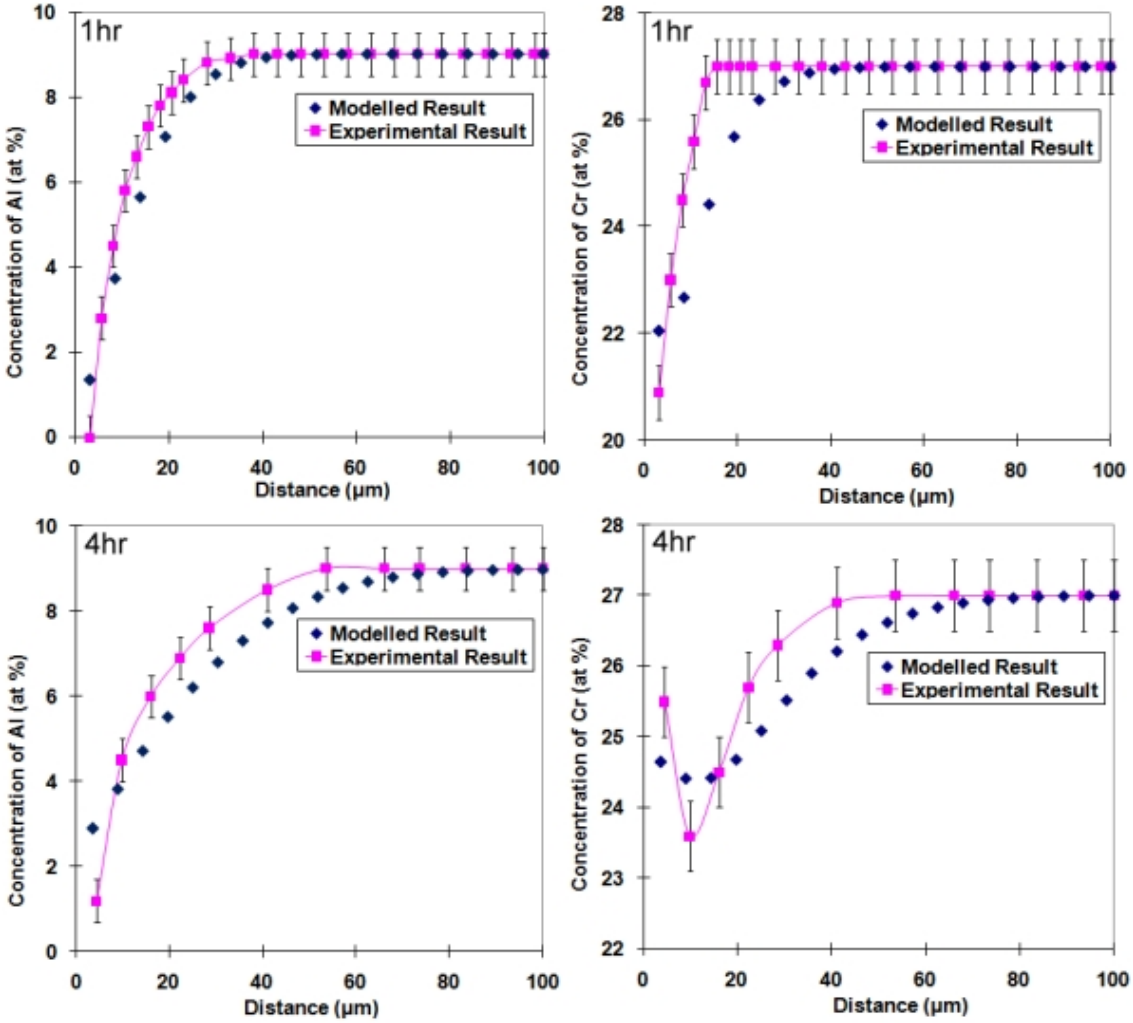

Figure 3.7 Top-left: diffusion profile of aluminium after 1 hour oxidation. Top-right: diffusion profile of chromium after 1 hour oxidation. Bottom-left: diffusion profile of aluminium after 4 hour oxidation. Bottom-right:, diffusion profile of chromium after 4 hours oxidation [9].

However, as the rate of aluminium depletion at this stage is significantly higher than the diffusion of aluminium from the bulk alloy towards the oxidation interface, the concentration of aluminium at the metal/oxide interface quickly approaches zero. The experimental concentration profiles shown in Figure 3.7 (Top-left) confirm this phenomenon. As the interfacial aluminium concentration decreases, the activities of other alloy constituents increase, thus, thermodynamically favouring formation of oxides other than alumina; thus, a drop of the chromium concentration at the interface is also observed, Figure 3.7 (Top-right).

As oxidation proceeds, its rate drops significantly, and a quasi-steady-state condition is established. During this stage, the supply of aluminium from the bulk substrate to the metal-oxide interface through the inter-diffusion process, exceeds the aluminium depletion by oxidation. As a result, there is a recovery of the aluminium concentration at the oxidation interface, (Figure 3.7 Bottom-left). The chromium concentration near the interface, on the other hand, increases quite rapidly, forming a U-shape concentration profile as shown in Figure 3.7 (Bottom-right) right which is seen experimentally. This observation cannot be explained by the interdiffusion process alone, since the inter-diffusion should give monotonic concentration profiles. Explanation of this U-shape concentration phenomenon could be related to the nickel oxide and spinel oxidation kinetics as shown in Figure 3.5, b). Since kinetics of oxidation of nickel to form nickel oxide and spinels are considerably faster than those of aluminium and chromium at the steady-state oxidation stage, it is proposed that the local depletion of nickel at the metal-oxide interface results in an increase of both aluminium and chromium concentration.

3.5 Summary and Conclusions

A coupled thermodynamic-kinetic oxidation and diffusion model capable of predicting the concentration profiles of a single-phase ternary alloy has been developed. The model relies on the simultaneous thermodynamic assessment of oxidation reactions and calculation of the oxide growth kinetics. By coupling this with the ternary diffusion equations, the composition profile in the alloy and the thickness of each oxide phase developed as a function of oxidation time can be modelled.

Application of the model to the oxidation of a Ni-27Cr-9Al (at %) ternary alloy shows that formation of a $NiAl_2O_4$ oxide layer is not possible due to the thermodynamic constraint. The model also shows that a rapid depletion in the aluminium concentration occurs at the oxide-metal interface during the initial transient oxidation stage. Moreover, it has been demonstrated that the rate of aluminium supply from the bulk alloy towards

the oxide reaction interface by inter-diffusion is considerably slower than the rate of aluminium consumption to form oxide during the initial transient oxidation stage. This is in fact, responsible for the aluminium depletion near the interface and its local concentration being essentially very close to zero. When such situation arises, the oxygen partial pressure in the oxide metal interface tends to increase and consequently, favouring the formation of other less stable oxides such as chromia and nickel based oxides.

In addition, since kinetics of oxidation of nickel to form nickel oxide and spinels are considerably faster than those of the oxidation of aluminium and chromium at the steady-state oxidation stage, the local concentration drop of nickel at the metal-oxide interface results in a local increase of both aluminium and chromium concentrations near this interface.

References for Chapter 3

[1] C. Wagner, “Theoretical analysis of the diffusion progress determining the oxidation rate of alloys,” Journal of The Electrochemical Society, Volume 99, 1952, Pages 369-380

[2] B.D. Bastow, D.P. Whittle, G.C. Wood, “Alloy depletion profiles resulting from the preferential removal of the less noble metal during alloy oxidation,” Oxidation of Metals, Volume 12, 1978, Pages 413-438

[3] G. Wang, B. Gleeson, and D.L. Douglass, “An extension of Wagner’s analysis of competing scale formation,” Oxidation of Metals, Volume 35, 1991, Pages 317-332

[4] D.P. Whittle, D.J. Evans, D.B. Scully and G.C. Wood, “Compositional changes in the underlying alloy during the protective oxidation of alloys,” Acta Materialia, Volume 15, 1967, Pages 1421-1430

[5] G.L. Wulf, M.B. McGirr, and G.R. Wallwork, “Theoretical analysis of alloy oxidation with reference to Fe-Cr alloys,” Corrosion Science, Volume 9, 1969, Pages 739-754

[6] G. Wahl, “Coating composition and the formation of protective oxide layers at high temperatures,” Thin Solid Films, Volume 107, 1983, Pages 417-426

[7] P. Carter, B. Gleeson, and D.J. Young, “Calculation of precipitate dissolution zone kinetics in oxidising binary two-phase alloys,” Acta Materialia, Volume 44, 1996, Pages 4033-4038

[8] J.A. Nesbitt, “COSIM – A finite-difference computer model to predict ternary concentration profiles associated with oxidation and interdiffusion of overlay-coated substrates,” NASA Glenn Research Center - Technical Report (2000) <http://gltrs.grc.nasa.gov/>

[9] T.J. Nijdam, L.P.H. Jeurgens and W.G. Sloof, “Modelling the thermal oxidation of ternary alloys – compositional changes in the alloy and the development of oxide phases,” Acta Materialia, Volume 51, 2003, Pages 5295-5307

[10] P. Saltykov, O. Fabrichnaya, J. Golczewski, F. Aldinger, “Thermodynamic modeling of oxidation of Al-Cr-Ni alloys,” Journal of Alloys and Compounds, Volume 381, 2004, Pages 99-113

[11] N. Matan, H.M.A. Winand, P. Carter, M. Karunaratne, P.D. Bogdanoff and R.C.

Reed, “A coupled thermodynamic/kinetic model for diffusional processes in superalloys,” Acta Materialia, Volume 46, 1998, Pages 4587-4600

[12] J.A. Nesbitt and R.W. Heckel, “Interdiffusion in Ni-rich, Ni-Cr-Al alloys at 1100 and 1200ºC: part II. diffusion coefficients and predicted concentration profiles,” Metallurgical and Materials Transactions A, Volume 18A, 1987, Pages 2075-2086

[13] A. Atkinson, “Transport processes during the growth of oxide films at elevated temperature,” Reviews of Modern Physics, Volume 57, 1985, Pages 437-470

[14] A.S. Khanna, “Introduction to High Temperature Oxidation and Corrosion,” (2002) ASM International

[15] J.S. Kirkraldy and D.J. Young, “Diffusion in the condensed state,” London: The institute of Metals, 1987

[16] W.F. Ames, “Numerical methods for partial differential equations.” 3rd ed. Boston: Academic Press, 1992

[17] P. Kofstad, “High Temperature Corrosion.” (London: Elsevier Applied Science Publishing, 1988), p.p. 268-274

[18] T.J. Nijdam, L.P.H. Jeurgens, and W.G. Sloof, “Promoting exclusive α-Al2O3 growth upon high-temperature oxidation of NiCrAl alloys: experiment versus model predictions,” Acta Materialia, Volume 53, 2005, Pages 1643-1653

Chapter 4

Experimental Details

4.1 Initial Preparation of Specimens

Fully heat-treated (solution and primary-aged) single crystal alloys of SRR99, CMSX-4, TMS-82+, PWA-1484 and TMS-138A processed using conventional investment casting methods into cylindrical rods (10 mm in diameter), with the long axis of each aligned close (±5°) to the <001> axis, were used as substrate materials for this research. The chemical compositions of the alloys considered are given in Table 4.1 (major elemental additions) and Table 4.2 (trace elements). These chemical analyses were conducted by Cannon Muskegon Corporation using LECO^{TM} Carbon & Sulfur Determinator, X-ray fluorescence (XRF), and inductively coupled plasma mass spectrometry (ICPMS) methods, to industry leading levels of precision (i.e. ppm levels). These alloy rods were cut to disc-shape (10 mm diameter and 4 mm thickness) and spot welded onto rectangular Nimonic sticks. The surfaces of the welded specimens were grit-blasted with 200-mesh Al_2O_3 grit before the deposition of coatings. Three different bond coats, a high temperature low activity Pt-Al (HT Pt-Al) -, a low temperature high activity Pt-Al (LT Pt-Al) - and a Pt diffusion - bond coat, were subsequently deposited onto the flat surfaces of the button-shaped discs.

Table 4.1 Nominal chemical composition, wt%, of the nickel-based superalloys considered. (Note: - means that the element is not included in the chemical analysis)

Element	Co	Cr	Mo	W	Al	Ti	Ta	Hf	Re	Ru	C	Ni
SRR99	5.0	8.0	-	9.5	5.5	2.2	2.8	-	-	-	0.011	Bal.
TMS-82+	7.8	4.9	1.9	8.7	5.3	0.5	6.0	0.1	2.4	-	-	Bal.
PWA1484	10.0	5.0	2.0	6.0	5.6	-	8.7	0.1	3.0	-	-	Bal.
CMSX-4	9.6	6.5	0.6	6.4	5.6	1.0	6.5	0.1	3.0	-	-	Bal.
TMS-138A	5.8	3.2	2.8	5.6	5.7	-	5.6	0.1	5.8	3.6	-	Bal.

Table 4.2 Levels of trace elements in the superalloy substrates examined, as determined by XRF, LECO and ICPMS methods (in ppm by weight).

Element	S	B	O	N	P	Zr
SRR99	2	2	2	4	2	4
TMS-82+	2	1	2	2	11	13
PWA1484	3	2	2	1	6	19
CMSX-4	2	8	2	2	4	7
TMS-138A	2	3	2	1	18	3

The HT Pt-Al and the LT Pt-Al bond coat specimens were prepared by first electrodepositing a thin layer of platinum of 5 and 7 μm respectively, followed by a vacuum heat treatment applied at 1100°C for 1 hour. Next, 5 hr vapour phase - and 20 hr pack- aluminisation processes were applied at 1080°C and 870°C respectively. Both the vapour phase and pack processes involve the generation of vapours containing aluminium, which are usually halides due to their high vapour pressures. The vapours flow and react with the substrate surface upon contact forming the aluminide coating. In the aluminisation process, specimens are either embedded in a pack mix (i.e. LT Pt-Al) or hanged in vapour-filled environment (i.e. HT Pt-Al) in a heated chamber.

The Pt-diffusion bond coat specimen was first electroplated with a 10 μm layer of platinum and then a vacuum heat treatment at 1150°C for 1 hour was subsequently carried out. No aluminisation process was applied in this case. All specimens were further heat-treated for 1 hour at 1100°C in argon atmosphere and a ZrO_2 /7wt% Y_2O_3

(YSZ) top coat 175μm in thickness was then deposited by EB-PVD. A further vacuum heat treatment (1100°C, 1 hr) and aging (870°C, 16 hrs) were applied to all specimens before testing.

4.2 Conditions for Thermal Cycling Test

The TBC coated disc-shape specimens were then subjected to cyclic oxidation testing in a purpose-built rig (See Figure 4.1). Each thermal cycle involved 1 hour at a furnace temperature of 1135°C (approximately 10 mins to reach the peak temperature); after which, the specimens were removed automatically from the rig and fan-cooled by laboratory air for 1 hour. Five individual specimens of each TBC system were cycled to failure to determine the average TBC spallation lifetime, to evaluate the scatter in the experimental results. In addition to the cycled to failure test, additional specimens were removed from the rig at specific intervals for the luminescence measurements (see below) and then returned for further thermal cycling. Some specimens were withdrawn from cycling, mounted in epoxy, cut through by an abrasive alumina blade to reveal the cross section and polished to mirror-finish for microstructural characterisation. An additional 3 coated disc-shape specimens were isothermally heated at 1135°C in the same rig for 150 hours.

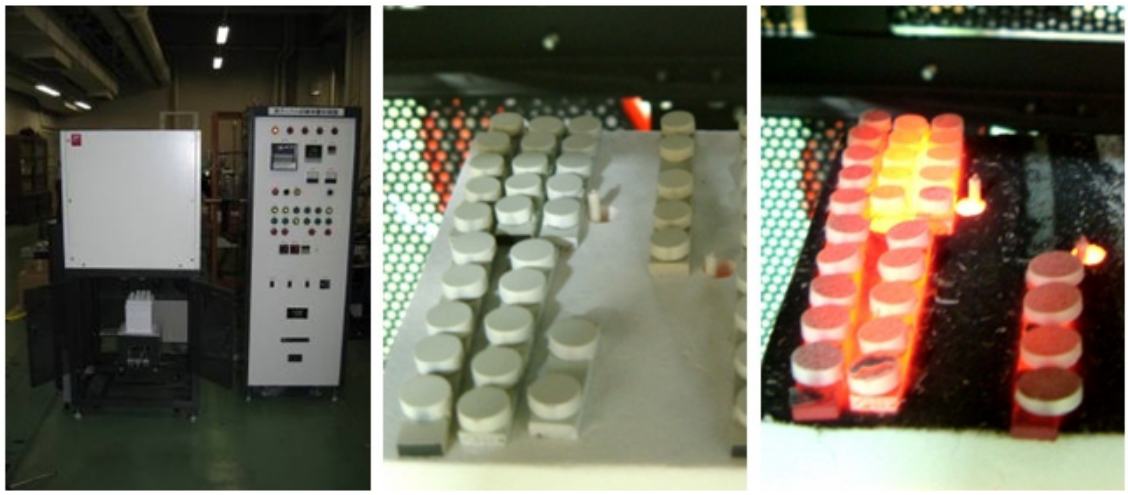

Figure 4.1 Pictures showing the use of the thermal cycling furnace (left), the placement of specimens on the sample stage (centre) and the heating/cooling conditions (right).

Microstructure characterisation was carried out in a field emission gun scanning electron microscope (FEG-SEM) equipped with EDX using the secondary electron detection mode at a working distance of 15mm and an accelerating voltage of 20kV. For high resolution quantitative elemental analysis, a prototype field emission electron probe microprobe analyser (FE-EPMA) was used for analysis by wavelength dispersive X-ray spectrometry (WDS). A probe current of 5.0 x 10^{-8} A was applied within a probe diameter of about 0.25 μm, at an accelerating voltage of 20 kV.

Residual stress in the thermally grown aluminium oxide (TGO) can be measured by piezospectroscopy, which acquiring Cr^{3+} luminescence spectra [1-3] emitted from α-Al_2O_3 as a result of excitation by a laser beam. The details for luminescence experiments are given in [4]. Luminescence spectra were acquired using a Renishaw Raman optical microprobe (model 2000) fitted with a motorised mapping stage. The luminescence from the TGO is due to the photo stimulation of trace Cr^{3+} impurities present within the alumina. The spectrum has a featured intense doublet, the R1 and R2 lines, where R2 represents the peak with the higher wave number and lower integral peak area [5]. The characteristic R line luminescence is a phenomenon resulted by the non phonon radiative decay from the Cr^{3+} first excited state to the ground state within the d orbital [6]. The laser source was a green Ar+ laser with a wavelength of 514.5 nm, which is focused on the specimen surface through an objective lens. The focused spot size can be adjusted by using different objective lens, with a minimum spot size of approximately 2 μm. However, upon incident on the specimen surface, the laser beam scatters within the YSZ top coat and consequently, results in an effective spot size at the TGO of approximately 20 μm [7, 8]. The light scattered back from the specimen was then collected by the objective lens, dispersed by a 1800 lines/mm grating and then received by a CCD detector.

An air conditioning unit was used to maintain a stable room temperature at 22±0.3°C. An acquisition time of one second was used for each spectrum. Measurements (121 per specimen) were taken on a square grid of 200 × 200 μm with a pitch of 20 μm located in

the centre of the flat face of the disk specimen. Before and after each measurement, the spectrometer was calibrated by taking a spectrum from a strain-free single crystal sapphire sample. The residual stress in the TGO was estimated from the R2 peak shift assuming a planar equi biaxial stress: $\sigma(GPa)=5.07\Delta\nu$ (cm^{-1}). Transition phases of alumina (eg., θ-Al_2O_3) produce luminescence lines at 14260 cm^{-1}, 14330cm^{-1}, 14546 cm^{-1} and 14626 cm^{-1}, which are distinguishable from the R1 and R2 lines of α-Al_2O_3 [19]. However, no significant transition phases were seen in the TGO for all the cases in this study. Five individual specimens of each TBC system were used for the above analyses to ensure consistency of the experimental results.

4.3 Characterisation of Coating Cross-Sections – As Received Condition

Scanning electron micrographs illustrating the microstructures of the three coatings in the as-received condition are given in Figure 4.2. In all cases, the YSZ top coat layer had almost the same thickness. Discernible differences can be seen between the microstructures and the thicknesses of the bond coats. Pt-Al bond coat systems produce a single phase β-(Pt,Ni)Al microstructure (i.e. NiAl with Pt in solid solution) next to the YSZ. Below the grit-line (residual Al_2O_3 particles remaining from the grit-blasting process prior to Pt plating) is the inner multi-phase layer of the coating consisting of precipitates rich in refractory metals (Ta, W, Mo) in the β phase matrix. The Pt-diffusion bond coat consists of a two phase γ and γ' microstructure both above and below the grit-line; the β-NiAl phase is completely absent since the aluminisation step was absent. Al and Pt EDX concentration line-profiles of these coatings are shown in Figure 4.3. As can be seen, the aluminisation process significantly increases both the Al concentration and the bond coat thickness in the Pt-Al systems. The main difference between the LT Pt-Al and HT Pt-Al bond coats is in the Pt profile. The LT Pt-Al has a higher Pt concentration within the first 20 μm, whereas the HT Pt-Al bond coat has higher Pt concentration at 30-60 μm. The Pt-diffusion bond coat, on the other hand, inherits the original Al content from the superalloy substrate and has higher Pt concentration than the Pt-Al systems due to the thicker electroplated Pt prior to the diffusion-heat treatment

process. In all cases, the post-processing heat treatment resulted in the formation of a thin thermally-grown oxide (TGO) layer, which shows as a thin dark line between the bond coat and YSZ, even before any thermal cycling had taken place.

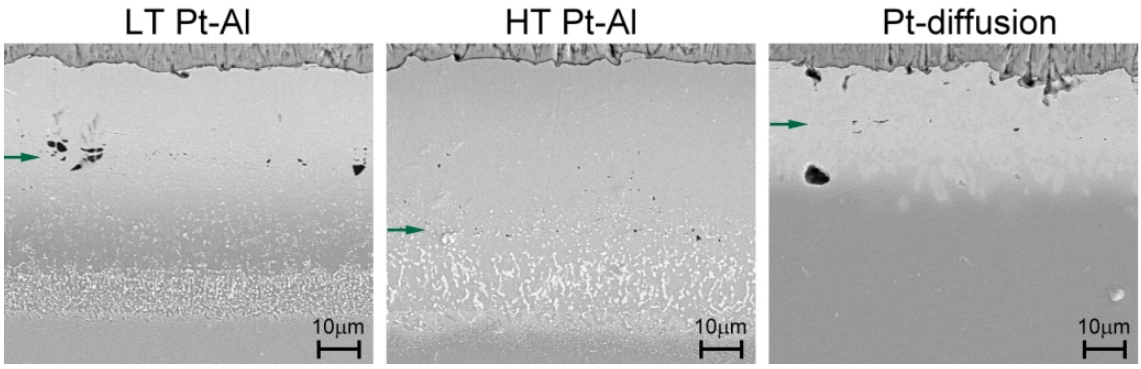

Figure 4.2 The cross-section microstructures of the bond coats (LT Pt-Al, HT Pt-Al, and Pt-diffusion) in the as-received coatings on CMSX-4. (Note: grit-lines are marked by arrows)

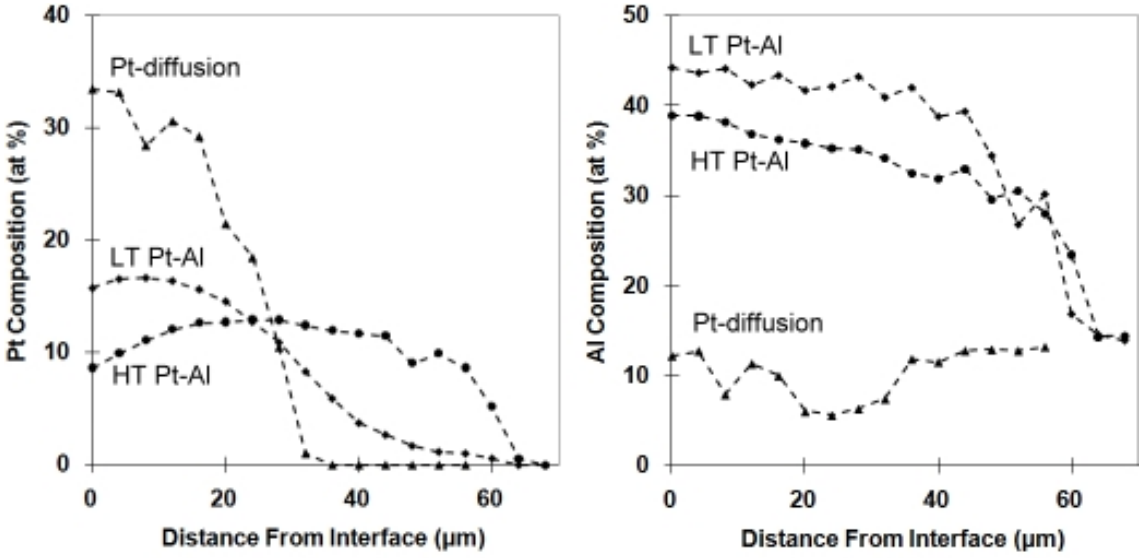

Figure 4.3 EDX concentration line-profile of Pt and Al in the as-received bond coats.

The microstructures of Pt-diffusion coatings on superalloy substrates are also shown in Figure 4.4. In all cases, the TBC top coats were prepared to similar thickness. It can be seen that the only differences are between the microstructures and the thicknesses of the bond coats. Pt-Al bond coat systems produce an outer layer with a single phase

microstructure of β-NiAl with Pt in solid solution (i.e. (Pt, Ni)Al). Below the grit-line of residual Al_2O_3 particles from the grit blasting process is the inner multi-phase layer of the coating consisting of precipitates (bright features) rich in refractory metals (Ta, W, Mo) in the β phase matrix. The Pt-diffusion bond coat consists of a two phase γ and γ' microstructure both above and below the grit-line; the β-NiAl phase is completely absent since the aluminisation process was not performed. Al and Pt EDX concentration line-profiles of these coatings are shown in Figure 4.3. In all cases, the post-processing heat treatment has resulted in the formation of a very thin thermally-grown oxide (TGO) layer even prior to any thermal cycling taking place.

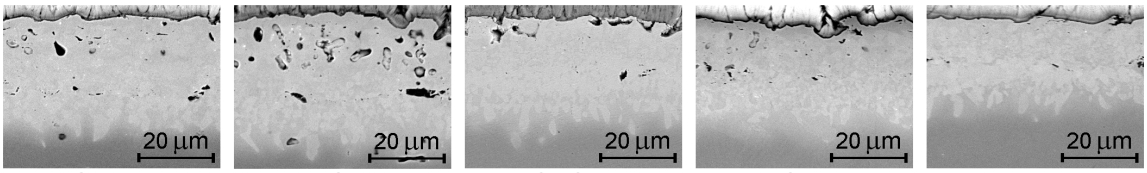

Figure 4.4 The microstructures of Pt-diffusion coatings on the superalloy substrates in the as-received condition.

References for Chapter 4

1. Q. Ma and D.R. Clarke, "Stress measurement in single-crystal and polycrystalline ceramics using their optical fluorescence," Journal of American Ceramic Society, Volume 76, 1993, Pages 1433-1440

2. D.M. Lipkin, and D.R. Clarke, "Measurement of the stress in oxide scales formed by oxidation of alumina-forming alloys," Oxidation of Metals, Volume 45, 1996, Pages 267-280

3. A. Selcuk and A. Atkinson, "Analysis of the Cr^{3+} luminescence spectra from thermally grown oxide in thermal barrier coatings," Materials Science and Engineering A, Volume 335, 2002, Pages 147-156.

4. X. Wang and A. Atkinson, "Piezo-spectroscopic mapping of the thermally grown oxide in thermal barrier coatings," Materials Science and Engineering A, Volume 465, 2007, Pages 49-58.

5. D.R. Clarke, R.J. Christensen, and V. Tolpygo, "The evolution of oxidation stresses in zirconia thermal barrier coated superalloy leading to spalling failure," Surface and Coatings Technology, Volume 94-5, 1997, Pages 89-93

6. J. He and D.R. Clarke, "Polarization dependence of the Cr^{3+} R-line fluorescence from sapphire and its application to crystal orientation and piezospectroscopic measurement," Journal of the American Ceramic Society, Volume 80, 1997, Pages 69-78

7. J.A. Nychka, D.R. Clarke, and S. Sridharan, "NDE assessment of TBCs: an interim report of a photostimulated luminescence 'round-robin' test," International Conference On Metallurgical Coatings And Thin Films (ICMCTF), 2002. San Diego: American Vacuum Society.

8. R.J. Christensen, D.M. Lipkin, D.R. Clarke and K. Murphy, "Nondestructive evaluation of the oxidation stresses through thermal barrier coatings using Cr^{3+} piezospectroscopy," Applied Physics Letters, Volume 69, 1996, Pages 3754-3756.

Chapter 5

An Investigation of the Compatibility of Nickel-based Single Crystal Superalloys with Thermal Barrier Coating Systems

---

5.1 Introduction

Single crystal (SC) superalloys [1] have traditionally been designed with the priority to optimise the creep, fatigue, oxidation and corrosion-resistant properties. However, as the demand for better fuel efficient turbine systems continues, it is required that the substrate materials must now be coated with thermal barrier coatings (TBCs) [2,3] to enhance the high temperature capability of critical turbine components such as turbine blades and guide vanes. Yet, it is known that TBC coated nickel-base superalloys are prone to spallation [4]; for this reason, several bond coat technologies have been developed as a means to enhance the mutual compatibility of the two by improving the oxidation resistance of the coated specimens.

Unfortunately, little work [5,6] has been reported to elucidate the compatibility issues of superalloys with the TBCs. More importantly, the influence of the substrate composition on the TBC spallation life is not well understood. This is despite much progress which has been made to determine the micromechanics of the failure mode of TBCs [7,8]. In particular, the approach in modeling TBC failure [9-13] generally relies on the treatment of the oxidation-induced stresses that drive TBC spallation despite the fact that it might reasonably be assumed that the TBC life and the modes of failure (i.e. location of interfacial failure) are also influenced significantly by the inherited chemistry of the

underlying superalloys.

In this study, the compatibility of a number of nickel-based single crystal superalloys with thermal barrier coating systems has been investigated. It has been demonstrated conclusively that the compositions of these alloys play an important role in determining TBC spallation resistance.

5.2 Results

5.2.1 Thermal Cyclic Oxidation Testing

Based on the results of the thermal cycling experiment, it was found that coating life varied significantly with the composition of the superalloy substrate as illustrated in Figure 5.1 with the error bars indicate ± one standard deviation in the lifetimes of each set of five specimens. For instance, TBC coated PWA1484 exhibited spallation lifetimes at least three times superior to those of first generation superalloy SRR99 regardless of the type of bond coat being applied, suggesting that strong chemical effects were inherited from the substrate. In addition, the spallation resistance of TBC coated 4th generation TMS-138A behaved significantly better than that of SRR99 and comparable to that the second generation superalloy CMSX-4, suggesting that no detrimental effect is inherited from ruthenium addition to the substrate, at least for the Pt-diffusion coating. It should be noted here that the thermal exposure of PWA-1484 specimens coated with Pt-diffusion bond coat was interrupted at the 1000th cycle as the purpose of demonstrating TBC spallation resistance had been fulfilled. These findings confirm a dependence of the TBC spallation life on the superalloy composition, and can be explained only by the different degradation mechanisms taking place in the bond coat or near the TGO interfaces (since the bond coat and the ceramic top coat were prepared in the same way on all different substrates).

In terms of the bond coat technology, it was demonstrated in general that the type of

bond coat being applied had less influence on the TBC spallation life than did the substrate. It was shown as well that platinum-diffusion bond coats outperformed both platinum aluminide systems.

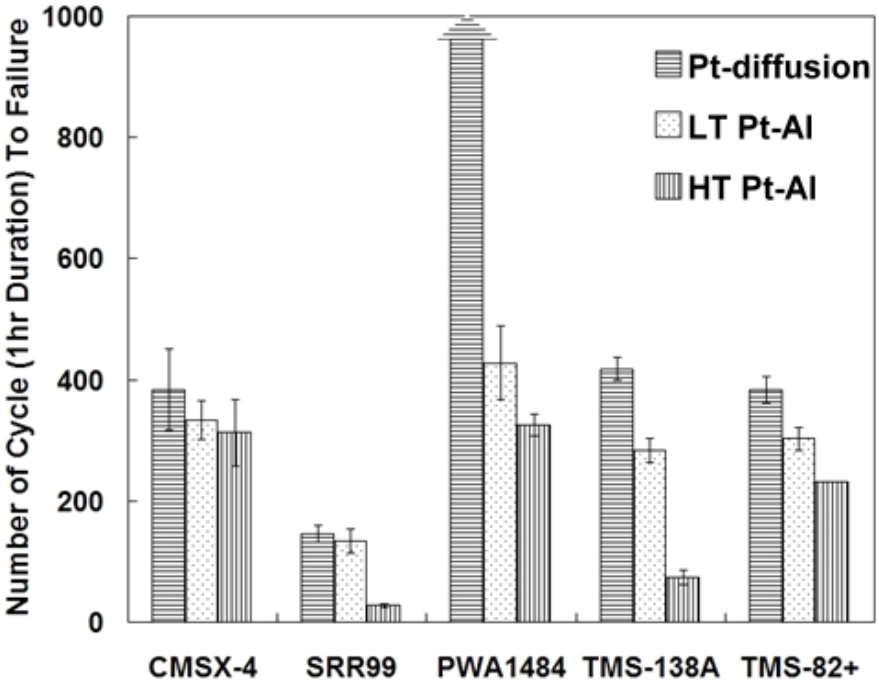

Figure 5.1 TBC spallation life for cyclic oxidation testing (1 hour thermal cycling to peak temperature) of TBC coated superalloys. The error bars indicate ± one standard deviation in the lifetimes of each set of five specimens.

5.2.2 Mechanism of TBC Failure

As previously demonstrated, the composition of the superalloy substrates has a larger influence on the TBC spallation life than that of the bond coat materials. For this reason, attention is focused in this section on how the substrate affects the mechanism of TBC failure, at a fixed TBC preparation condition. Pt-diffuson bond coat was chosen for this investigation as it showed the largest substrate effect on the coating spallation life.

SEM images of the fracture interface for each of the five substrates are shown in Figure 5.2. It was found that decohesion occurred at a position which depended on the substrate composition. In particular, it was observed that specimens with shorter TBC

spallation life tended to fail at the TGO / bond coat interface; while more spallation-resistant coatings failed within the TGO. In addition, by importing higher magnification files of these SEM images into imaging software, the thickness of the TGO at failure for each of the specimens could be quantised by making boundary selections (i.e. defining the top and bottom TGO interfaces) and calculated with reference to the scale bar of these images. These TGO thicknesses were plotted along with the TBC life for comparison as illustrated in Figure 5.3.

Based on these results, it can be seen that the TGO thickness at failure in TMS-138A is considerably thicker than that of the TMS-82+, even though TBC coated TMS-138A offered slightly longer TBC spallation life than TMS-82+. Moreover, despite the fact that the TBC lifetimes of CMSX-4, TMS-138A and TMS-82+ were within a few cycles to each other, their TGO growth kinetics are very different. Thus, it seems that there is little correlation between the oxide growth kinetics and the TBC spallation life.

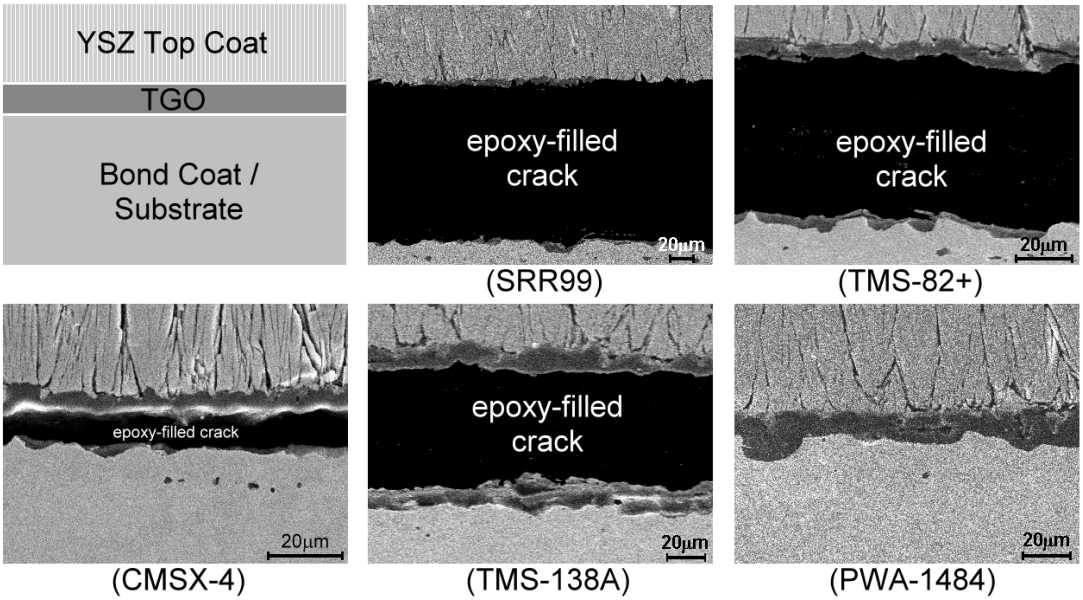

Figure 5.2 SEM micrographs illustrating the location of interfacial spallation failure of TBC (Pt-diffusion bond coat) coated superalloys.

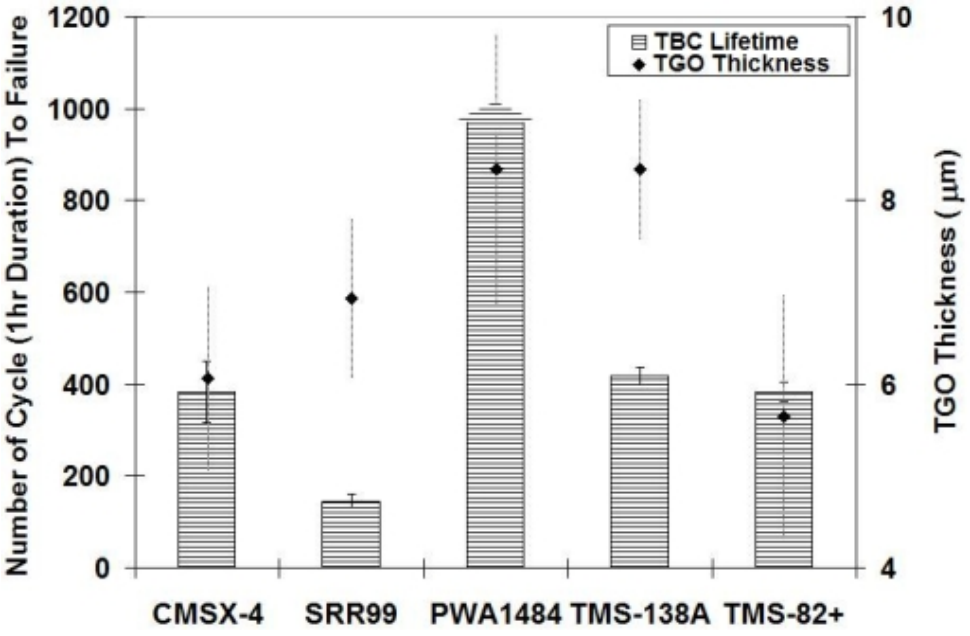

Figure 5.3 TBC spallation life vs the thickness of TGO upon failure; illustrating no clear correlation between the two.

5.2.3 High Resolution Analysis and Mapping by EPMA/WDX

Elemental compositions of the TGO layers on the three bond coats were characterized using WDS analysis, see Table 5.1. The results are quoted only for specimens with TGO thickness greater than the spatial resolution of the FE-EPMA/WDX technique (~ 1μm). Chemical mapping of the bond coat near the TGO interfaces was also carried out to determine the elemental chemical distributions on specimens after 100-cycles thermal exposure as shown in Figures 5.4 – 5.8. The results suggest that for all specimens, the oxide layers are primarily of Al_2O_3. However, it has also been observed for some specimens that either islands or continuous layers of Ni, Cr and, or Co –rich oxides are present above the primarily Al_2O_3 layer. For example, CMSX-4, TMS82+, TMS-138A and PWA1484 all contain islands which are rich in Cr; while TMS82+, TMS138A and PWA1484 further contain islands rich in Ni. In addition, the presence of Co rich regions has also been noticed on TMS-82+ and TMS-138A. For SRR99 specimens, fairly continuous Ni, Cr and Co –rich oxides are present. However, it should be recognised that the amount of spinel phases in the TGO is very small in any of the TBC coated

systems; the TGO thickness upon failure varies between different alloys and is essentially a measure of the amount of alumina.

At the TGO / bond coat interface, an enriched layer (i.e. a bright line) of Ni, Cr, Al and Ti was observed in the SRR99 specimen. TMS-82+ and CMSX-4 also have enriched layers of Ni and Cr near the interface. Both TMS-138A and PWA1484, in contrast, had no noticeable enrichment of alloying constituents.

Table 5.1 Elemental compositions (wt%) of the TGO layers measured by WDS FE-EPMA analysis.

Element	Pt	Zr	Y	Co	Re	Ta	Mo	Al	Ni	Ru	W	Ti	Cr	O
SRR99	0.3	0.8	0.1	0.1	-	0.0	-	51.6	0.5	-	0.1	0.0	0.2	46.2
TMS-82+	0.5	0.7	0.1	0.1	0.1	0.1	0.0	51.6	0.6	-	0.1	0.0	0.1	45.9
PWA1484	0.5	0.9	0.1	0.1	0.1	0.1	0.0	51.6	0.7	-	0.1	-	0.1	45.6
CMSX-4	0.3	0.9	0.1	0.1	0.1	0.1	0.0	48.8	0.7	-	0.0	0.0	0.1	48.7
TMS-138A	0.4	0.8	0.1	0.1	0.1	0.0	0.0	51.7	0.6	0.0	0.1	-	0.0	46.0

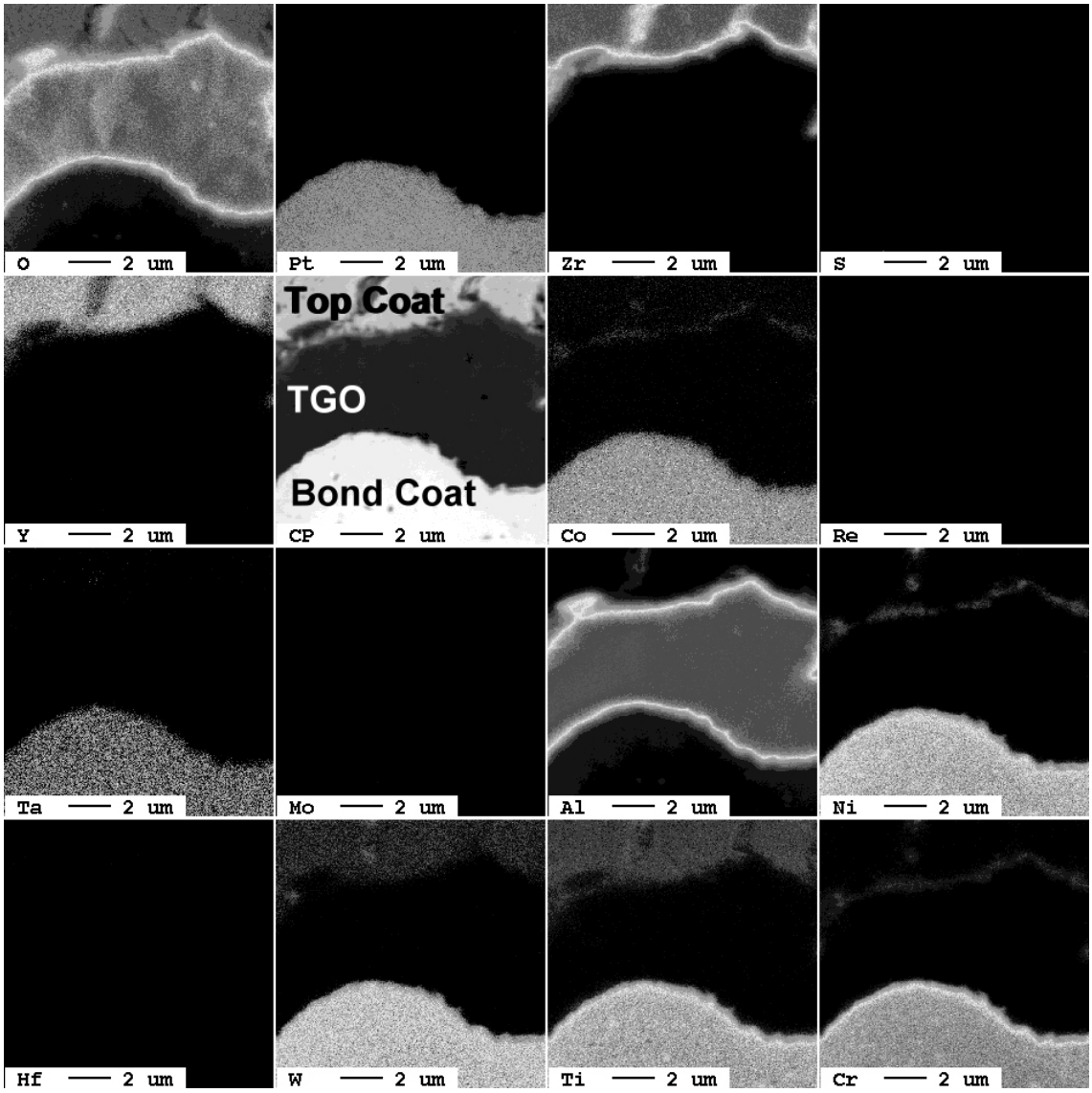

Figure 5.4 Quantitative WDX maps of the TBC coated SRR99 – Pt-diffusion system following 100 cycle exposure at 1135°C.

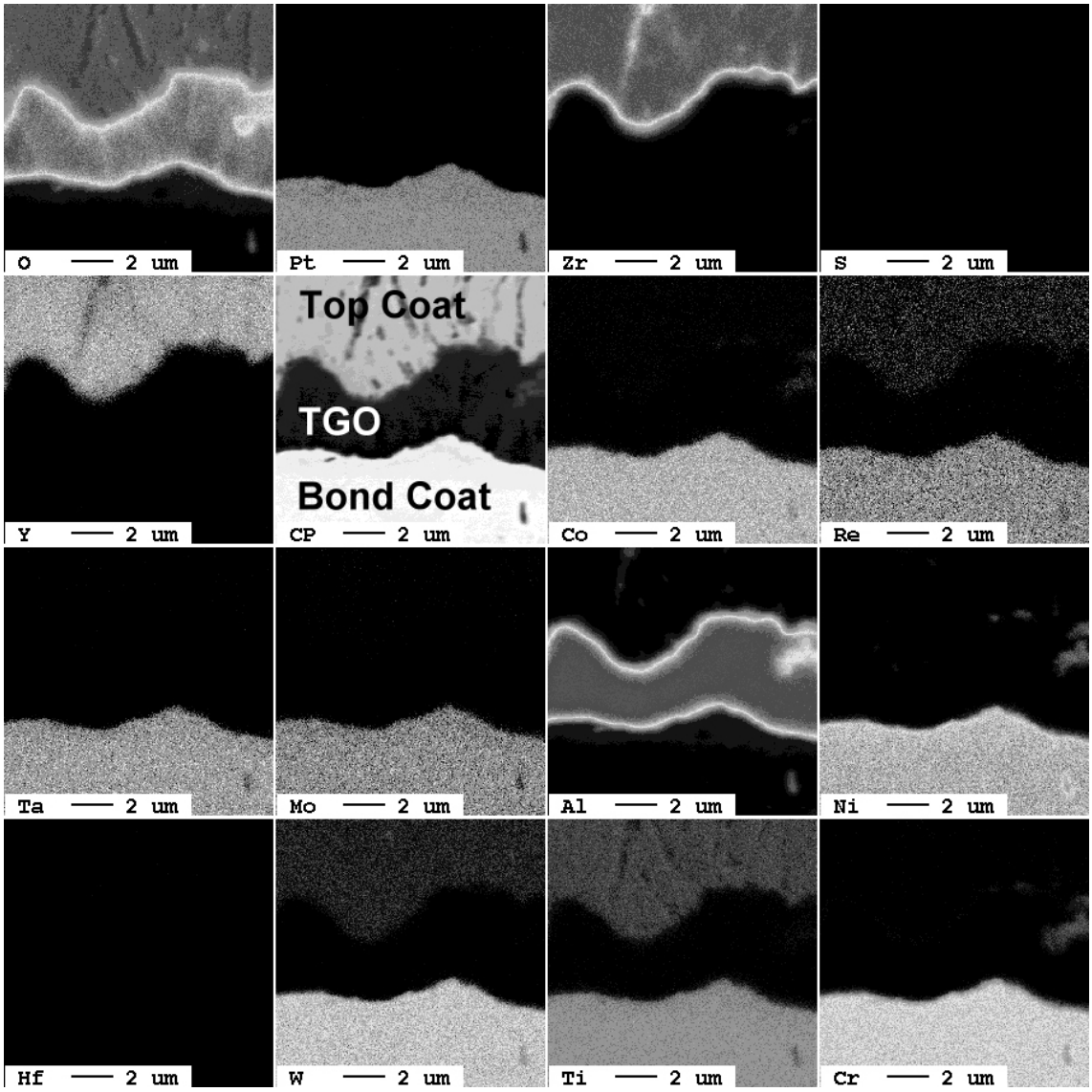

Figure 5.5 Quantitative WDX maps of the TBC coated TMS-82+ - Pt-diffusion system following 100 cycle exposure at 1135°C.

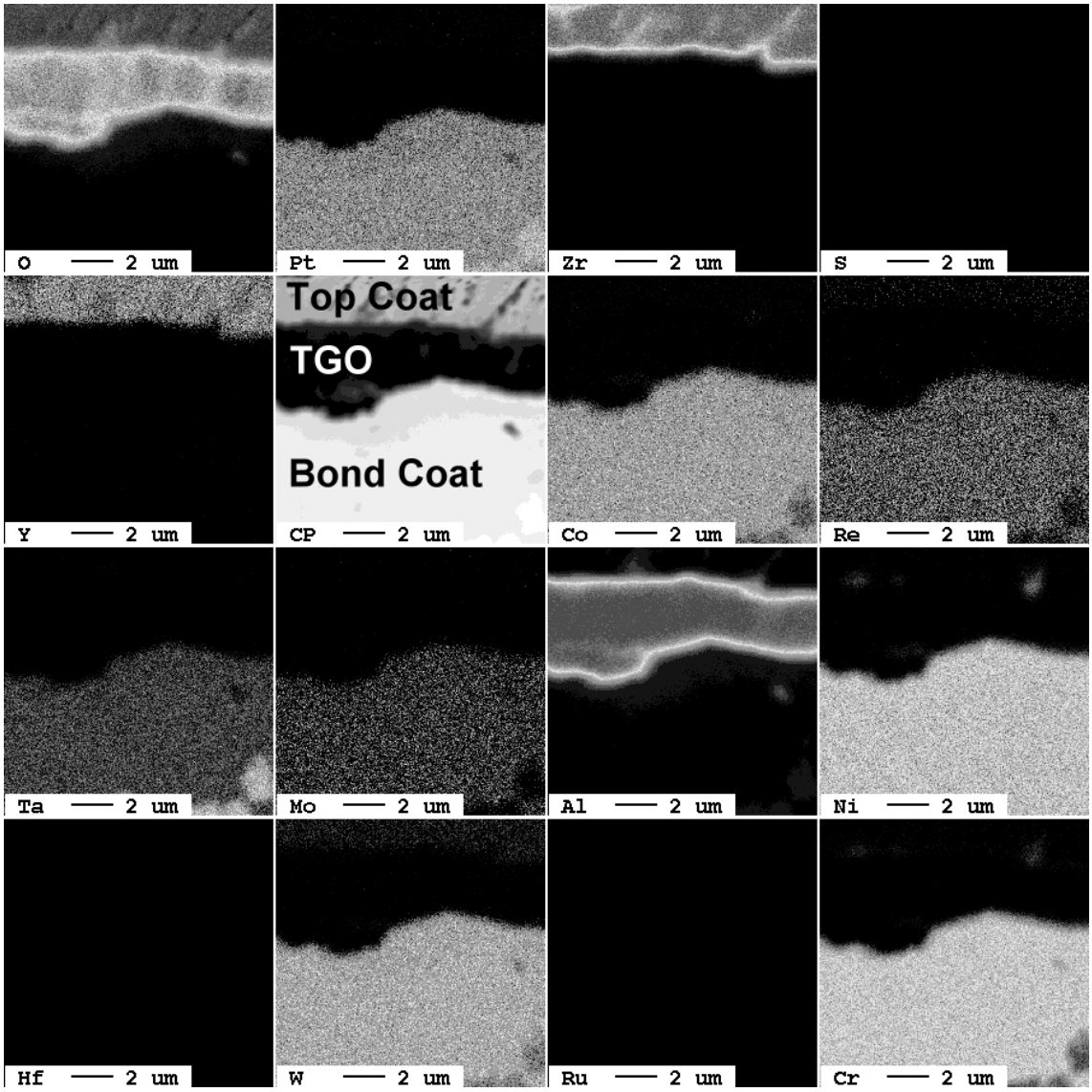

Figure 5.6 Quantitative WDX maps of the TBC coated PWA1484 – Pt-diffusion system following 100 cycle exposure at 1135°C.

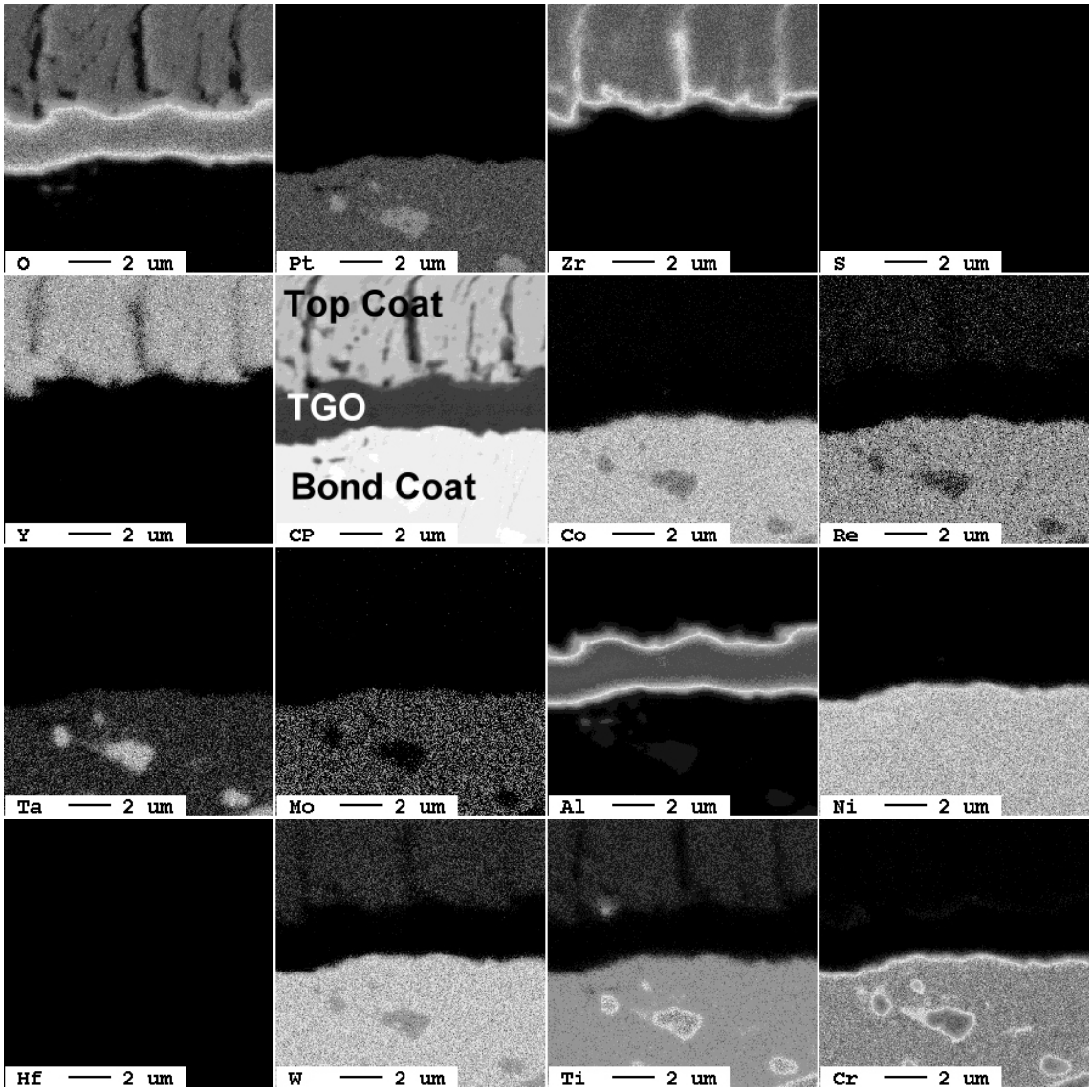

Figure 5.7 Quantitative WDX maps of the TBC coated CMSX-4 – Pt-diffusion system following 100 cycle exposure at 1135°C.

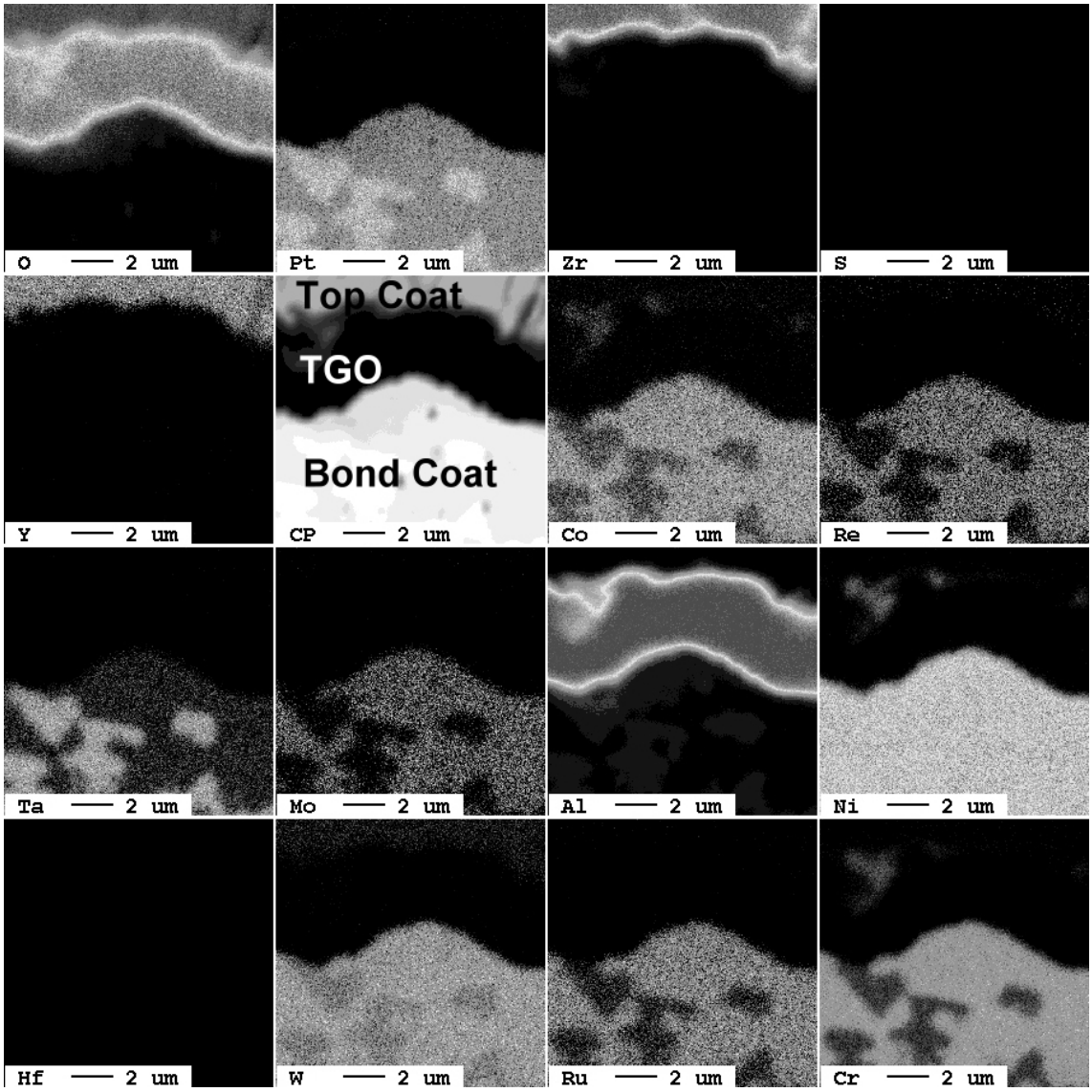

Figure 5.8 Quantitative WDX maps of the TBC coated TMS138A – Pt-diffusion system following 100 cycle exposure at 1135°C.

5.3 Discussion

The results presented here provide new insights into the current understanding of thermal barrier coating systems (TBCs). Traditionally, it is considered that TBC spallation occurs by the accumulation of local damage to form a weakly bonded area that can be susceptible to buckling [14-16]. Choi et al. [14] have studied the competing failure processes of TBCs, such as edge delamination, and small/large –scale buckling.

Their results show that the failure mechanism depends strongly on both the thickness and in-plane modulus of the YSZ top coat. Assuming the in-plane elastic modulus for the EB-PVD top coat is in the range 0.05 to 0.25 times the bulk modulus of dense YSZ [16] and taking the top coat to be approximately 175 μm in thickness as in the case of the current study, substantial suppression of TGO buckling is believed to be present. Therefore, the final failure mode is more likely to be associated with edge delamination or wedging [17] irrespective of the initiation process.

Consider that TBC spallation occurs as the stored elastic energy of the TGO and top coat, which stiffens with time due to sintering, exceeding the interfacial adhesion between the TGO and bond coat. In the case of the steady state energy release rate, a driving force G exists for the delamination of the multilayer TBC as [16]:

$$G = \frac{\left(\sum_i \sigma_o^i h_i\right)^2}{2\sum_i \frac{E_i}{(1-\upsilon_i^2)} h_i}$$

where E_i, h_i and ν_i are the elastic modulus, thickness and Poisson's ratio of each layer i respectively. σ_o is the equi-biaxial residual plane stress. The general argument is that the driving force for spallation (G) increases as the TGO thickens; delamination occurs when G reaches the critical interfacial fracture toughness G_c. In fact, as the EPMA mapping has revealed, the segregation of Ni, Cr and Co –rich oxides above the Al_2O_3 increases the overall TGO thickness and thus, further increased this misfit strain energy.

However, the current findings have conclusively confirmed that the resistance of TBC to spallation during thermal cycling is strongly dependent upon the composition of the superalloy substrate upon which the TBC system is placed. Since there is little correlation between the oxide growth kinetics and the TBC spallation life and the levels of trace elements present (e.g. sulphur) do not vary substantially from alloy to alloy, any differences in TBC lives will be attributable to differences in major elemental additions rather than trace elements.

The presence of Ti as an alloying element in SRR99, TMS-82+, CMSX-4 is suggested to have shortened the TBC life. EPMA mapping of Ti shows a concentration-enriched layer (i.e. a bright layer) near the TGO / bond coat interface in the coated SRR99 system. In fact, previous studies [18, 19] have suggested that fast diffusion of Ti to the surface leads to the formation of titanium rich oxides, potentially weakening the adhesive strength at TGO / bond coat interface. In addition, Ti^{4+} ions, reported [20] to substitute for Al^{3+} ones to create aluminium vacancies within the alumina scale may also degrade the properties of TGO / bond coat interface. Thus, it is not difficult to rationalise the reason why SRR99, among the alloys considered, exhibits the fastest oxidation rate and the shortest TBC life. TMS-138A and PWA1484, in contrast, have no detected enrichment of alloy constituents at the TGO / bond coat interface and represent the two most spallation resistant systems.

Regarding the spallation mechanisms as mentioned previously, it appears that the more spallation-resistant coatings failed at the top coat / TGO interface or tended to fail within the TGO; while specimens with shorter TBC spallation life preferentially failed at the TGO / bond coat interface, which again is the interface most likely to be affected by diffusion of harmful elements from the superalloys.

This leads to a proposed argument that the TGO / bond coat interfacial adhesive strength of TBCs, which controls the TBC lifetime, is a dynamic materials property dependent on and influenced considerably by the composition of the substrate materials (i.e. superalloys). This situation can be qualitatively represented by a schematic drawing (Figure 5.9) which illustrates the possible variation of the driving force G and the interfacial fracture toughness G_c with the time of thermal exposure.

Based upon the steady state energy release rate equation for the delamination of the multilayer TBC, the driving force G increases with TGO thickness, which is assumed to grow parabolically with time t, then thermal cycling at higher temperatures will accelerate the kinetics. The possible variation of G_c is also shown. At the beginning, for any choice of bond coat, G_c is assumed to be roughly the same for all alloy systems

consistent with the identical processing conditions employed. However, upon thermal exposure as the harmful elements, such as Ti, diffuse to the TGO interface, the value of G_c is believed to decrease – rapidly for a substrate system such as the SRR99 and modestly for PWA1484 with other alloys of consideration falling somewhere between the two.

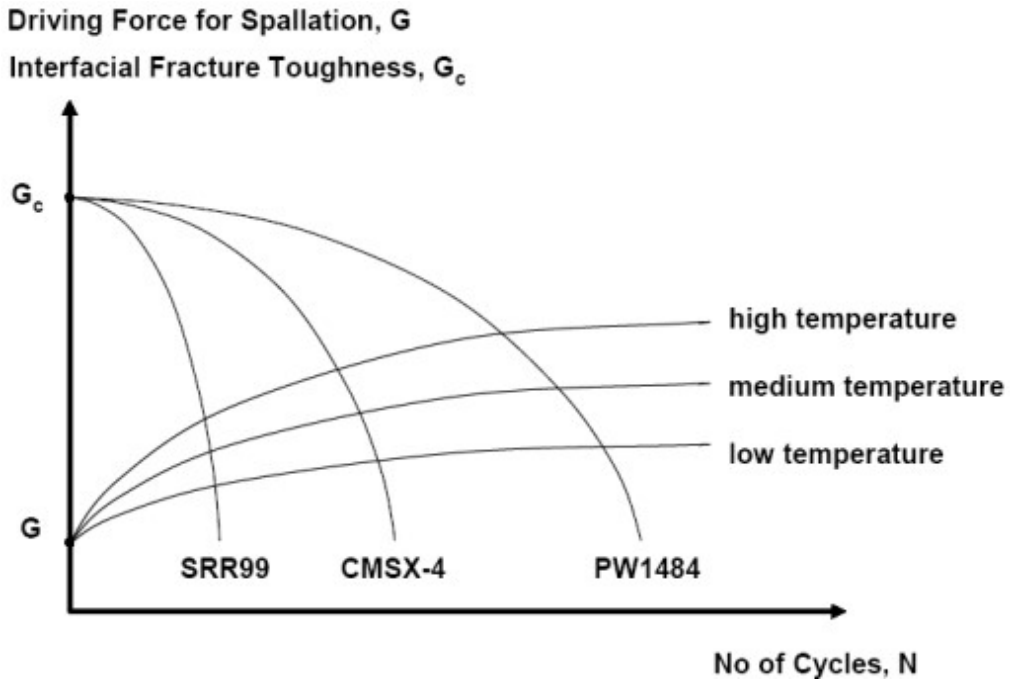

Figure 5.9 Schematic illustration of the proposed variation of driving force G and interfacial fracture toughness G_c during thermal cycling.

It should be recognised that studies published so far have tended to consider just a single substrate composition with a TBC placed upon it; thus, any influence of the substrate chemistry is then factored out from the experiment. It would appear that the superalloy composition has a major influence on the lifetime of the systems, potentially due to the sensitivity of the interfacial fracture toughness to substitutional elements diffusing through the bond coat system from the superalloy substrate beneath it. These findings have implications for the design of TBC systems for the protection of the turbine blade aerofoils used for high temperature applications. Traditionally, nickel-base single crystal superalloys have been designed with their mechanical properties – particularly in creep and fatigue – in mind. However, as the operating conditions of

modern gas turbines continue to become more aggressive and thermal barrier coatings (TBCs) for the provision of thermal insulation are being used increasingly, a further property of the superalloy substrate is then required: that of compatibility with the TBC system which it is required to support. In particular, the influence of different alloying elements present in the superalloy on the TBC's interfacial fracture toughness needs to be better understood.

5.4 Conclusions

The following conclusions can be drawn from this work:

1. It is demonstrated conclusively that the compatibility of modern nickel-based single crystal superalloys with thermal barrier coating (TBC) systems depends acutely upon the superalloy chemical composition.

2. In the experiments reported here, TBC spallation life was found to depend significantly on the chemical composition of the superalloy substrate; this effect implies that considerable chemical effects are at play.

3. An improvement of about 10% in spallation life was nonetheless displayed by the so-called Pt-diffusion bond coat system. This was observed consistently for the different substrate compositions considered.

4. These results can be presumably explained by the fracture toughness parameters controlling decohesion – for example the fracture toughness of the thermally grown oxide (TGO) and the fracture toughnesses of the interfaces bounding it – are influenced strongly by small changes in composition arising from interdiffusion with the bond coat, which itself inherits elemental changes from the substrate.

5. Single crystal superalloys have traditionally been designed primarily with mechanical performance in creep and fatigue in mind. The results reported here show that the

compatibility with the thermal barrier coating systems placed upon them is also an important design parameter.

6. For optimum turbine blade aerofoil characteristics in service, it may now be necessary to balance the mechanical behaviour of the substrate and its compatibility with the TBC systems in order to improve the performance of the system as a whole.

References for Chapter 5

1. R.C. Reed, “Superalloys: Fundamentals and Applications”, Cambridge University Press, (2006).

2. C.G. Levi, “Emerging materials and processes for thermal barrier systems,” Current Opinion in Solid State and Materials Science, Volume 8, 2004, Pages 77-91.

3. N.P. Padture, M. Gell and E.H. Jordan, “Thermal barrier coatings for gas-turbine applications,” Science, Volume 296, 2002, Pages 280-284.

4. V.K. Tolpygo and D.R. Clarke, “On the rumpling mechanism in nickel-aluminide coatings, part I: an experimental assessment,” Acta Materialia, Volume 52, 2004, Pages 5115-5127.

5. B.A. Pint, I.G. Wright, W.Y. Lee, Y. Zhang, K. Prussner and K.B. Alexander, “Substrate and bond coat compositions: factors affeccting alumina scale adhesion,” Materials Science and Engineering A, Volume 245, 1998, Pages 201-211.

6. B.A. Pint, “The role of chemical composition on the oxidation performance of aluminide coatings,” Surface and Coatings Technology, Volume 188-189, 2004, Pages 71-78.

7. B.A. Pint, I.G. Wright, W.Y. Lee, Y. Zhang, K. Prussner and K.B. Alexander, “Substrate and bond coat compositions: factors affecting alumina scale adhesion,” Materials Science and Engineering A, Volume 245, 1998, Pages 201- 211.

8. B.A. Pint, J.A. Haynes, K.L. More and I.G. Wright, “The use of model alloys to understand and improve the performance of Pt-modified aluminide coatings,” Superalloys 2004, edited K.A. Green, T.M. Pollock, H. Harada, T.E. Howson, R.C. Reed, J.J. Schirra and S. Walston, (Warrendale, PA, USA: The Minerals, Metals and Materials Society (TMS), 2004), Pages 597-606.

9. E.P. Busso, J. Lin and S. Sakurai, “A mechanistic study of oxidation-induced degradation in a plasma-sprayed thermal barrier coating system: Part II: Life prediction model,” Acta Materialia, Volume 49, 2001, Pages 1529-1536.

10. F. Traeger, M. Ahrens, R. Vaβen and D. Stover, “A life time model for ceramic thermal barrier coatings,” Materials Science and Engineering A, Volume 358, 2003, Pages 255-265.

11. E.P. Busso, L. Wright, H.E. Evans, L.N. McCartney, S.R.J. Saunders, S. Osgerby and J. Nunn, “A physics-based life prediction methodology for thermal barrier coating systems,” Acta Materialia, Volume 55, 2007, Pages 1491-1503.
12. M. Baker, J. Rosler and G. Heinze, “A parametric study of the stress state of thermal barrier coatings Part II: cooling stresses,” Acta Materialia, Volume 53, 2005, Pages 469-476.
13. M. Jinnestrand and S. Sjostrom, “Investigation by 3D FE simulations of delamination crack initiation in TBC caused by alumina growth,” Surface and Coatings Technology, Volume 135, 2001, Pages 188-195.
14. S.R. Choi, J.W. Hutchinson and A.G. Evans, “Delamination of multilayer thermal barrier coatings,” Mechanics of Materials, Volume 31, 1999, Pages 431-447.
15. M.Y. He, D.R. Mumm and A.G. Evans, “Criteria for the delamination of thermal barrier coatings; with application to thermal gradients,” Surface and Coatings Technology, Volume 185, 2004, Pages 184-193
16. A. Selcuk, A. Atkinson, “The evolution of residual stress in the thermally grown oxide on Pt diffusion bond coats in TBCs,” Acta Materialia, Volume 51, 2003, Pages 535-549
17. A. Strawbridge, H.E. Evans, “Mechanical failure of thin brittle coatings,” Engineering Failure Analysis, Volume 2, 1995, Pages 85-103.
18. B.A. Pint, J.A. Haynes, K.L. More, I.G. Wright, C. Leyens, “Compositional effects on aluminide oxidation performance: objectives for improved bond coats,” Superalloys 2000, edited T.M. Pollock, R.D. Kissinger, R.R. Bowman, K.A. Green, M. McLean, S.L. Olson and J.J. Schirra, (Warrendale, PA, USA: The Minerals, Metals and Materials Society (TMS), 2000), Pages 629–638.
19. A.L. Purvis and B.M. Warnes, “The effects of platinum concentration on the oxidation resistance of superalloys coated with single-phase platinum aluminide,” Surface and Coatings Technology, Volume 146-147, 2001, Pages 1-6.
20. P. Fox, G.J. Tatlock, “Effect of tantalum additions on oxidation of overlay coated superalloys,” Materials Science and Tecchnology, Volume 5, 1989, Pages 816-827

Chapter 6

Comparison of failure mechanisms in TBCs with different Pt-modified bond coats

---

6.1 INTRODUCTION

Traditionally, the study of TBCs has been focused on the investigation of individual bond coat systems [1-4]. However, as the operating temperature of advanced gas turbines increases, new bond coats based on existing ones, are required to meet this demand and suit different applications [5, 6]. Thus, it becomes necessary to not only understand how a coating system performs; but also to know how and why existing coating systems behave differently.

However, little work [7] has been reported in which the modes of degradation responsible for TBC spallation are compared for different bond coats. This is despite much progress that has been made on the micromechanics of the failure of aluminide bond coat systems [2, 3]. In particular, the usual approach in modelling of TBC failure [8-13] concentrates on the treatment of the oxidation-induced stresses that drive TBC spallation despite the fact that it is likely that the modes of failure [5, 14, 15] and evolution of the residual stress are influenced considerably by the bond coat systems.

The work reported here was carried out with these factors in mind. Three different representative bond coat systems were deposited on single crystal CMSX-4 substrates and then subjected to identical (industry standard) EB-PVD YSZ coating processes. It is shown that both the evolution of the residual stress in the TGO and the mode of TBC failure depend on the bond coat composition. Field emission gun scanning electron

microscopy (FEG-SEM) and energy dispersive x-ray (EDX) analysis were used to study the composition and microstructure changes occurring near the TGO/bond coat interface.

6.2 RESULTS

6.2.1 Cyclic Oxidation Testing

The TBC spallation life (defined as detachment of top coat by approximately 20 percent in area) in thermal cycling conditions was found to be slightly dependent on the type of bond coat system used, see Figure 6.1. Pt-diffusion bond coat specimens achieved a mean TBC life of 384 cycles; 15% and 23% longer than for LT and HT Pt-Al bond coats. It should be pointed out that although the three bond coats differed significantly in composition and were prepared by different coating manufacturing processes, all three systems showed remarkably similar spallation life. However, it was found that depending on the type of bond coat, decohesion of the TBC occurred at different interfaces. Since the substrate and the ceramic top coat were prepared to be identical, this can only be explained by the different behaviours of the bond coats, as will be discussed later.

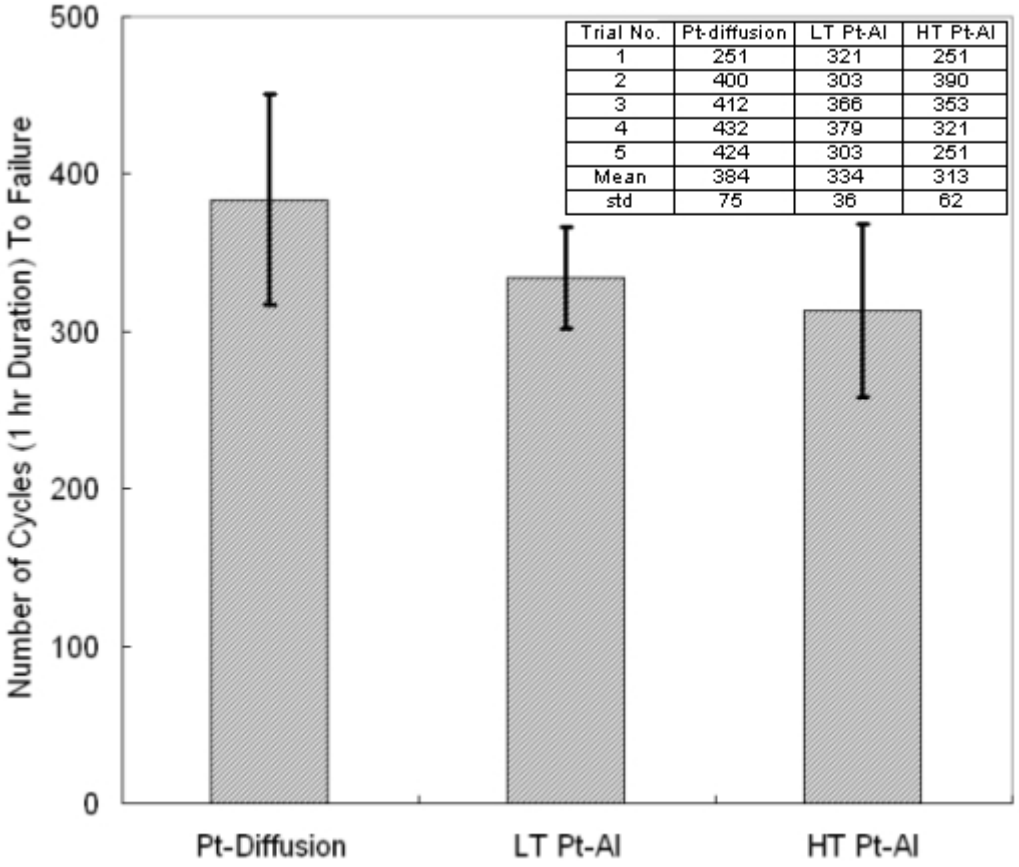

Figure 6.1 TBC spallation life for cyclic oxidation testing (1 hour at 1135°C) of TBC systems. The error bars indicate ± one standard deviation in the lifetimes of each set of five specimens.

6.2.2 Residual Stress Measurement by Luminescence Spectroscopy

Luminescence measurements illustrating the evolution of residual stress in the TGO layer are given in Figure 6.2. It was found that that the evolution of this stress was substantially different between the Pt-diffusion and the Pt-Al bond coat systems, despite the fact that they all had similar initial stress level in the as-coated condition. The Pt-diffusion bond coat systems began with a compressive stress of 2.8 GPa that gradually increased to 3.5 GPa over the coating lifetime, while those of the Pt-Al coatings decreased from an initial compressive stress of about 2.3 GPa to between 1 and 1.5 GPa during the first 75 - 100 thermal cycles, before maintaining at a steady level to the end of life. The error bars in Figure 4 represent ± one standard deviation of the 121

measurements made at each time step. It is therefore notable that the standard deviation increases significantly for the Pt-diffusion bond coats just before failure.

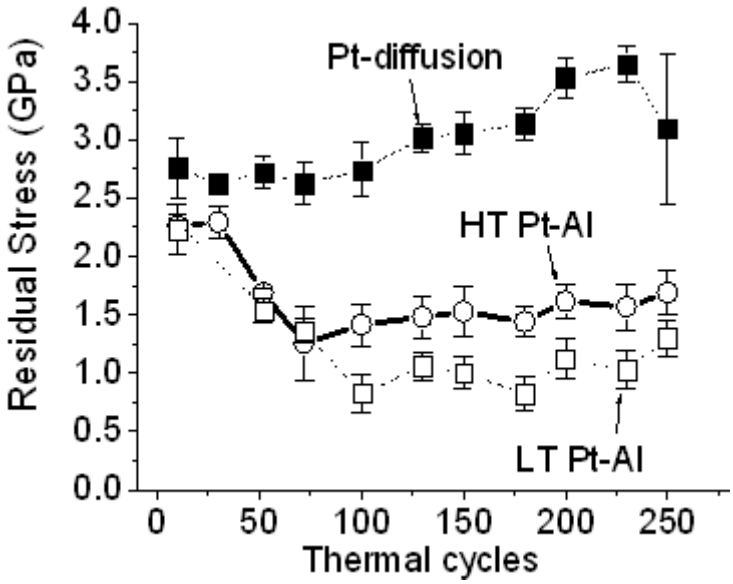

Figure 6.2 Compressive residual stress in the TGO shift vs number of cyclic oxidation testing of the bond coat systems.

6.2.3 Microstructure Imaging of Thermal Cycled Specimens by FE-SEM/EDX

Cross-section scanning electron micrographs illustrating the microstructures of the three coatings after 10, 30, 100, 200, and 280 thermal cycles are shown in Figure 6.3. Based on these SEM images, the oxidation kinetic (TGO thickness vs. time) curve is plotted in Figure 6.4. A few observations can be made with regard to the thermal-cycling induced degradation. First, it can be seen that the TGO morphology evolved quite differently for the three bond coats. For example, the TGO interfaces in the Pt-diffusion system remained intact on thermal cycling for most of its spallation life. In contrast, local interfacial separation of the TGO in the Pt-Al systems occurred at less than 30% of their lifetimes. Furthermore, final spallation occurred at the TGO / YSZ interface for the LT Pt-Al bond coat, but at the TGO / bond coat interface for the Pt-diffusion system. The HT Pt-Al bond coat system showed a mixture of the two failure modes. Finally, the

waviness of the TGO layer in Pt-Al systems appears to amplify significantly upon thermal cycling.

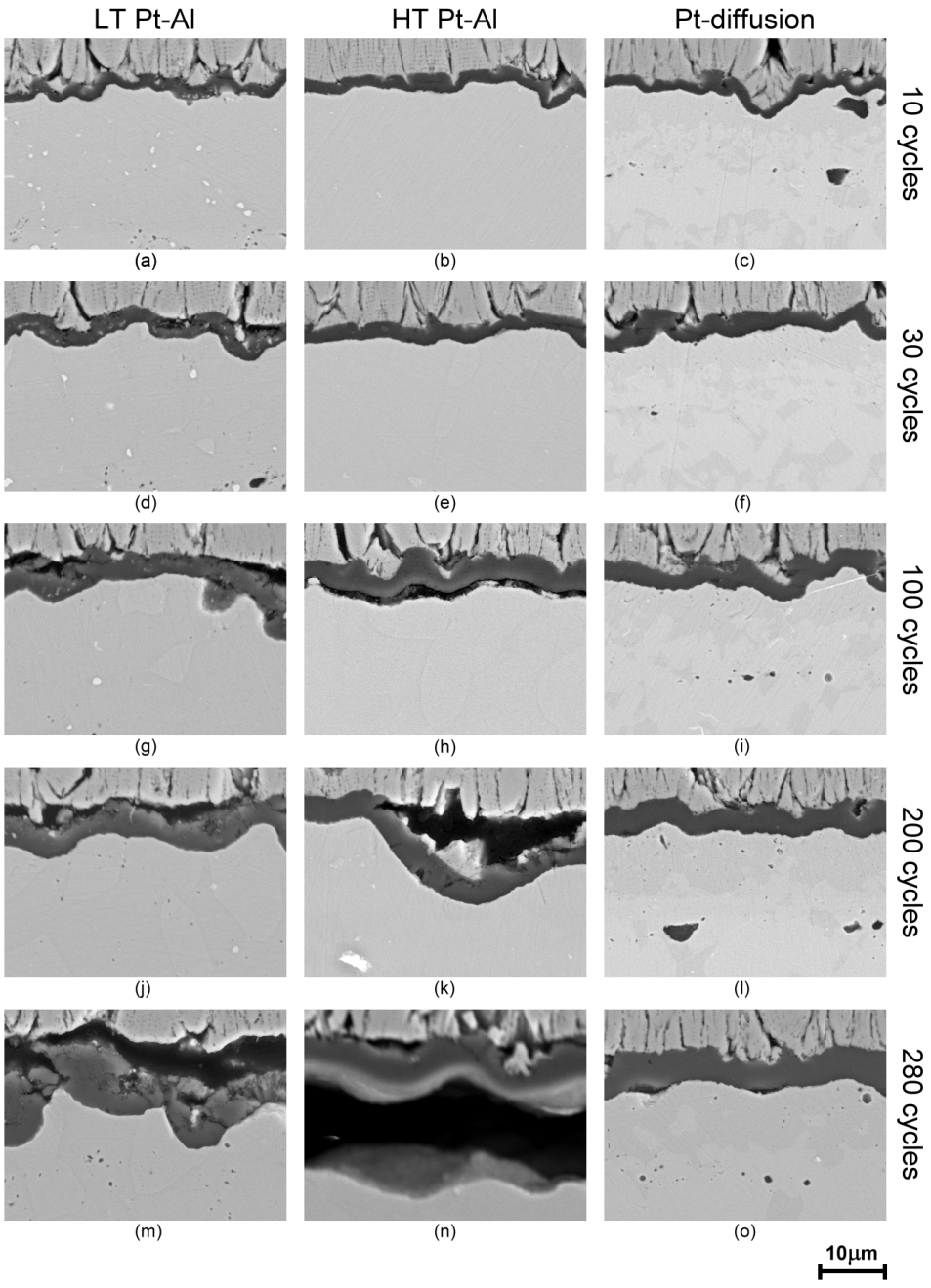

Figure 6.3 A series of SEM micrographs illustrating the near-TGO microstructure of the coatings after 10, 30, 100, 200 and 280 thermal cycles.

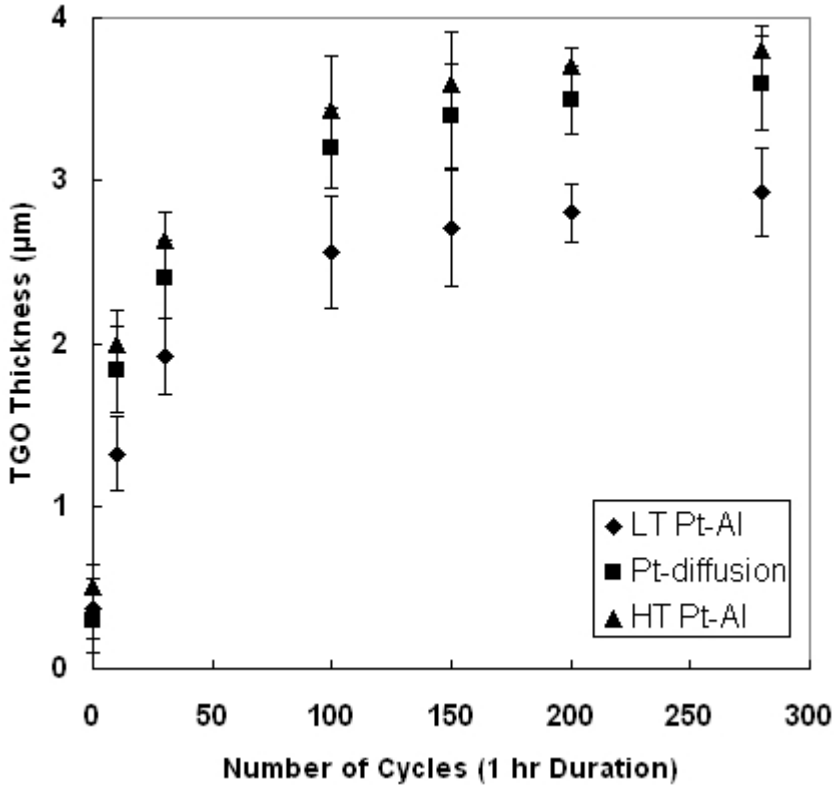

Figure 6.4 TGO thickness vs number of thermal cycles (1hr at 1135°C) for the three bond coat systems.

6.2.4 Quantification of Rumpling at the TGO/Bond Coat Interface.

Measurement of the interfacial waviness was carried out by tracking the normal displacement along the TGO/bond coat interface in a cross-section SEM image over a distance of approximately 640 µm with a step size of 1 µm. Each position on the interface was represented by a pair of X (distance parallel to the specimen surface) and Y (distance normal to the specimen surface) co-ordinates. Figure 6.5 shows the evolution of the TGO/bond coat interface morphology for each of the three bond coat systems. The amplitude of waviness was quantified by determining the standard deviation (STD) of each profile. Figure 6.6 shows the standard deviation from the mean for each profile as a function of the number of thermal cycles. Results of isothermal tests were also plotted for reference. As can be seen in both Figures 6.5 and 6.6, the LT Pt-Al system exhibited a marked increase in TGO/bond coat interfacial waviness with

thermal cycling. The HT Pt-Al bond coat also demonstrated a tendency to roughen with thermal cycling, but at a considerably slower rate. In contrast to the two Pt-Al systems, the Pt-diffusion bond coat showed no detectable roughening.

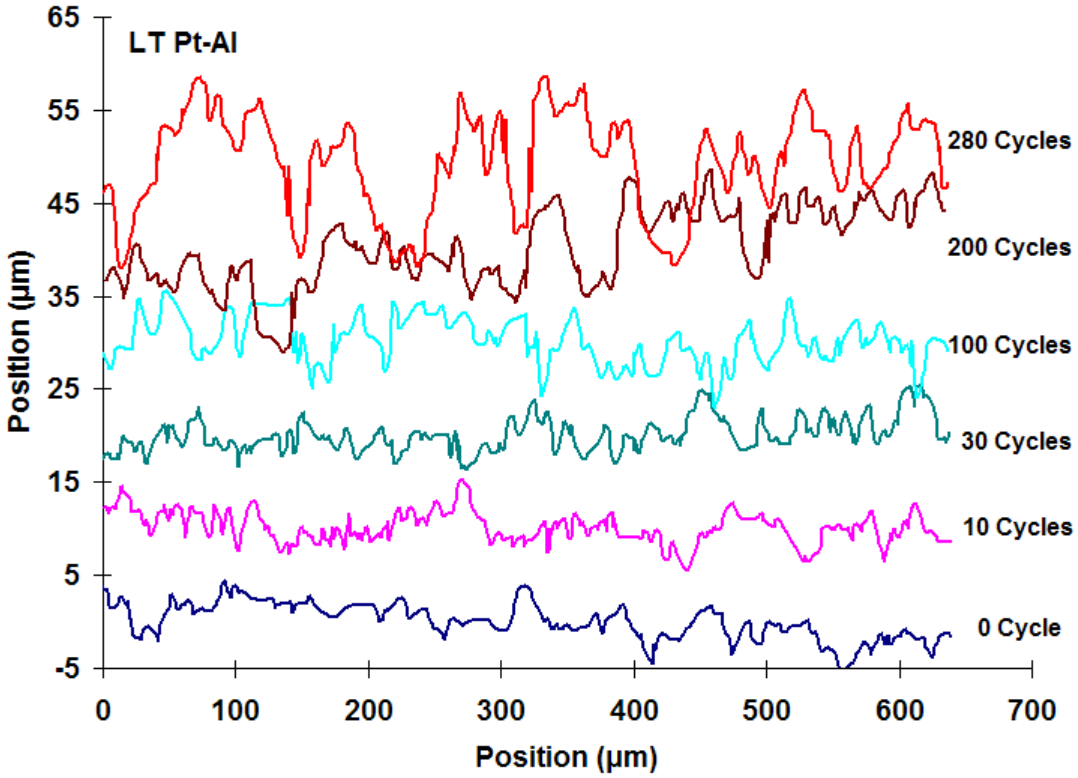

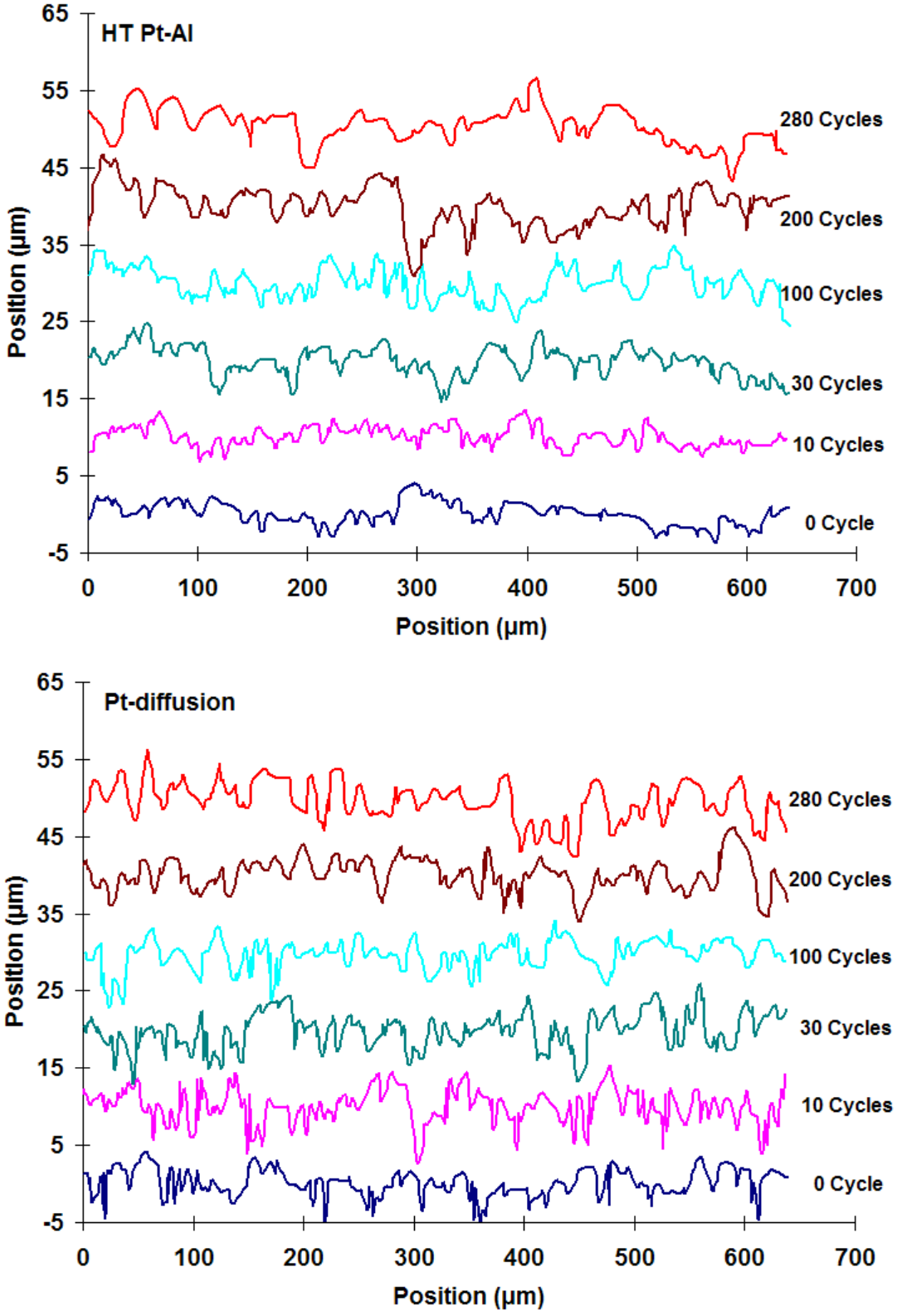

Figure 6.5 TGO/bond coat interface Profiles of top) LT Pt-Al, middle) HT Pt-Al and bottom) Pt-diffusion bond coat at stages of the thermal cycling history.

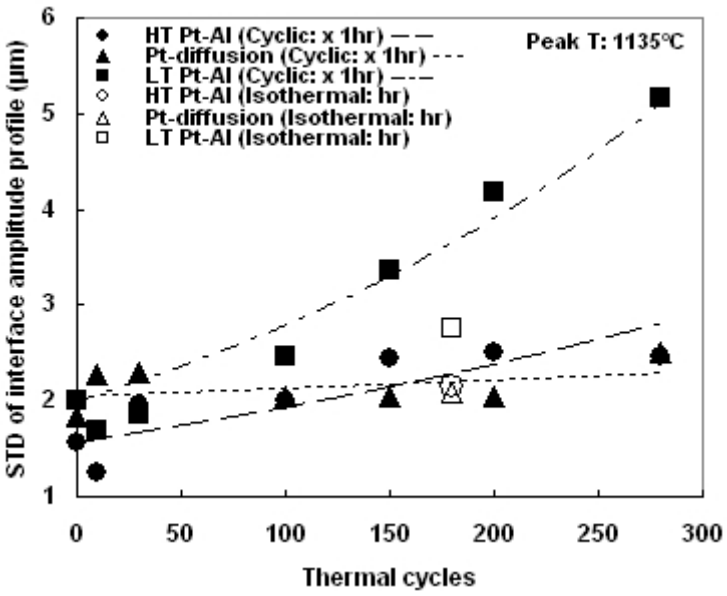

Figure 6.6 Standard deviation of interface amplitude profile (i.e. magnitude of rumpling) as a function of the number of thermal cycles for the 3 different bond coat systems.

6.2.5 Chemical Analyses of TGO layers and Interfaces

Elemental compositions of the TGO layers on the three bond coats were characterised using WDS analysis after 200 thermal cycles, see Table 6.1. The results are quoted only for locations having TGO thickness greater than the spatial resolution of the FE-EPMA/WDS technique. The results show that for all specimens, the oxide layers consisted of more than 99 at% Al_2O_3. Less than a total of 1 at% of other elements originated from the top coat, bond coat and substrate was detected in the oxide layer, possible due to solid solution and particle segregation within the alumina scale. In addition, high resolution Al – mapping (Figure 6.7) of the bond coat near the TGO interfaces using FE-SEM/EDX revealed how the different bond coats respond to the Al loss resulting from TGO growth and interdiffusion with the substrate. Both Pt-Al bond coats showed a progressive phase transformation from the as-deposited single phase β-(Pt,Ni)Al to a two phase β-(Pt,Ni)Al and γ'-$(Pt,Ni)_3Al$ microstructure. These images reveal that the phase transformation in the Pt-Al systems was detectable within the first

30 thermal cycles and the rate of transformation in the HT Pt-Al bond coat appeared to be faster. The Pt-diffusion bond coat, on the other hand, showed a distinct γ' to γ phase transformation near the TGO/bond coat interface. Upon thermal cycling, a continuous γ layer was eventually formed directly below the Al_2O_3 layer and thickened as the Al depletion continued.

Table 6.1 Elemental compositions (at %) taken using WSD FE-EPMA analysis of the TGO layer from specimens at 200 thermal cycles.

Bond Coat	Pt	Zr	Y	Co	Re	Ta	Al	Ni	Ti	Cr	O
LT Pt-Al	0.04	0.21	0.01	0.04	0.01	0.01	37.05	0.23	0.01	0.04	62.35
HT Pt-Al	0.02	0.20	0.02	0.04	0.00	0.02	38.60	0.29	0.02	0.04	60.75
Pt-diffusion	0.04	0.23	0.02	0.02	0.01	0.01	37.75	0.21	0.01	0.02	61.68

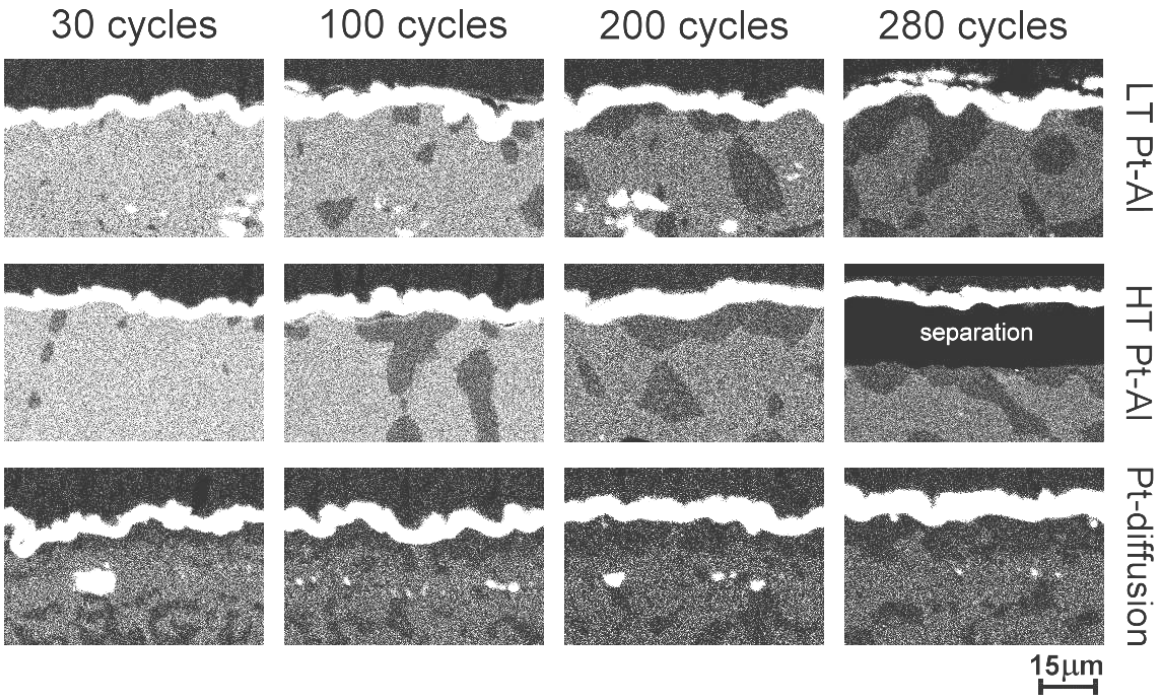

Figure 6.7 A series of Al EDX maps illustrating the microstructural evolution of the bond coat systems after 30, 100, 200 and 280 thermal cycles.

6.3 DISCUSSION

The results presented here provide a detailed comparison of the progressive degradation of TBCs with three different bond coat systems upon thermal exposure. The results show that the three TBC coated bond coat systems failed with quite different characteristics, despite having similar lifetimes. In particular, the location of the TBC spallation interface varied strongly with type of bond coat employed. In addition, both the bond coat rumpling and the TGO residual stress measurements showed significantly different behaviour for the different bond coats. Since the substrate and the ceramic top coat were identical for all three systems, these differences can only be explained by the different processes taking place in the bond coats.

Quantification of the bond coat/TGO interfacial roughness indicated that rumpling was detectable within the first 30 cycles of thermal exposure in the Pt-Al systems. Upon further thermal cycling, the undulation in the TGO amplified in the LT Pt-Al system and resulted in localised vertical separation between the YSZ (which remained at its initial roughness) and the TGO as can be clearly seen in Figures 6.3 g) and k). TGO rumpling is capable of relieving the residual stress in the TGO by increasing its waviness [16], which explains the reduction of the TGO residual stress in the Pt-Al coatings. In contrast, the absence of rumpling in the Pt-diffusion bond coat system helped in ensuring the YSZ/TGO and the TGO/bond coat interfaces remained intact over the majority of the coating lifetime. Consequently, when there was significant rumpling (i.e. the LT Pt-Al system), coating decohesion took place primarily in the YSZ/TGO interface. In the absence of rumpling as in the case of the Pt-diffusion system, spallation eventually occurred at the bond coat/TGO interface. The HT Pt-Al bond coat system showed a mixture of these two failure modes, presumably due to the fact that its rate of rumpling was considerably less than that of the LT Pt-Al system.

In addition to the observed consequences of rumpling, the mechanism by which rumpling occurs is also of importance. In particular, the dependence of rumpling on the

properties of the bond coat materials must be considered. Upon depletion of Al, a phase transformation from the as-deposited single phase β-(Pt,Ni)Al to a two phase β-(Pt,Ni)Al and γ'-$(Pt,Ni)_3Al$ microstructure takes place in Pt-Al bond coats. It has been proposed [17] that this phase transformation induces non-uniform volume changes of the bond coat and thus leads to rumpling [2, 4, 18-21]. However, this mechanism does not appear to play a major role in inducing bond coat rumpling, at least in our current study, for two reasons. First, according to the proposed mechanism, the LT Pt-Al bond coat, which exhibited strongest rumpling behaviour in our study, should correspondingly have the fastest oxidation kinetics (i.e. fastest Al-depletion rate). However, our results showed that it had the slowest oxidation rate among the three systems studied. Second, the lower-Al containing Pt-Al bond coat (HT PtAl), according to the proposed mechanism, should be more sensitive to Al depletion and thus, prone to the phase transformation induced rumpling than its high-Al Pt-Al counterpart (LT PtAl). However, our results showed the opposite, in that the rate of rumpling in the HT PtAl system was considerably lower than that of the LT PtAl system.

Based on these considerations, it is suggested that rumpling is not primarily induced by the phase transformation associated with the Al-depletion, but depends on the high temperature mechanical properties of the bond coats. Thus, it is hypothesised that the rumpling behaviour observed in this study may be controlled by the high temperature resistance to plastic deformation of these bond coat materials. The fact that the magnitude of rumpling was lower in the isothermal conditions suggested that the rumpling mechanism may be mainly due to micro-mechanical interactions of the TBC systems and strongly related to the resistance of the bond coat materials to plastic deformation at elevated temperatures; but not the temperature and time dependent phase transformation process. The Pt-diffusion bond coat, which inherited the two phase γ and γ' microstructure of the superalloy, should be more resistant to plastic deformation at elevated temperatures than the single phase β-(Pt,Ni)Al Pt-Al bond coats. Similarly in the Pt-Al system, a previous study [22] has suggested that a strengthening effect (i.e. high value creep index and activation energy) can be attributed to the precipitation of finely dispersed γ' within the β matrix. The extent of γ' phase precipitation depends not only on the aluminium depletion by interdiffusion or oxidation, but primarily on how

close the composition is to the β/ β+γ' phase boundary (Figure 6.8) [22] at elevated temperatures. The HT PtAl system, leaner in both Pt and Al near its rumpling interface, is situated closer to the β/ β+γ' phase boundary than the LT PtAl system. Thus, one would expect the HT PtAl system to be stronger in creep than that of the LT PtAl system, due to a higher volume fraction of precipitated γ'. This explanation is consistent with the observation that the Al-rich Pt-Al (LT Pt-Al) bond coat exhibited a considerably faster rumpling rate than the low Al-containing one (HT Pt-Al). Clearly, further studies need to be done to clarify the role of high temperature plasticity in the rumpling phenomenon. These are described in the next chapter.

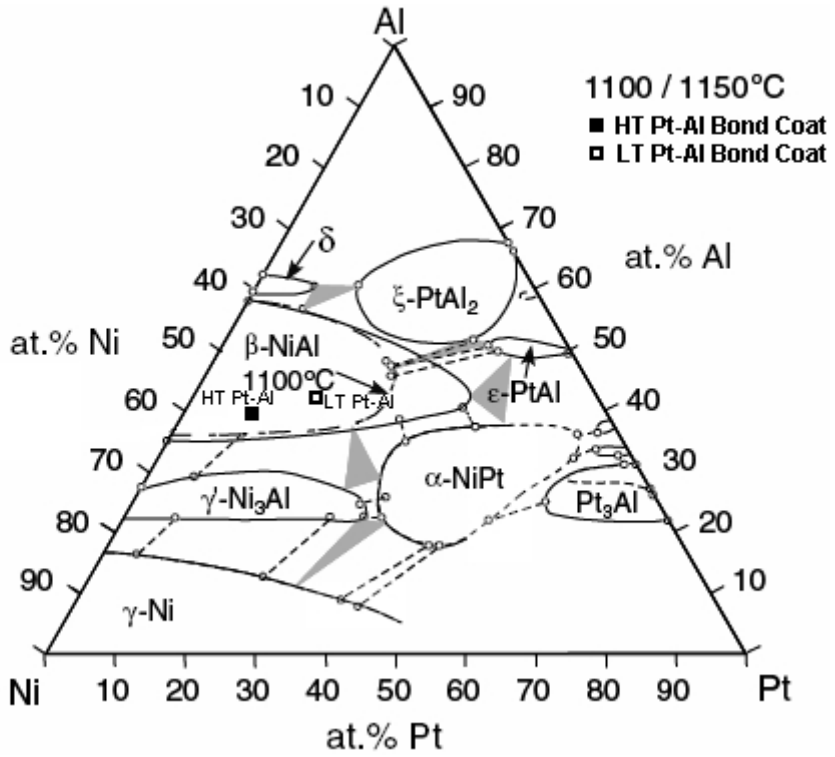

Figure 6.8 Ternary Ni-Al-Pt phase diagram at 1100 and 1150°C [22] showing the two Pt-Al bond coat systems considered in the current study.

6.4 CONCLUSIONS

The following conclusions can be drawn from this work:

1. Spallation occurred at the TGO / YSZ interface for the LT Pt-Al bond coat system, but at the TGO / bond coat interface for the Pt-diffusion system. The HT Pt-Al bond coat system showed a mixed mode failure of the two.

2. The TGO compressive residual stress in the Pt-diffusion bond coat systems began at 2.8 GPa and gradually increased to 3.5 GPa near the end of the coating life. However, for the Pt-Al systems, the stress decreased from 2.3 GPa to between 1 and 1.5 GPa during the first 75 - 100 thermal cycles, before maintaining a steady level to the end of life, with the LT Pt-Al system showing the lower TGO stress.

3. Both Pt-Al systems exhibited rumpling behaviour, but the LT Pt-Al bond coat system showed a significantly faster rumpling rate than the HT Pt-Al bond coat system. The Pt-diffusion system, in contrast, showed no tendency to rumple.

4. The fact that the magnitude of rumpling was lower in the isothermal conditions suggested that the rumpling mechanism is not due to the phase transformation associated with Al-depletion, but related to the high temperature mechanical properties of the bond coat materials.

5. The rumpling results can be explained only if the two phase γ and γ' microstructure of the Pt-diffusion bond coat is more resistant to plastic deformation at elevated temperatures than the single phase β-(Pt,Ni)Al Pt-Al bond coats.

6. The HT PtAl system is considered to be stronger in creep than that of the LT PtAl system, due to a higher volume fraction of precipitated γ' (i.e. the HT PtAl system, leaner in both Pt and Al near its rumpling interface, is situated closer to the β/ β+γ' phase boundary than the LT PtAl system.).

References for Chapter 6

1. A.G. Evans, D.R. Mumm, J.W. Hutchinson, G.H. Meier and F.S. Pettit, “Mechanisms controlling the durability of thermal barrier coatings,” Progress in Materials Science, Volume 46, 2001, Pages 505-553

2. V.K. Tolpygo and D.R. Clarke, “On the rumpling mechanism in nickel-aluminide coatings, part I: and experimental assessment,” Acta Materialia, Volume 52, 2004, Pages 5115-5127.

3. V.K. Tolpygo and D.R. Clarke, “On the rumpling mechanism in nickel-aluminide coatings, part II: characterisation of surface undulations and bond coat swelling,” Acta Materialia, Volume 52, 2004, Pages 5129-5141.

4. M. Gell, K. Vaidyanathan, B. Barber, J. Cheng and E. Jordan, "Mechanism of spallation in platinum aluminide/electron beam physical vapor-deposited thermal barrier coatings,” Metallurgical and Materials Transactions A, Volume 30A, 1999, Pages 427-435

5. C.G. Levi, “Emerging materials and processes for thermal barrier systems,” Current Opinion in Solid State and Materials Science, Volume 8, 2004, Pages 77-91.

6. N.P. Padture, M. Gell and E.H. Jordan, “Thermal barrier coatings for gas-turbine applications,” Science, Volume 296, 2002, Pages 280-284.

7. R.C. Pennefather, and D.H. Boone, “Mechanical degradation of coating systems in high-temperature cyclic oxidation,” Surface and Coatings Technology, Volume 47, 1995, Pages 76-77

8. E.P. Busso, J.Lin and S. Sakurai, “A mechanistic study of oxidation-induced degradation in a plasma-sprayed thermal barrier coating system: Part II: Life prediction model,” Acta Materialia, Volume 49, 2001, Pages 1529-1536.

9. F. Traeger, M. Ahrens, R. Vaβen and D. Stover, “A life time model for ceramic thermal barrier coatings,” Materials Science and Engineering A, Volume 358, 2003, Pages 255-265.

10. E.P. Busso, L. Wright, H.E. Evans, L.N. McCartney, S.R.J. Saunders, S. Osgerby and J. Nunn, “A physics-based life prediction methodology for thermal barrier coating systems,” Acta Materialia, Volume 55, 2007, Pages 1491-1503.

11. M. Baker, J. Rosler and G. Heinze, “A parametric study of the stress state of thermal barrier coatings Part II: cooling stresses,” Acta Materialia, Volume 53, 2005, Pages 469-476.
12. M. Jinnestrand and S. Sjostrom, “Investigation by 3D FE simulations of delamination crack initiation in TBC caused by alumina growth,” Surface and Coatings Technology, Volume 135, 2001, Pages 188-195.
13. A.M. Karlsson and A.G. Evans, “A numerical model for the cyclic instability of thermally grown oxides in thermal barrier systems,” Acta Materialia, Volume 49, 2001, Pages 1793-1804.
14. A.G. Evans, M.Y. He and J.W. Hutchinson, “Mechanics-based scaling laws for the durability of thermal barrier coatings,” Progress in Materials Science, Volume 46, 2001, Pages 249-271
15. J.S. Wang and A.G. Evans, “Measurement and analysis of buckling and buckle propagation in compressed oxide layers on superalloy substrates,” Acta Materialia, Volume 46, 1998, Pages 4993-5005
16. G. Lee, A. Atkinson and A. Selcuk, “Development of residual stress and damage in thermal barrier coatings,” Surface and Coatings Technology, Volume 201, Proceedings of the 33rd International Conference on Metallurgical Coatings and Thin Films - ICMCTF 2006, The 33rd International Conference on Metallurgical Coatings and Thin Films, 2006, Pages 3931-3936.
17. V.K. Tolpygo and D.R. Clarke, “Surface rumpling of a (Ni, Pt)Al bond coat induced by cyclic oxidation,” Acta Materialia, Volume 48, 2000, Pages 3283-3293.
18. D.R. Mumm, A.G. Evans and I.T. Spitsberg, “Characterisation of a cyclic displacement instability for a thermally grown oxide in a thermal barrier coating system,” Acta Materialia, Volume 49, 2001, Pages 2329-2340
19. D.R. Mumm and A.G. Evans, “On the role of imperfections in the failure of a thermal barrier coating made by electron beam deposition,” Acta Materialia, Volume 48, 2000, Pages 1815-1827
20. V.K. Tolpygo and D.R. Clarke, “Morphological evolution of thermal barrier coatings induced by cyclic oxidation,” Surface and Coatings Technology, Volumes 163-164, 2003, Pages 81-86.
21. B. Gleeson, W. Wang, S. Hayashi, D. Sordelet, “Effects of platinum on the

Interdiffusion and Oxidation Behavior," Materials Science Forum, Volume 213, 2004, Pages 461-464

22. M.P. Taylor, H.E. Evans, E.P. Busso, and Z.Q. Qian, "Creep properties of a Pt-aluminide coating," Acta Materialia, Volume 54, 2006, Pages 3241-3252.

Chapter 7

An Investigation of the high temperature plasticity of TBCs with different Pt-modified bond coats

7.1 INTRODUCTION

Thermal barrier coating (TBC) systems based on an electron beam physical vapour deposited (EB-PVD) yttria-stabilised zirconia (YSZ) top coat and a substrate material of CMSX-4 superalloy were identically prepared to systematically study the behaviour of different bond coats (two beta-structured Pt-Al types and a gamma-gamma prime type), as presented in the previous chapter. The reported results showed that the three TBC coated bond coat systems failed with quite different characteristics, despite having similar lifetimes. In addition, both the bond coat rumpling and the TGO residual stress measurements showed significantly different behaviours for the different bond coats. For instance, the LT Pt-Al bond coat system showed a significantly faster rumpling rate than the HT Pt-Al bond coat system; while, the Pt-diffusion system, in contrast, showed no tendency to rumple. The fact that the magnitude of rumpling was lower in the isothermal conditions suggested that the rumpling mechanism is not due to the phase transformation associated with Al-depletion, but related to the high temperature mechanical properties of the bond coat materials. With this in mind, the rumpling results might be explained if the two phase γ and γ' microstructure of the Pt-diffusion bond coat is more resistant to plastic deformation at elevated temperatures than the single phase β-(Pt,Ni)Al Pt-Al bond coats. Thus, the experiment described in this chapter was carried out to investigate whether the differences in high temperature mechanical properties of the bond coats are indeed responsible for the previously mentioned rumpling phenomena.

7.2 EXPERIMENTAL DETAILS

In order to verify if the high temperature plasticity is indeed the mechanism driving the interfacial rumpling observed in the Pt-Al bond coat systems, measurement of plastic deformation of specimens' free edge was carried out for all the bond coat systems.

Coated disc-shape samples, identical to the ones mentioned in the previous chapter were used for this experiment. These samples were further cut into square specimens of 4 mm side. A total of six specimens (i.e. two specimens for each bond coat type) having the same dimensions as previously were used for the investigation. The two free edge surfaces perpendicular to the observation face and the the oxide interface were polished to #400-grit finish for all the specimens. Three of the six polished specimens were then subjected to cyclic thermal exposure in a purpose-built rig. The thermal profile involved 1 hour at a furnace temperature of 1135°C (approximately 10 mins to reach the peak temperature); after which, the specimens were removed automatically from the rig and fan-cooled by laboratory air for 1 hour, identical to the conditions employed in the previous chapter. Specimens were removed from the rig at specific intervals for optical measurements of any mechanical deformation at the free edge and then returned for further thermal cycling. The remaining three specimens were isothermally heated at 1135°C in the same rig for 150 hours (equivalent to approximately 180 cycles in terms of the time at peak temperature).

Measurement of the edge displacement was carried out by using a high magnification optical microscope and its integrated CCD system to take high resolution images. These images were then imported into imaging software, which then quantised the edge displacement by making boundary selections (i.e. defining the original edge position and the displaced position). With reference to the known top coat thickness, the edge displacement can be calculated.

7.3 RESULTS

Optical micrographs illustrating the layered structures of the three coatings after polishing are given in Figure 7.1. The polished surface showed optical contrast between the ceramic top coat and the bright metallic bond coat and substrate for specimens.

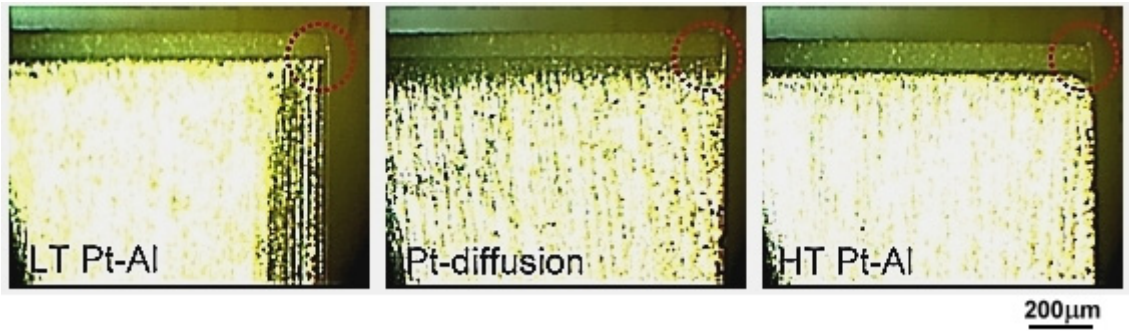

Figure 7.1 Coating cross-sections and polished free edge of as-coated specimens.

Upon thermal cycling, the brightness of the cross-sectional surface was reduced due to surface oxidation. However, the bond coat interfaces became clearly visible, thus, making the measurement of bond coat plastic deformation near the free edge considerably easier, as shown in Figure 7.2. It was found that the elongation of the bond coat was substantially different between the Pt-diffusion and the Pt-Al bond coat systems. Pt-Al bond coats showed significant lateral extension of the bond coat and top coat with reference to the initial edge position. In addition, the extensions of the Pt-Al bond coats were not uniform, meaning that the maximum elongation occurred at the TGO – bond coat interface. This indicates that the driving force for extension comes from the TGO and / or YSZ layers. The Pt-diffusion bond coat systems, in contrast, exhibited much less significant deformation even after 270 cycles.

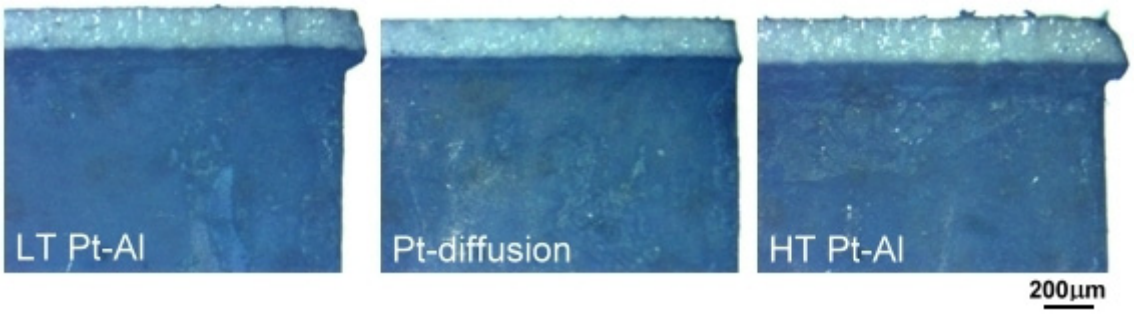

Figure 7.2 Deformation of the coating's free edge after 270 cycles of thermal exposure.

Optical micrographs of the three coatings taken after 10, 30, 50, 70, 100, 130, 160, 200, 240 and 270 thermal cycles were used to construct a plastic deformation curve, showing the percent nominal strain of the bond coat as a function of thermal cycling, as shown in Figure 7.3. The gauge length was taken as half the specimen dimension (i.e. 2 mm). It should be noted that the plotted results were measured for the maximum elongation, i.e. at the TGO – Bond Coat interface. Based on these results, it can be seen that both the Pt-Al bond coats showed very similar deformation behaviours, being the fastest at the beginning and settling to a more steady-state deformation rate after approximately 30 cycles. In contrast to the Pt-Al bond coats, the Pt-diffusion system showed no rapid elongation initially, although the rate of plastic deformation did increase with further thermal cycling, and much lower strains.

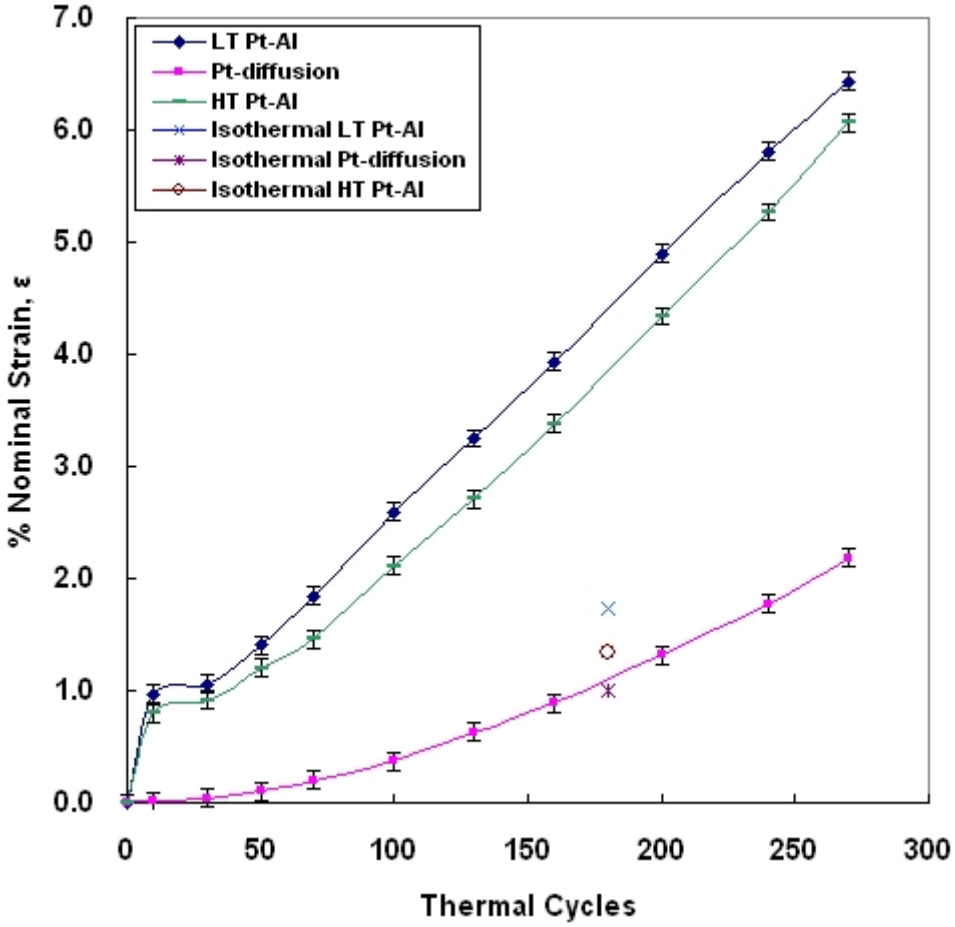

Figure 7.3 Plasticity curve showing the percent strain of the bond coat as a function of thermal cycling.

In order to further investigate whether the observed bond coat plasticity was a thermal cycling induced effect (i.e. thermal mismatch induced stress conditions) or a time at the peak temperature phenomenon (i.e. the time and temperature dependent diffusion processes), an equivalent isothermal version of the experiment was carried out for 150 hours.

Optical micrographs of the three isothermally exposed specimens are shown in Figure 7.4. The results, which are plotted at 180 cycles (i.e. equivalent to 150 hours at peak temperature) in Figure 7.3, show that edge deformation of isothermally exposed Pt-Al bond coats was considerably lower than under thermal cycling conditions; while both isothermally and cyclically exposed Pt-diffusion bond coat specimens had almost identical degrees of edge elongation.

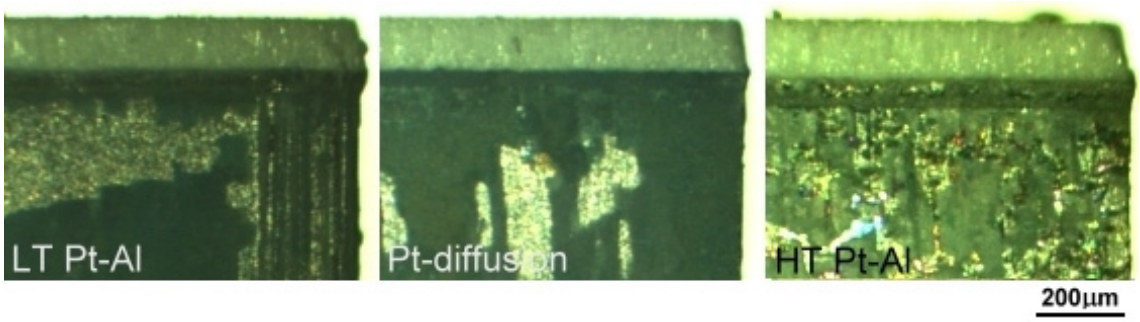

Figure 7.4 Optical micrographs showing the coating's free edge after 150 hours of isothermal exposure.

Observation of the plastically deformed edge showed two geometrically different regions in each of the two Pt-Al bond coats (Figure 7.5). In the case of low temperature Pt-Al bond coat, the transition between the two geometrically different regions of the bond coat took place at about 37 μm away from the TGO/bond coat interface, and at 52 μm in the case of high temperature Pt-Al bond coat. From the aluminium composition profiles (Figure 7.6) of the two as coated Pt-Al bond coats, it is seen that the transition points in the edge deformation lie near locations (LT Pt-Al: 39 μm and HT Pt-Al: 51 μm) where sharp variation in the slope of the as-coated aluminium concentration profile occurred.

It is also evident that a good correlation exists between the local deformation magnitude and the local aluminium concentration for both Pt-Al bond coats. Moreover, LT Pt-Al being the bond coat system with the highest aluminium concentration exhibited the most severe rumpling behaviour and edge plasticity while, the lowest aluminium containing Pt-diffusion bond coat showed very little tendency to rumpling and edge deformation.

It should be noted here that although the as-coated aluminium composition profile no longer represents the profile after 270 cycles, Figure 7.6 is considered appropriate for the purpose of comparing with Figure 7.5 since the edge deformation process did occur from the start of thermal cycling.

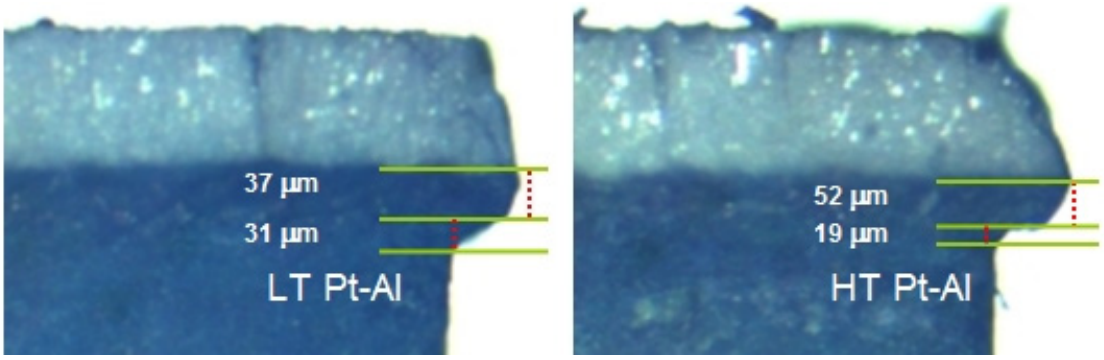

Figure 7.5 Two geometrically different regions in the plastically deformed edge in coated CMSX-4 with LT and HT Pt-Al bond coats.

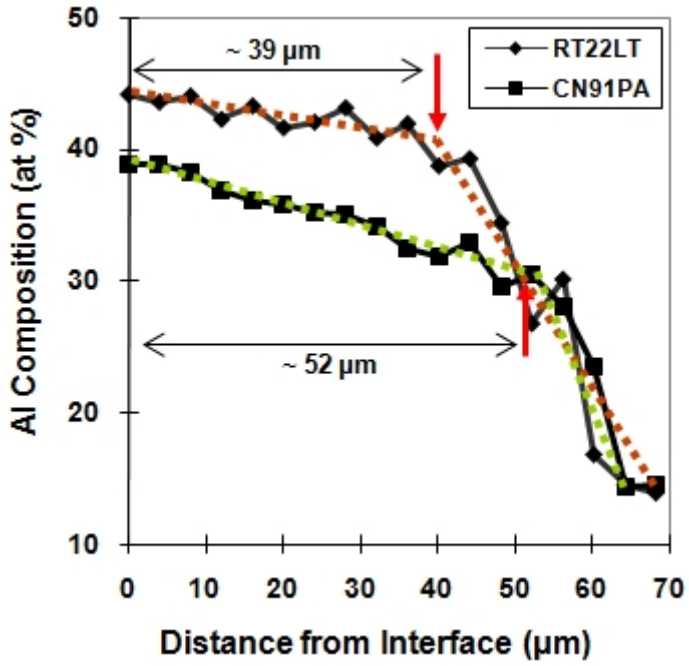

Figure 7.6 Aluminium concentration profiles in as-coated CMSX-4 with LT and HT Pt-Al bond coats.

7.4 DISCUSSION

As discussed in the previous chapter, in addition to the observed consequences of rumpling, the mechanism by which rumpling occurs is also of importance. In particular, the dependence of rumpling on the properties of the bond coat materials must be considered.

The results presented here provide a detailed comparison of the progressive deformation of three different bond coat systems upon thermal exposure. The results show that the Pt-Al bond coats suffered significant plastic deformation of the bond coat on thermal cycling. Pt-diffusion bond coats, on the other hand, deformed plastically by a considerably lower degree under both isothermal and cyclic conditions. In addition, all three bond coats exhibited a quite similar magnitude of bond coat deformation under isothermal conditions.

The fact that the magnitude of bond coat deformation was less in the isothermal conditions for the Pt-Al bond coats suggests that the rumpling mechanism may be mainly due to micro-mechanical interactions of the TBC systems and strongly related to the resistance of the bond coat materials to plastic deformation at elevated temperatures. A temperature and time dependent phase transformation process cannot account for the observation. The lower CTEs of the TGO and YSZ in comparison with CMSX-4 will generate a tensile in plane stress in the bond coat on cooling. This can be relaxed by in-plane plastic deformation in the bond coat until at some lower temperatures the bond coat becomes elastic. The elastic deformation is reversible upon heating, while plastic deformation is non-reversible (rachetting [1]). This leads to an incremental plastic elongation per cycle.

As mentioned in the previous chapter, the Pt-diffusion bond coat, which inherited the two phase γ and γ' microstructure of the superalloy, should be more resistant to such plastic deformation at elevated temperatures than the single phase β-(Pt,Ni)Al Pt-Al bond coats. In addition, it was discussed at that time that in the case of Pt-Al system, a

gradual strengthening effect can be attributed to the precipitation of finely dispersed γ' within the β matrix. Since the extent of phase precipitation depends not only on the aluminium depletion by interdiffusion or oxidation, but primarily on how close the composition is to the β/ β+ γ' phase boundary at elevated temperatures, one would expect the different composition profiles (i.e. composition gradient of Ni, Al, Pt, etc) of the Pt-Al diffusion bond coat results in different extents of local strengthening effects.

In particular, based on the consideration of the β/ β+ γ' phase boundary, it is known that the composition dependent phase transformation is mostly sensitive to the aluminium concentration gradient. This is, in fact, confirmed by Figures 7.5 and 7.6, which shows that the transition points in the edge deformation lie near locations where sharp variation in the slope of the as-coated aluminium concentration profile occurred. In Pt-Al coating systems, it appears that the magnitude of the local edge-deformation is related to the local aluminium concentration; while, the slope of the geometrically different regions of the deformed edge is related to the gradients of the aluminium concentration profiles.

7.5 CONCLUSIONS

Based on the comparative study presented in chapters 5 and 6, it is concluded that the high temperature mechanical properties of the bond coat play a critical role in controlling the degradation mechanism of the TBC system. The differences in the TGO residual stress evolution, magnitudes of bond coat rumpling and the degree of plastic deformation of the bond coat at free edges are very much inter-dependent and will eventually determine the failure mechanisms of the TBC system.

In particular, the following specific conclusions can be drawn from this work:

1. Pt-Al bond coats were extremely sensitive to thermal cycling, which resulted in significant plastic deformation of the bond coat. In contrast, Pt-diffusion bond coat showed much smaller plastic deformation.

2. All three bond coats (LT Pt-Al, HT Pt-Al, Pt-diffusion) exhibited quite similar magnitudes of bond coat deformation under isothermal conditions.

3. It is proposed that the plastic elongation of the Pt-Al bond coats at free edges was due to micro-mechanical interactions within the TBC systems and is strongly related to the high temperature strength of the bond coat.

4. Since all three bond coats showed much less bond coat deformation under isothermal conditions, it is argued that the large plastic deformation in the Pt-Al bond coats was not induced by the volume change associated with the temperature and time dependent phase transformation process. Rather, it is consistent with a ratcheting process in these bond coats during thermal cycling. This is absent in the Pt-diffusion bond coats.

5. In Pt-Al coating systems, it appears that the magnitude of the local edge-deformation is related to the local aluminium concentration; while, the slope of the geometrically different regions of the deformed edge is related to the gradients of the aluminium concentration profiles.

References for Chapter 7

1. A.G. Evans, J.W. Hutchinson, “The thermomechanical integrity of thin films and multilayers,” Acta Metallurgica et Materialia, Volume 43, 1995, Pages 2507-2530.

Chapter 8

Conclusions and suggestions for future work

8.1 Summary of Conclusions

The research reported here presents an investigation into the effects of high temperature oxidation and exposure on nickel-base alloys and TBC coated nickel-base superalloys.

In Chapter 3 of this thesis, a one-dimensional coupled thermodynamic-kinetic oxidation and diffusion model capable of predicting the concentration profiles of alloying elements and oxide composition during the transient stage of oxidation of a single-phase ternary alloy has been developed using the finite difference method. Application of the model to the oxidation of a Ni-27Cr-9Al (at%) ternary alloy predicted a rapid depletion in the aluminium concentration at the oxide-metal interface during the early-stage of oxidation. This is because in the early stages of oxidation, Al consumption by oxide scale growth is faster than Al replenishment by diffusion towards the scale. Preferential oxidation of chromium then occurs as the aluminium concentration at the oxide-metal interface drops to near zero. Once a continuous oxide scale has formed, oxidation of nickel to form nickel oxide and spinels with the result that local depletion of nickel at the metal-oxide interface leads eventually to an increase of both aluminium and chromium concentrations as a pseudo steady state is approached. These predictions of the model are in agreement with experiments reported in the literature. It is emphasised that the ability of the alloy to maintain a non-zero concentration of aluminium at the oxide-metal interface during transient oxidation is a key requirement in the design of oxidation-resistant alumina-forming alloys.

The importance of superalloy substrate composition in determining the oxidation kinetics and the cycling life of thermal barrier coating systems was demonstrated in

Chapter 5. The TBC spallation life was found to vary by a factor of up to three, depending upon the chemical composition of the superalloy substrate even though the bond coat and top coat were nominally the same. This effect implies that considerable chemical effects are at play. By comparison, the choice of bond coat among common types has a smaller effect in determining TBC spallation life. The experimental results can be explained only if the fracture toughness parameters controlling decohesion (i.e. the fracture toughness of the TGO and the fracture toughness of the interfaces bounding it) are influenced strongly by small changes in composition arising from interdiffusion with the bond coat, such that they are degraded during thermal cycling. Chemical analysis indicates that trace elements such as sulphur (on the basis of bulk chemical analysis) in the superalloy substrate are not responsible for the effects reported, indicating that major elemental additions are the cause, such as Ti in particular.

In Chapter 6, a detailed study was described of TBC systems, based on an EB-PVD YSZ top coat and a substrate material of CMSX-4 superalloy, with different bond coats. The three bond coat materials investigated include two beta-structured Pt-Al types (differing in their aluminising temperature, LT and HT) and a gamma-gamma prime structure produced by Pt diffusion without aluminising. It was found that the TGO compressive residual stress in the Pt-diffusion bond coat system began at 2.8 GPa and gradually increased to 3.5 GPa near the end of the coating life. In comparison, the stress in the Pt-Al systems decreased from 2.3 GPa to between 1 and 1.5 GPa during the first 75 - 100 thermal cycles, before maintaining a steady level to the end of life, with the LT Pt-Al system showing the lower TGO stress. It was also found that the TBCs with the LT Pt-Al bond coat fail by a rumpling mechanism that generates isolated cracks at the interface between the TGO and the YSZ. In fact, both Pt-Al systems exhibited rumpling behaviour, but the LT Pt-Al bond coat system showed a significantly faster rumpling rate than the HT Pt-Al bond coat system. By contrast, the TBCs with Pt diffusion bond coats do not rumple, and the adhesion at the TGO/YSZ interface does not obviously degrade. In addition, the fact that for the Pt-Al bond coats, the magnitude of rumpling was lower in isothermal conditions suggested that the rumpling mechanism is not due to the phase transformation associated with Al-depletion, but related to the high temperature mechanical properties of the bond coat materials. Thus, it was proposed

that the two phase γ and γ' microstructure of the Pt-diffusion bond coat is more resistant to plastic deformation at elevated temperatures than the single phase β-(Pt,Ni)Al Pt-Al bond coats. Moreover, the HT PtAl system is considered to be stronger in creep than that of the LT PtAl system, due to a higher volume fraction of precipitated γ' (i.e. the HT PtAl system, leaner in both Pt and Al near its rumpling interface, is situated closer to the β/ β+ γ' phase boundary than the LT PtAl system.).

In order to verify if the high temperature bond coat plasticity is indeed responsible for the interfacial rumpling observed in the Pt-Al bond coat systems, measurement of plastic deformation of specimens' free edges was carried out for all the bond coat systems, as presented in Chapter 7. It was found that Pt-Al bond coats were extremely susceptible to bond coat elongation during thermal cycling. In contrast, Pt-diffusion bond coat showed much lower plastic edge deformation. Since all three bond coats (LT-PtAl, HT-PtAl, Pt-diffusion) were found to exhibit quite similar magnitude of bond coat deformation under isothermal conditions, it is proposed that the plastic elongation of the Pt-Al bond coats was due to micro-mechanical interactions of the TBC systems and strongly related to the high temperature strength of the bond coat, rather than the volume change associated with the temperature and time dependent phase transformation processes.

8.2 Suggestions for Future Work

Although results obtained here provide some insight to assist the design of advanced superalloys or oxidation resistant coatings, further work needs to be carried out to elucidate more detailed mechanisms associated with the degradation of thermal barrier coatings.

The coupled thermodynamic-kinetic oxidation and diffusion numerical model developed in the current PhD study presents an initial step in predicting surface oxidation induced composition depth profile changes in a single-phase ternary alloy. However, the presented oxidation treatment does not consider the detailed initial

oxidation morphology (i.e. internal precipitation) and the transition mechanism from the initial internal precipitation of oxides to continuous oxide layers. Moreover, in order to further develop the model to accurately predict the effects of alloying elements on the oxidation of complex alloys without engaging in extensive experimental testing, a more complex multi phase 2-D numerical model needs to be developed to account for the microstructural degradation mechanisms occurring during service exposure, specifically (i) the formation of thermal grown oxides (alumina and spinel phases) by oxidation on the bond coat and (ii) interdiffusion of the bond coat with the superalloy substrate (iii) phase transformation and possible formation of detrimental phases induced by oxidation and inter-diffusion processes. These phase transformations have the common features of reactions occurring in high temperature systems, in that they occur at rates which are diffusion-controlled. The solutions of the underlying coupled diffusion equations (one for each element) are easily arrived at either by analytical or numerical means.

The importance of substrate composition on the lifetime of thermal barrier coatings was highlighted in Chapter 5. The relationship between substrate composition and the composition of the platinum-diffused layer is central to the beneficial effect of platinum-modification in the context of diffusion coating technology. The Pt-diffusion bond coat is resistant to rumpling and results in an enhanced TBC life, but this effect is diminished in alloys containing elements that have an adverse effect on adhesion at the BC/YSZ interface. In view of this, future use of the Pt-diffusion bond coat requires a more considered approach towards the chemistry of the underlying superalloy and the composition of the platinum-diffused substrate prior to top coat application. For optimum turbine blade aerofoil characteristics in service, it may now be necessary to balance the mechanical behaviour of the substrate and its compatibility with the TBC systems in order to improve the performance of the system as a whole.

It is believed that with the development of more sophisticated models, the important phase transformations and oxidation behaviour which govern the degradation of coated superalloys will be modeled, with the goal of developing a predictive capability which is presently lacking; this activity will require the identification of the physical factors which dictate substrate/coating interactions – it will also provide the basis for a chemistry-based approach to coating life prediction.

In terms of the work on the study of bond coat rumpling, the current PhD study showed the different rumpling behaviours between the Pt-diffusion and Pt-Al bond coats. Both Pt-Al systems exhibited rumpling behaviour, but the LT Pt-Al bond coat system showed a significantly faster rumpling rate than the HT Pt-Al bond coat system. The Pt-diffusion system, in contrast, showed no tendency to rumple. It would be of interest as a continuation of the current work, to study the effect of the substrate composition on bond coat rumpling. If such an effect is apparent, it would be interesting to correlate the TBC spallation life with the magnitude of rumpling.

Additionally, the high temperature plasticity of the bond coat should be further investigated. More specifically, the entire experiment demonstrated in Chapter 7 can be repeated on identical specimens without the top coat and in an inert atmosphere to minimise the formation TGO. This will provide additional clarifications of any possible role of the CTE difference between the bond coat and the substrates.